Escola Politècnica Superior
de Castelldefels
UNIVERSITAT POLITÈCNICA DE CATALUNYA

MASTER THESIS

TITLE : UHF RFID tag implementation on cork substrate for wine bottle monitoring

MASTER DEGREE: Master of Science in Telecommunication and Management

AUTHOR: Sergi Rima Martí

DIRECTOR: Apostolos Georgiadis

SUPERVISOR: Jordi Mateu

DATE: November 17, 2013

Títol : UHF RFID tag implementation on cork substrate for wine bottle monitoring

Autor: Sergi Rima Martí

Director: Apostolos Georgiadis

Supervisor: Jordi Mateu

Data: 17 de novembre de 2013

Resum

Un camp de recerca obert és el de les etiquetes d'identificació per ràdio-freqüència (RFID) que utilitzen com a substrat el suro, el qual està relacionat amb l'exploració de l'ús de diferents substrats i tècniques de fabricació adequats per a múltiples i diversos escenaris d'aplicació de la tecnologia RFID. Especialment per a la necessitat creixent d'etiquetes RFID amb capacitats de sensatge afegides.

El suro és un material particularment atractiu ja que es caracteritza per la seva lleugeresa i les seves propietats aïllants, les quals permeten trobar multitud d'aplicacions en la indústria militar, el sector aeronàutic o la indústria del vi. Entre d'altres, la indústria vinícola és susceptible a l'aplicació de la tecnologia RFID ja que pot ser desplegada per al control de la producció, la logística o per a oferir productes amb un valor afegit ja que els consumidors són susceptibles a pagar més diners per un producte millor. No obstant, la identificació d'ampolles de vi és difícil a causa que el material contingut és desfavorable per a l'operació de les antenes.

Aquesta tesi consisteix en la implementació d'una etiqueta UHF RFID col·locada sobre substrat de suro per tal de proporcionar una manera factible de ser insertada dintre un tap de suro. En el treball es presenten els dissenys d'etiquetes RFID i antenes UHF de baix cost que utilitzen suro com a substrat. D'altra banda, també s'investiga l'extensió de l'ús de l'etiqueta RFID per a aplicacions de detecció remota que requereixin d'un baix cost i en aquest sentit es mostra el principi de funcionament d'un sensor de temperatura basat en l'etiqueta RFID.

Per començar, les propietats elèctriques del substrat de suro són caracteritzades en la finalitat d'obtenir valors fiables per ser utilitzats després en el procés de disseny de l'antena. Seguidament, una antena dipol en 3D es fabricada perforant el patró dissenyat sobre cinta adhesiva de coure de baix cost que es col·loca posteriorment sobre el substrat de suro adequadament dimensionat. Aquesta antena s'utilitza a continuació per obtenir una etiqueta RFID que té la forma d'un cub amb dimensions de 21.5x20.75x16.25 mm. El rendiment de l'etiqueta s'avalua a través de mesures en el rang de lectura, assolint una mesura de 100 cm als 920 MHz. Finalment, s'investiga una tècnica que utilitza un canvi en la resposta de l'antena de l'etiqueta RFID com a mecanisme de detecció mitjançant la correlació d'un canvi en la temperatura a un canvi en el rendiment del rang de lectura de l'etiqueta per obtenir un sensor de temperatura basat en l'esmentada etiqueta RFID.

Title : UHF RFID tag implementation on cork substrate for wine bottle monitoring

Author: Sergi Rima Martí

Director: Apostolos Georgiadis

Supervisor: Jordi Mateu

Date: November 17, 2013

Overview

Radio frequency identification (RFID) tags using cork as their substrate is an open research field related to exploring the use of different substrate materials and fabrication techniques suitable for diverse application scenarios, especially for the increasingly need of RFID tags with added sensing capabilities.
Cork is particularly attractive due to its lightweight and insulating properties, finding a multitude of applications from military industry, aeronautics or wine industry. Among the others, the wine sector is susceptible of applying RFID technology as it can be deployed for production control, logistics or to offer added value products as the consumers are sensible to pay more money for a better product. However, identifying wine bottles is difficult due to the unfavorable material content for the operation of the antennas.
This thesis consists on the implementation of a UHF RFID tag placed on cork substrate in order to provide a feasible way to be embedded into a cork stopper. The design of low cost, conformal UHF antennas and an RFID tags on cork substrate is presented. Moreover, the extend of use of an RFID tag for applications that have a need for low-cost, ubiquitous wireless sensing is investigated and the principle of operation of a tag-antenna-based temperature sensor is shown.
The electrical properties of cork substrate are first characterized in order to obtain reliable values to be used after in antenna design process. Following, a 3D meander line dipole antenna is fabricated by milling the designed pattern on low cost adhesive copper tape which is then placed on a properly dimensioned cork substrate. Such antenna is then used to obtain an RFID tag which is shaped as a cube with dimensions of 21.5x20.75x16.25 mm. Tag performance is evaluated through read range measurements achieving a measured range of 100 cm at 920 MHz. Finally, a technique that uses a change in the response of the RFID tag antenna as a sensing mechanism by correlating a change in temperature to a change in RFID tag read range performance is investigated to obtain a tag-antenna-based temperature sensor.

I would like to thank Ph.D. Apostolos Georgiadis for the assistance received during the realization of this thesis and the support given.

I would like to thank also Ph.D. Ana Collado for her suggestions and help received, specially with the cork characterization and the antennas measurements.

I am also thankful to Ph.D. Francesco Giuppi for the help received during the fabrication of the antennas.

Also thanks to Ph.D. Student Kyriaki Niotaki for her support and help with the fabrication of the tags.

Last but not least, thanks to those that directly or indirectly helped me fulfilling this project.

CONTENTS

LIST OF FIGURES

LIST OF TABLES

INTRODUCTION

RFID technology is applied in an increasing number of applications from identification and localization to various types of monitoring and sensing [1]. The large and diverse number of application scenarios result in various challenges for the tag design, which include a diverse range of substrate materials as well as the use of different fabrication techniques targeting large volume production such as inkjet printing [2].

A characteristic example of the requirement for low profile, conformal RFID tags is related to liquid bottle tagging, including water, wine and as well as a variety of other liquids. The challenge for conformal and low profile antennas, has led to different antenna designs, such as a meander monopole placed inside a hollow plastic bottle closure [3], and several designs consisting of dipole antennas placed around the bottle plastic or glass neck [4] [5] or body [6].

This thesis is aimed to provide a low profile, conformal RFID tag related to wine bottle tagging. The work is focused on the design of a passive UHF RFID tag placed on cork substrate and shapped to be embedded inside a cork stopper. Moreover, it is considered a fast and cost effective tag fabrication process involving standard milling fabrication on addhesive copper tape which is then attached to the cork substrate. Additionally, RFID-tag-antenna-based sensing principle is applied on the tag aiming to propose a low-cost, long-lifetime temperature wireless RFID-sensor.

0.1. RFID

Radio Frequency IDentification (RFID) is a technology that uses electronic tags placed on objects, people or animals to relay identifying information to an electronic reader by means of radio waves. An RFID system usually consists of two components: tags and readers. A reader interrogates a tag by sending an electromagnetic (EM) signal, and then the tag sends back its unique identification information or additional data such as product information [7].

There are three types of RFID tags: active, semiactive, and passive, with their main difference being the tag power source. Active and semi-passive RFID tags use internal batteries to power their circuits. An active tag also uses its battery to generate and send its identification signal by itself to a reader, whereas a semi-passive tag relies on the reader to supply its power through backscattering. The passive tag does not have any power source and uses the incident power from the reader to send back the corresponding information signal through backscattering mechanism. As it can be expected, the read range of passive tags is much shorter than active tags, but the active RFIDs require a battery replacement periodically.

RFID technology is exploited in numerous domains, with thousands of applications, including more and more seen in everyday life. Some of these applications are tracking, finance, retail management, sport games, logistics, security and health care, among others. Indeed, the RFID market is worth more than seven billion dollars today, and its growth is

more than 10% per year [8].

0.2. UHF RFID tags

RFID systems use frequencies varying from around 100 kHz to over 5 GHz (Figure 1[1]). The most commonly encountered frequency bands are the 125/134 kHz, 13.56 MHz, 860-960 MHz, and 2.4-2.45 GHz [9]. The working frequency selected for the operation of the tags considered in this work is the ultra high frequency (UHF) which goes from 860 MHz to 960 MHz. Specifically, the European UHF RFID band is regulated in the 865-868 MHz band [10].

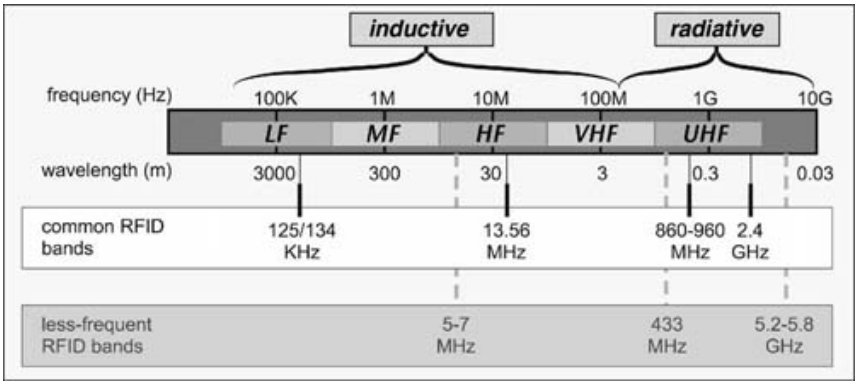

Figure 1: RFID Frequency Bands

The simple and passive nature of UHF RFID tag communication makes it low cost without the need for maintenance and complicated structures. They can be integrated and mounted on numerous objects in a vast range of applications, such as supply chain operations, personal identification, tracking of items, sensing various environmental conditions, medical and health related applications, and military scenarios. Passive UHF RFID tags harvest energy from the reader in order to operate and send data back to the reader with its own embedded unique identification code. However, in passive UHF RFID systems, the backscatter signal is rather weak and therefore more vulnerable to several surrounding factors which are mostly application specific; they involve, for instance, the material properties of the object where the tag is mounted on, such as humidity, water or performance degradation close to metallic objects [11].

0.3. RFID-tag-antenna-based sensing

In the last years, the explosive demand for ubiquitous low-power, compact wireless sensors for Internet-of-Things or ambient intelligence has promoted research efforts to integrate sensors with an RFID-enabled platform [12]. RFID tags are mass produced at a low cost and present an excellent platform on which to fabricate sensors that are low cost and which

[1] this image has been extracted from the book of Daniel Dobkin “The RF in RFID. Passive UHF RFID in Practice”. Newnes ed., Elsevier, 2008. ISBN 978-0-7506-8209-1.

have the potential for pervasive deployment. Sensors, which make minimalistic changes to the RFID tag design itself, lend themselves well to applications in which there is a need for pervasive, low-cost sensing in which the sensor response can be simplistic [13].

Antenna based tag sensing is receiving significant attention due to a simple passive architecture and easily adaptable to existing commercial RFID systems [2]. In fact, RFID sensors that calibrate a change in some physical phenomenon of interest to a change in RFID tag antenna electrical properties have already been studied [13] [14] [15].

The tag-antenna-based sensing paradigm discussed in this thesis has several advantages including low-cost, theoretically infinite lifetime, and is based on standardized communication protocol, all of which are very desirable properties in applications requiring ubiquitous monitoring. However, this technology comes with its own set of limitations. Since these sensors are passive, the range over which they can be read is limited. However, tag-antenna-based sensing can be considered as a viable technology for those application domains in which there is a need for low-cost, ubiquitous sensing in which the sensor response can afford to be simplistic [13].

0.4. Objectives

Characterize the electrical properties of cork in order to obtain reliable values to be used in antenna design process.

Design, through EM software, an RFID tag which uses cork as its substrate. The design process should lead to a conformal RFID tag capable of being inserted inside a cork stopper.

Fabricate the RFID tag design through a fast and cost effective fabrication process, thus obtaining a low-cost tag.

Add temperature sensing capabilities to the RFID tag.

0.5. Work structure

This work is structured as follows: in **Chapter 1** it is described the characterization process of the electrical properties of cork, which involves S-parameters measurements on two microstrip lines placed on cork substrate. **Chapter 2** is devoted to the design and fabrication of several antennas which have cork as their substrate. In **Chapter 3** it is explained the design process of an RFID tag which is aimed to be embbeded inside a cork stopper. Temperature sensing capabilities are added to this RFID tag which is described in **Chapter 4**. Finally, in **Chapter 5** there are shown the measurement results performed on the fabricated antennas and tags involving measurements in an anechoic chamber and in multipath environment.

CHAPTER 1. SUBSTRATE CHARACTERIZATION

Antenna design process requeries to have knowledge of the electrical properties of the material the antenna is composed of. The electrical properties of cork are not well known yet as it has some properties that make it difficult to establish such as being an anisotropic[1] material or having dependence on the water content. In this chapter, a brief description of cork material properties is first made in order to give the reader a better understanding of the behavior and characteristics of the cork. Following, a method involving microstrip lines on cork samples is used to determine the dielectric constant and loss tangent. Finally, this same method is applied on a controlled climate environment using a climatic chamber to determine the dependence of those electrical properties with the amount of moisture present in the material.

1.1. Cork properties

Cork is a material which has been used by mankind for the last 5,000 years and it is a strategic material used for multiple applications, from wine bottles to aeronautics. Cork is the name given to the bark of the cork oak (*Quercus Suber L.*), a tree found mainly in the western Mediterranean. The natural properties of cork offer to the wine industry incomparable insulating characteristics [16]. The most important characteristics are:

- **Lightness:** cork weights just 0.16 g/cm^3 (grams per cubic centimeter). A cork stopper contains about 89.7 % of a gas like air.
- **Flexibility, elasticity and compressibility:** these properties are given by the nearly 750 million cell (40,000,000 cells/cm^3) composing a cork. These cells are static and with a gas mixture within it, like the air, allowing a stopper can be easily compressed (to be inserted into the bottle) and recovers its initial form.
- **Impermeability:** cork is composed of suberin, a hydrophobic substance. Suberin is made up of organic acids due to the presence of which gases and liquids are unable to permeate into the cork. So it makes it impermeable to liquids and practically impermeable to gases.
- **Incorruptibility:** due to its chemical structure, cork presents a high resistance to the action of humidity and, consequently, to the oxidation that it causes. It does not absorb dust and is fire resistant in its natural state.
- **Recyclable and reusable:** cork stoppers can be recycled through being crushed. The resulting granulate can be used in other products such as shoe soles or fishing buoys. The recycled cork cannot be reused in the manufacture of stoppers.

[1] defined by the Oxford Dictionary as "*anisotropic:* having a physical property which has a different value when measured in different directions.". [http://www.oxforddictionaries.com]

Efficient antenna design requires accurate knowledge of the electromagnetic properties of all materials the antenna is composed of. For this reason, a first step to carry out the design of the antenna will be the characterization of the dielectric properties of cork.

Cork is an anisotropic material; so its different axes of anisotropy should be considered when analysing its electrical properties. The piece of cork from which all samples used in this work are derived is shown in Figure 1.1. This is a piece of natural cork, extracted from a cork oak in Portugal. Pieces of cork like this are used to perform natural cork stoppers. Natural cork in general and specifically for this piece of cork, it can be cut into slices in three different directions: radial (parallel to the tree trunk and perpendicular to the radius of the trunk), which corresponds to the axis y-z indicated in Figure 1.1; axial (perpendicular to the direction of the trunk) which is the z-x axis and tangential (parallel to the trunk and parallel to the radius) being the y-x axis. Due to limitations of cutting tools available, only two of these three axes have been considered: the radial and the axial.

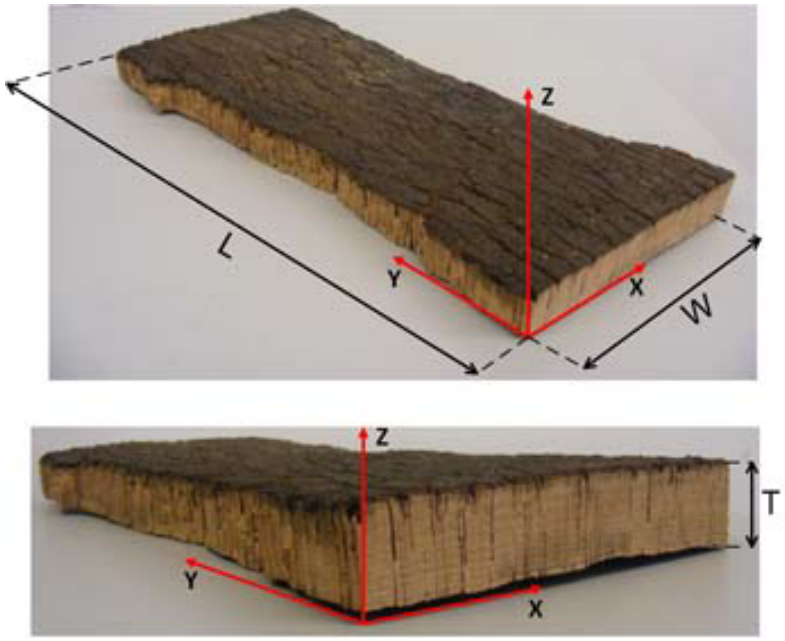

Figure 1.1: Photo of the raw cork piece

1.2. Substrate characterization measurements

In order to determine the dielectric constant and loss tangent, the propagation characteristics of microstrip lines of different lengths placed on cork substrate have been measured, as proposed in [17]. The S-parameters of two microstrip lines of length l_1 and l_2, with $l_2 > l_1$ have been measured. Moreover, in Fig 1.2.b the dimensions of these samples are indicated. Sample thickness varied from 1.5mm to 3mm.

In order to measure its S-parameters, a universal test fixture Anritsu 3680V, available at the laboratory, cannot be used for this substrate, since due to its small thickness and the characteristics of the material, the test fixture compresses the connection area of the microstrip line; furthermore, thicker substrate samples cannot be fit in the universal test

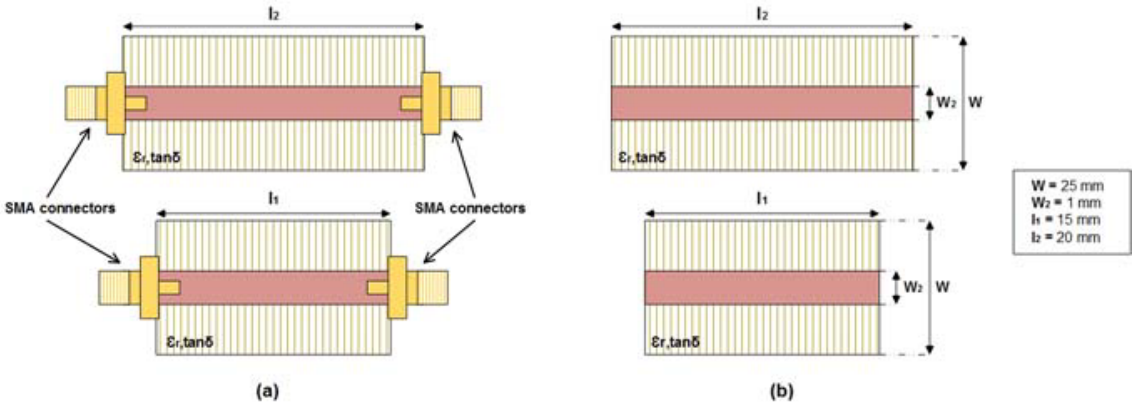

Figure 1.2: (a) two microstrip lines with different lengths, being $l_2 > l_1$. (b) dimensions of the two microstrip lines

fixture. Therefore, it must be used fixed SMA connectors that are nonidentical due to production and soldering inaccuracies, as it is shown in Figure 1.2.a.

The S-parameters measures (see Figure 1.4) were performed using an E8361A PNA network analyzer from Agilent Technologies [18] in the range from 400MHz to 1GHz. Following the method proposed in [17], once the data corresponding to the two-port S-parameters measurements were obtained, the data was computed using Matlab to determine the propagation characteristic (equation 1.1) of the microstrip lines, which is used to obtain the frequency-dependent effective permittivity (1.2).

$$\gamma = \alpha + j\beta \tag{1.1}$$

Having knowledge of the effective permittivity 1.2 and the width (W) and height (H) of the used microstrip lines, the dielectric constant is obtained by solving 1.3.

$$\varepsilon_{r,eff} = \left(\frac{\beta}{k_o}\right)^2 \tag{1.2}$$

$$\varepsilon_{r,eff} = \frac{\varepsilon_r + 1}{2} + \frac{\varepsilon_r - 1}{2}\left[\frac{1}{\sqrt{1 + 12 \cdot (\frac{H}{W})}} + 0.4 \cdot (1 - \frac{W}{H})^2\right] \tag{1.3}$$

Then, the dielectric loss tangent is obtained using formula 1.4. The derived dielectric permittivity and loss tangent were computed based on least-squares fitting. A more detailed explanation of the methodology as well as the implemented Matlab code can be found on Appendix A.

$$tan\delta \approx 0.0366 \frac{\alpha_d \lambda_0 \sqrt{\varepsilon_{r,eff}}(\varepsilon_r - 1)}{\varepsilon_r(\varepsilon_{r,eff} - 1)} \tag{1.4}$$

The results obtained from the measurements performed on the samples of axial and radial axes (see Figure 1.3), are shown in Figures 1.5 (dielectric constant) and 1.6 (loss tangent). Since the cork substrate contain a lot of an air-like gas [16] [19], the dielectric constant is not much larger than one. It is also observed a frequency dependence for the dielectric constant as it have been studied on other works [20]. On the desired frequency range the

value of the dielectric constant is close to 1.7, presenting the axial sample a slightly higher value.

On the other hand, the dielectric loss tangent results show a value of this parameter close to 0.04. Again, the axial sample presents slightly higher values altough in this case the results present a decreasing loss tangent as the frequency increases. These results do not differ significantly from other experiments that can be found in the literature [20] [21]. Therefore, these values will be taken into account when designing the antenna through the electromagnetic simulation software.

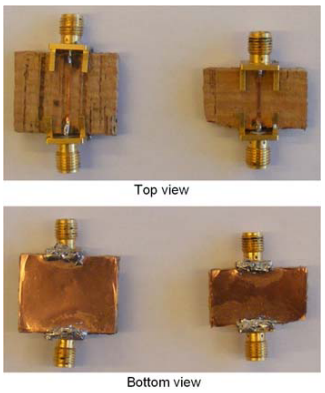

Figure 1.3: Photo of cork samples cut along radial axis. (a) Top view and (b) Bottom view

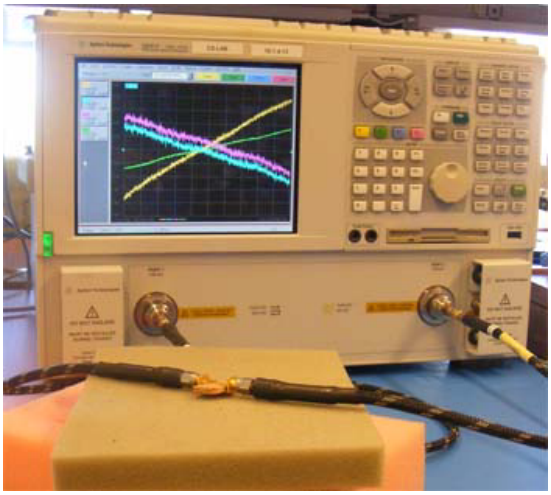

Figure 1.4: measure of a cork sample with a VNA

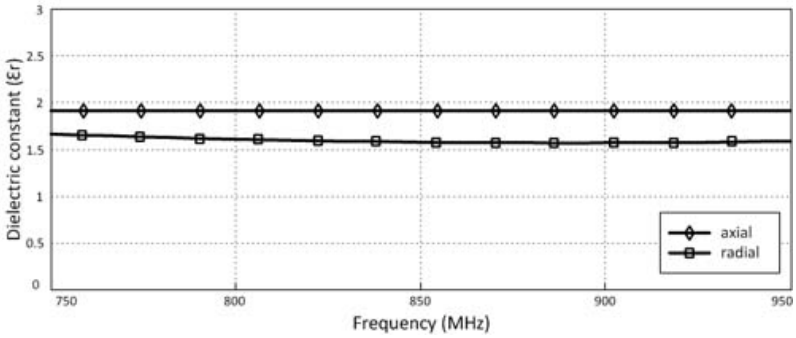

Figure 1.5: Measured dielectric constant

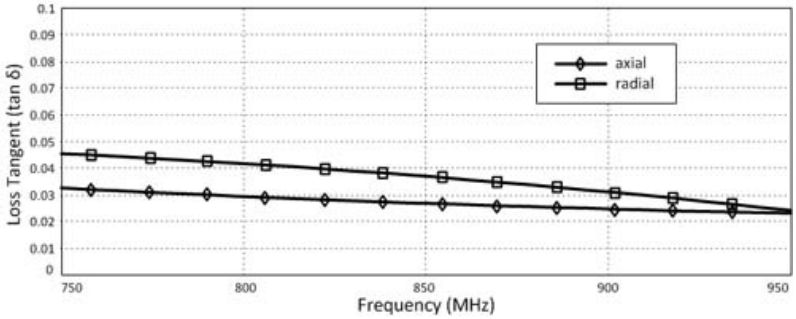

Figure 1.6: Measured dielectric loss tangent

1.3. Measurements in the climatic chamber

Up to now, the measurements have been performed in the lab under ambient room conditions. The electric and in particular the dielectric properties of cork are not well known, although some works can be found in the literature [20] [21] [22] [23]. These publications have shown that the electric and dielectric properties of cork are strongly dependent on the amount of water present in the material. For this reason, measurements on a controlled climatic environment were performed thus trying to establish such dependence.

In fact, temperature and humidity conditions for cork stoppers, specially in wine industry, are encountered in a very specific range. Specifically, the realtive humidity in wine cellars has to be within the range of 50% and 75%, as if it is lower than 50% the cork is dried and if it is higher than 75% can appear fungus. On the other hand, temperature has to be within 7 °C and 25 °C, being the ideal temperature between 15 °C and 20 °C [24].

In order to perform measurements where the temperature/humidity conditions are controlled, it has been used a climatic chamber [25]. In this case, only the samples from the radial axis were measured. The cork samples were introduced inside it and the measurements with the VNA were performed (see Figure 1.7). There were set up two experiments with a controlled temperature/humidity environment. The first experiment consisted of varying the relative humidity in the range from 50% to 80% while keeping a constant temperature value of 18 °C. The relative humidity was increased in steps of 5%. The second experiment consisted of varying the temperature from 7 °C to 25 °C while keeping the relative humidity constant at a value of 70%. In both experiments the temperature/humidity values were kept constant during one hour before realizing the measurement.

Figure 1.7: Climatic chamber measurement setup

The results obtained from the first experiment are depicted in Figures 1.8 and 1.9. It is seen that both dielectric constant and loss tangent suffer a variation when the humidity is changed. Specifically, this variation goes from 1.4 to 1.8 for the dielectric constant and from 0.039 to 0.048 for the loss tangent.

In the other hand, the results from the second experiment (Figures 1.10 and 1.11) show a slight change on the values, being the dielectric constant close to 1.7 in all range and the

loss tangent variation from 0.038 to 0.042. As it is observed, the variations suffered when the temperature is kept constant and the RRHH is changed are substantially higher than in the case where the RRHH is kept constant and the temperature is changed. Those results agree with the literature in the sense that the dielectric properties of cork are dependent on the moisture present in the material.

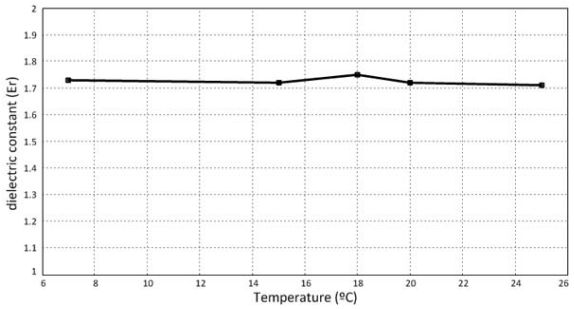

Figure 1.8: Measured dielectric constant in the climatic chamber, where temperature was varied while RRHH was kept constant at 70%

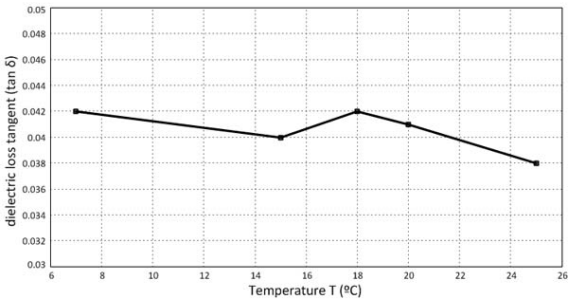

Figure 1.9: Measured dielectric loss tangent in the climatic chamber, where temperature was varied while RRHH was kept constant at 70%

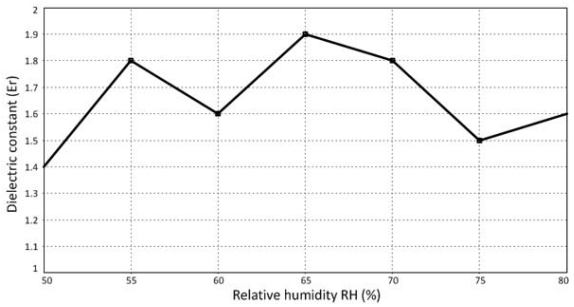

Figure 1.10: Measured dielectric constant in the climatic chamber, where RRHH was varied while temperature was kept constant at 18 Celsius degrees

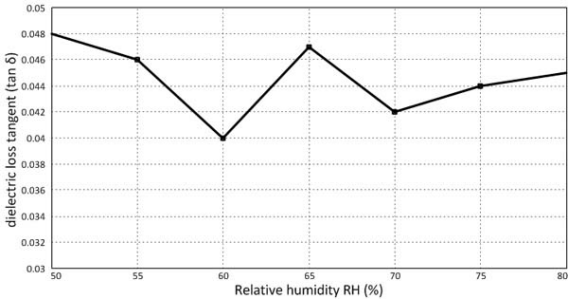

Figure 1.11: Measured dielectric loss tangent in the climatic chamber, where RRHH was varied while temperature was kept constant at 18 Celsius degrees

CHAPTER 2. CORK ANTENNA DESIGN

Cork has specific properties (physical, chemical and mechanical) that confer great potential for new applications. Such applications go from insulation corkboards, agglomerates for wall and floor coverings to shoe soles. Furthermore, cork has been chosen for some aerospace application because of its thermal properties, slow burn rate and shock absorption capacity.

Moreover, there are still unresolved issues related to the design of cost-effective RFID tag antennas for the identification of objects with nonplanar surfaces and unfavourable material content for the operation of the antennas. Objects of this type are encountered frequently in practical applications of RFID, such as in the identification of water or wine bottles. This last case is of particular interest to this thesis because the relationship between cork (stoppers) and wine bottles. In fact, identification of wine bottles with UHF tags is an open field of research and only few papers on this particular field have been published [3] [4] [26]. Given the shape of a bottle, it has been considered that the antenna design should be focused on obtaining an omnidirectional radiation performance thus allowing readings from any direction of the bottle; being at once sacrificed the fact of obtaining a large read range. For these reasons, a dipole antenna has been chosen. Moreover, this type of antenna allows being meandered thus giving more versatility on the shape.

This chapter is focused on the step of designing a meander line dipole antenna which will be used in the tag. The antenna design is in accordance with the shape of a cork stopper, and provides good radiation performance. The first section refers to the design of a straight dipole antenna which will be used to check the validity of the results obtained in chapter 1. The second section describes the design of a meandered dipole antenna, presenting the most relevant parameters that affect the behaviour of the antenna, explaining the steps to achieve the desired shape and presenting simulation results.

2.1. Straight dipole antenna

As have been explained in chapter 1, the accurate knowledge of the electric properties of the material the antenna is composed of is essential when the antenna is going to be designed. This is why a first step on the design of the tag antenna will be the validation of the results obtained regarding the electric properties of cork (this is, permittivity of 1.7 and dielectric loss tangent of 0.04). In order to perform such validation, a simple half-wavelength dipole antenna will be designed and built and its measurement results will be compared with Ansys HFSS, which is the software used to design the antennas and perform the simulations [27]. As explained in chapter 1, the tag antenna is going to be designed in order to work on the European UHF RFID band. So, taking into account that the operation frequency has to be within the range of 865 - 868 MHz, the size of a half-wavelength dipole is calculated using equation 2.1:

$$\lambda = \frac{c}{f} = \frac{3 \cdot 10^8 m/s}{868 \cdot 10^6 Hz} = 0.34m \rightarrow \frac{\lambda}{2} = \frac{0.34m}{2} = 0.17m \tag{2.1}$$

The value of 0.17m obtained in equation 2.1 is calculated in air medium. On the other hand, the length value on cork medium is calculated as follows:

$$\lambda_{cork} = \frac{c}{f \cdot \sqrt{\varepsilon_r}} = \frac{3 \cdot 10^8 m/s}{868 \cdot 10^6 Hz \cdot \sqrt{1.7}} = 0.26m \rightarrow \frac{\lambda}{2} = \frac{0.26m}{2} = 0.13m \tag{2.2}$$

Therefore, the length is expected to be between the value calculated in air medium and the value obtained in cork medium. As a starting point, the upper limit value is introduced in HFSS. An image of the layout is shown in Figure 2.1.

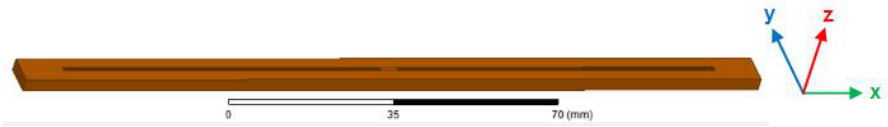

Figure 2.1: Straight half-wavelength dipole antenna design on Ansys HFSS

The properties of the substrate have been introduced in HFSS considering the results obtained in chapter 1, as it is shown in Figure 2.2. The design and its dimensions are shown in Figure 2.3 and Table 3.15 respectively.

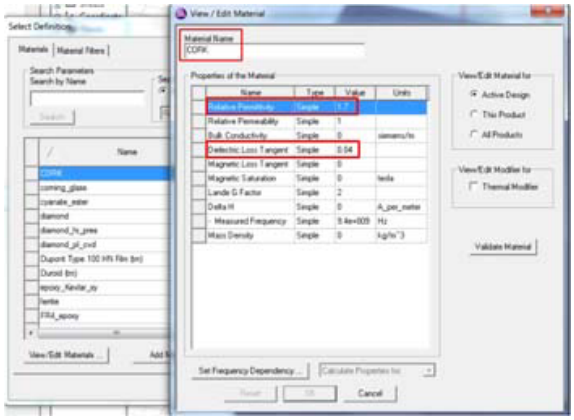

Figure 2.2: Substrate definition on Ansys HFSS

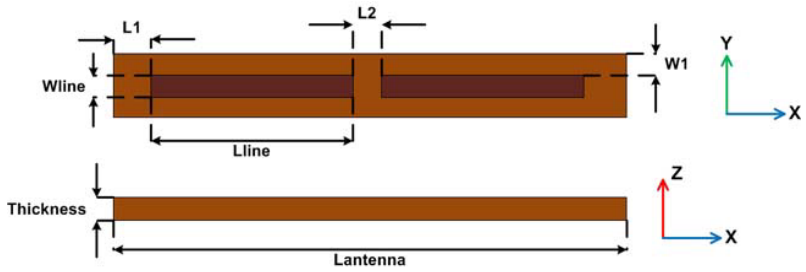

Figure 2.3: Schematic with the straight dipole dimensions

The simulated S_{11} performance of the half-wavelength dipole design is depicted in Figure 2.4. It is indicated that the resonant frequency is at 758MHz, which is around 107MHz lower than expected. Therefore, modifications on the dipole length (between the values calculated previously) should be performed in order to adjust it at the desired frequency.

L_1	L_2	L_{line}	$L_{antenna}$	W_1	W_{line}	thickness
10	4	85	194	3	1	3

Table 2.1: Dimensions in millimeters of the half-wavelength dipole

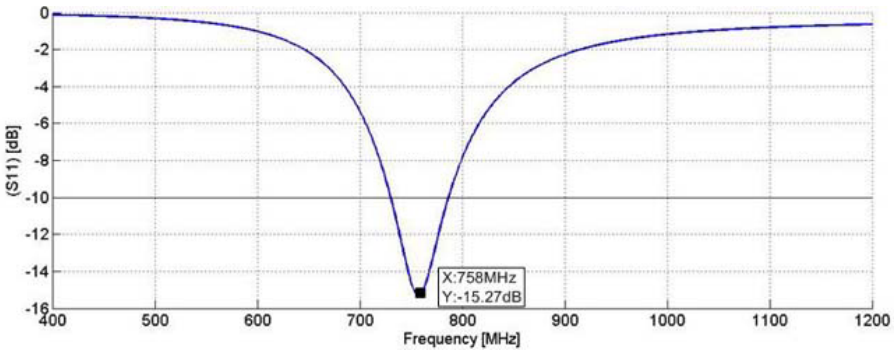

Figure 2.4: Simulated S_{11} performance of the half-wavelength dipole

Following are described the modifications made on the half-wavelength dipole design in order to optimize its performance. Those modifications will bring us a knowledge on what are the critical parameters as well as the amount of change on the antenna behaviour when they are changed. Specifically, the modifications have been performed on the following parameters: dipole length (parameter L_{line}), substrate thickness ($Thickness$) and substrate width (W_1).

2.1.1. Modification on the dipole length

Firstly, a modification on the dipole length was performed. Specifically, the parameter L_{line} from Figure 2.3 was changed from 77mm to 73mm in steps of 1mm. As can be seen in Figure 2.5, the simulation results show a decrease on the resonant frequency as the length is increased. The length that brings a resonant frequency closer to the desired is 75mm. This value will be taken to perform the following simulations.

2.1.2. Modification of the substrate thickness

Another modification that was made, was on the thickness of the substrate. This corresponds to the parameter $thickness$ from Figure 2.3. This value has been changed with values 2mm, 3mm, and 4mm. The simulation results are shown in Figure 2.6. As the changes on the thickness don't affect significantly the behaviour of the antenna, it was decided to set this parameter at the original value of 3mm.

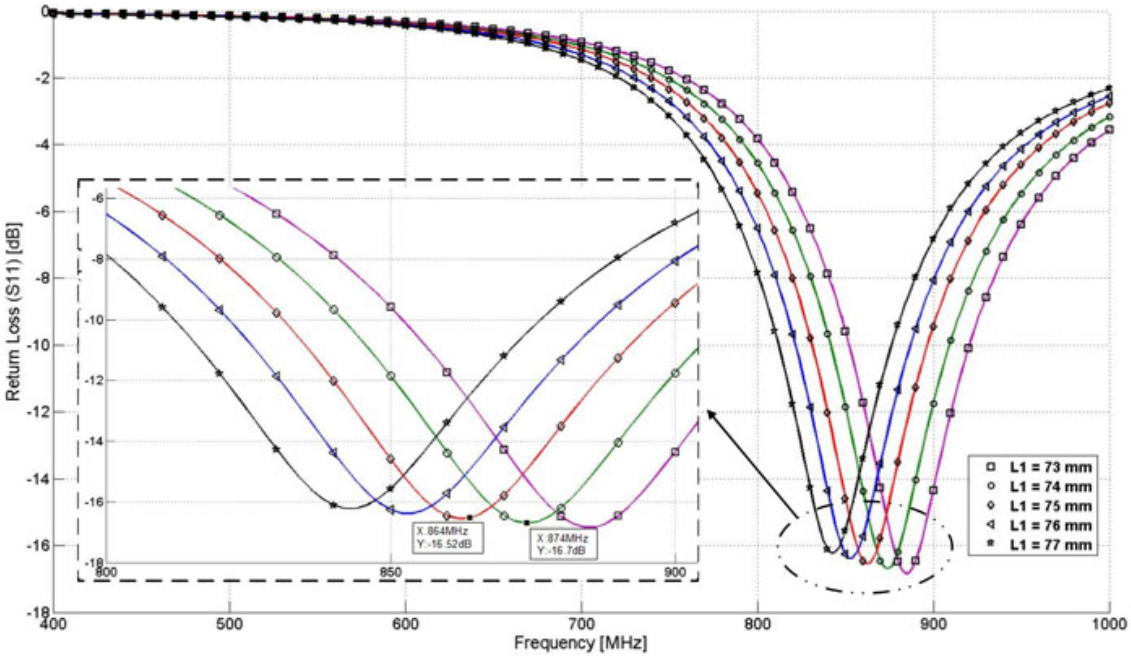

Figure 2.5: Modification on the dipole length

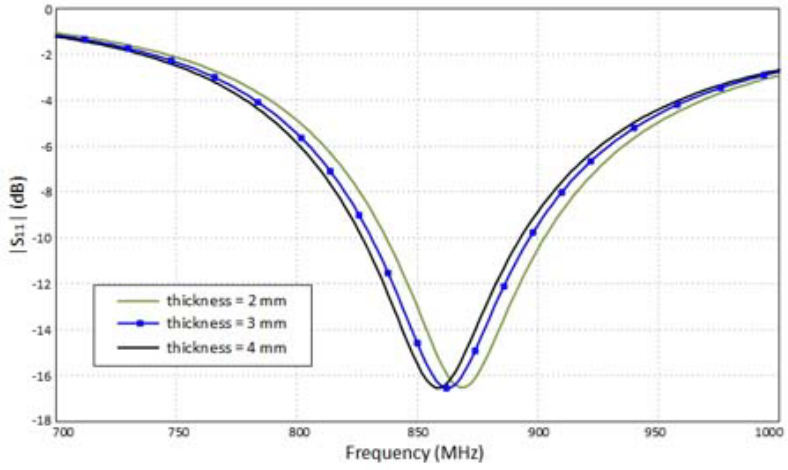

Figure 2.6: Modifications on the substrate thickness

2.1.3. Modification of the substrate width

Finally, the last parameter modified was W_1, which corresponds to the distance between the line and the border of the substrate and, therefore, modifies the total width of the substrate. As can be observed in the simulated S_{11} parameter result from Figure 2.7, the change of this parameter doesn't affect at all the behaviour of the antenna. So it is decided to keep it as short as possible to provide a smaller antenna.

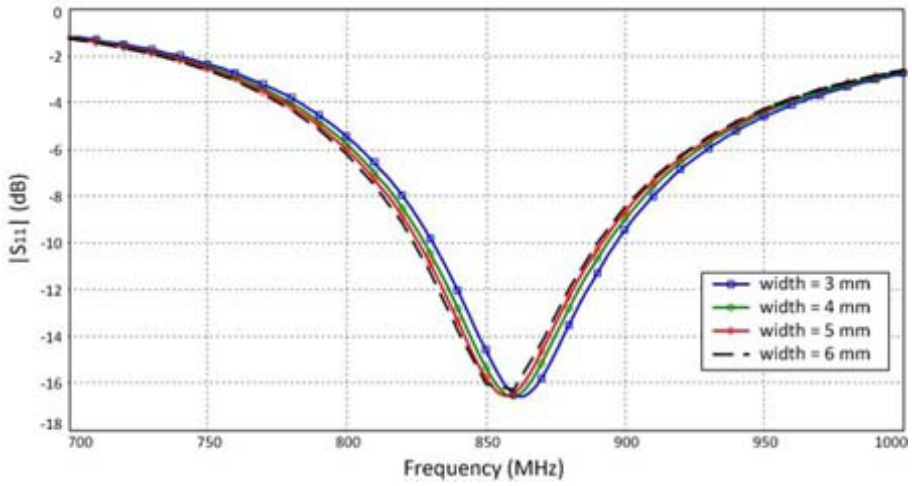

Figure 2.7: Modifications on the substrate width

2.1.4. Final design of the straight dipole antenna

Taking into consideration the modifications made and the results obtained, the design that was built had the dimensions specified in table 2.2. In Figures 2.8, 2.9 and 2.10 are plotted the simulation results corresponding to input S-Parameters, the 3D and 2D radiation patterns, respectively.

Parameter	L_1	L_2	L_{line}	$L_{antenna}$	W_1	W_{line}	**thickness**
Value [mm]	10	4	75	174	3	1	3

Table 2.2: Dimensions in millimeters of the final half-wavelength dipole

From the simulated S_{11} performance it is seen that the antenna is well matched (-16.5dB) at the resonant frequency of 864MHz. It is also observed that it has a bandwidth of 65MHz. On the other hand, the resulting 3D radiation pattern is illustrated in Figure 2.9 where looks kind of like a donut or a bagel with the antenna sitting in the hole and radiating energy outward. The strongest energy is radiated outward, perpendicular to the antenna in the y-z plane. This kind of shape and radiation behavior is the one expected for a dipole. Moreover, in Figure 2.10 there are represented the E and H planes corresponding to the two-dimension cuts of the 3D radiation pattern. The E-plane which is defined for a linearly-polarized antenna as the plane containing the electric field vector and the direction of maximum radiation, in this case coincides with the horizontal/azimuth plane (x-y plane). On the other hand, the H-plane is defined as the plane containing the magnetic field vector

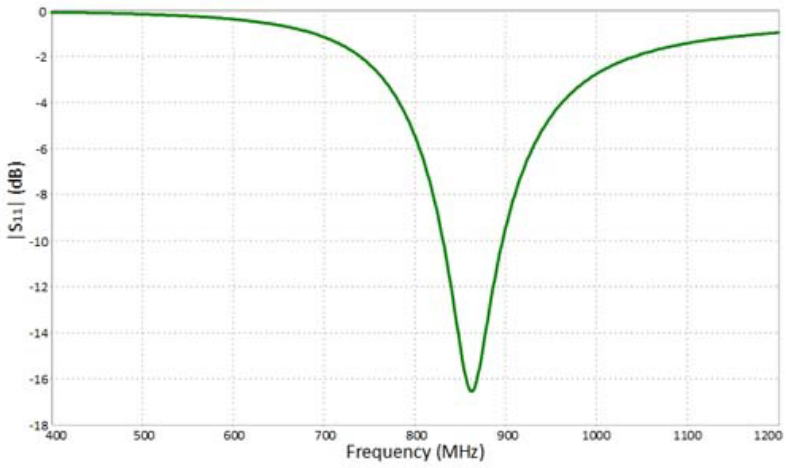

Figure 2.8: Half-wavelength dipole simulated input S-parameters of the final design

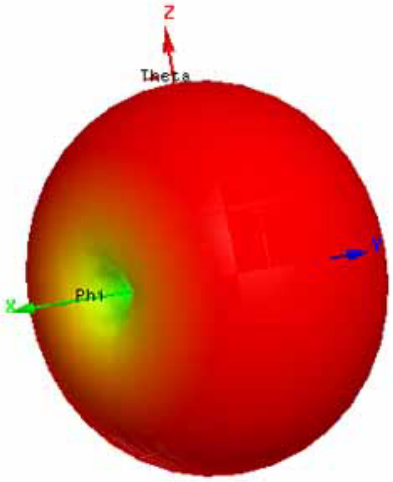

Figure 2.9: 3D radiation pattern of the half-wavelength dipole antenna at 865 MHz

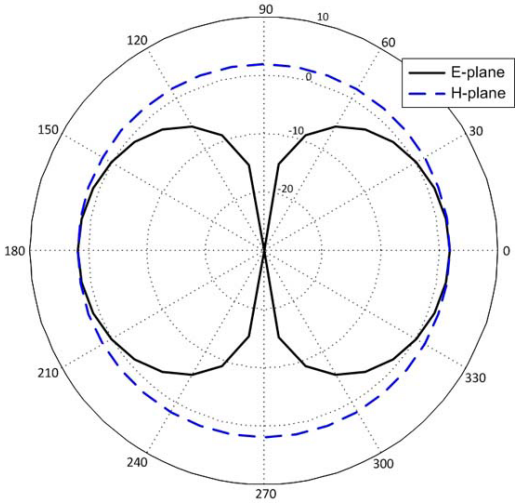

Figure 2.10: E and H Radiation pattern at 865 MHz

and the direction of maximum radiation and coincides with the vertical/elevation plane (z-y plane) [28]. From both E and H planes one can observe that the antenna presents a gain of 1.87dBi.

Moreover, the radiation efficiency provided by HFSS gives a value of 91.18%. The efficiency of an antenna relates the power delivered to the antenna and the power radiated within the antenna. A high efficiency antenna has most of the power present at the antenna's input radiated away. A low efficiency antenna has most of the power absorbed as losses within the antenna, or reflected away due to impedance mismatch.

2.1.5. Fabrication of the straight dipole antenna

The antenna design of previous section was fabricated. The fabrication process for all antennas processed in this thesis has been aimed to be fast and cost effective. In this way,

standard milling fabrication has been used to transfer the antenna design on a low cost adhesive copper tape, which is then attached to the cork substrate, thus providing fast and cost effective fabrication.

Specifically, the layout from HFSS was exported into gerber[1] format to the software CircuitCAM from LPKF Laser&Electronics [29]. This software was used to edit the layout thus setting the copper layer which has to be drilled. Then, the layout was drilled using the $ProtoMat^{\textcircled{R}}C100/HF$ milling machine [30] controlled through LPKF BoardMaster software [31], which is the circuit board plotter processing software included with the milling machine. Once the adhesive copper tape was cut with the milling machine, it was removed using tweezers and glued on cork substrate, which was previously cut from the natural cork sample (see Figure 1.1) using a regular saw. Once the dipole line was placed on the substrate, pressure was applied on it during several hours so that it was completely stucked. Finally, a SMA connector was soldered. The constructed antenna is shown in Figure 2.11.

Once the antenna was fabricated, measurements of its performance were carried out. The measured performance of the antenna is presented in Section 5.1. of Chapter 5.

Figure 2.11: Fabricated straight half-wavelength dipole antenna

2.2. Meandered dipole antenna

In the previous section a straight dipole of 17.4 cm long was considered; this size is too large to provide the antenna with a conformal profile to be embedded into a cork stopper. Therefore, the size of the antenna must be reduced. To achieve such reduction into a dipole antenna, size-reduction techniques can be applied such as meandering.

The straight dipole antenna was folded as can be seen in the layout of Figure 2.12. This folded dipole has the same wire length as the straight dipole antenna, but as it is indicated in Table 2.3 the antenna length has been reduced up to 3.4cm which is about five times less than the length of the straight dipole antenna. However, the performance of the antenna has been reduced significantly and the resonant frequency has increased approximately 320MHz, as can be seen in Figure 2.14. When the dipole is meandered, the direction of the current flow in neighbouring arms of a meander is inverted, so these currents cancel and contribute no radiation [9]. In addition, the inductance of a meandered structure is not the same as those of a straight structure. A densely-packed meandered structure has significantly less inductance per unit length than a straight dipole; this is seen in Figure 2.13. Since the resonant frequency of the antenna is inversely proportional to the product of inductance and capacitance [28], when these are reduced, the resonant frequency is

[1]The Gerber file format is used by printed circuit board (PCB) industry software to describe the printed circuit board images, copper layers, solder mask, legend, drill holes, etc.) [extracted from Wikipedia: http://en.wikipedia.org/wiki/Gerber_format]

increased. A meandered dipole has a higher resonant frequency than a straight dipole for the same wire length, as it happened in this case and as it can be seen in Figure 2.14.

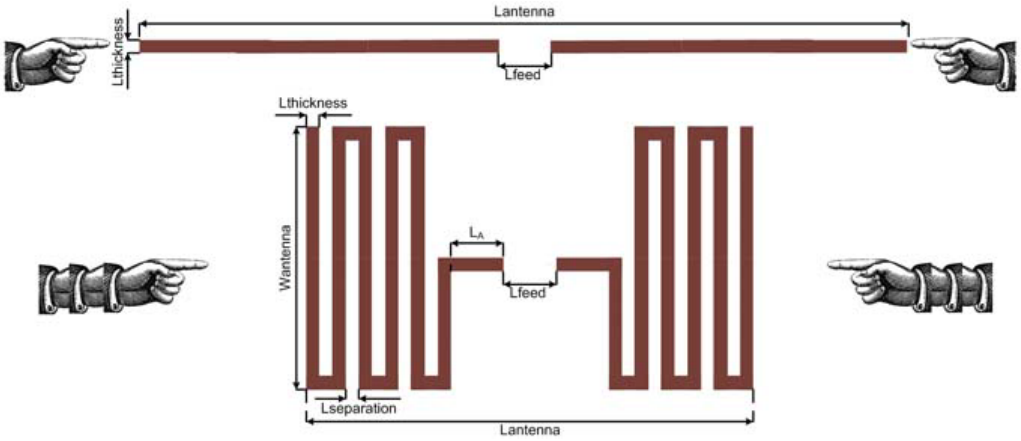

Figure 2.12: The straigth dipole can be made shorter by bending the wires

Antenna type	$L_{thickness}$	$L_{separation}$	L_A	L_{feed}	$L_{antenna}$	$W_{antenna}$
Straight	1 mm	–	–	4 mm	154 mm	–
Meandered	1 mm	1 mm	4 mm	4 mm	34 mm	20 mm

Table 2.3: Comparisson of the dimensions of the straight and meandered dipole antennas

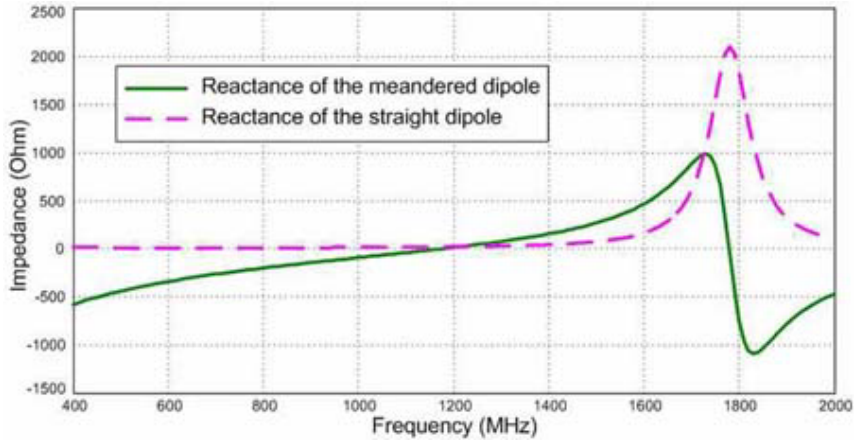

Figure 2.13: Reactance of the input impedance of the straight and meandered dipole

	Straight	**Meandered**
Radiation efficiency	91.18%	35.42%
Gain	1.87 dBi	-2.9 dBi

Table 2.4: Radiation efficiency and gain of the straight and meandered dipole

In table 2.4 there are indicated the radiation efficiency and the gain of both designs, the straight and the meandered dipoles. As it is seen, the performance of the meandered dipole worsened significantly as it has poor values of efficiency and gain. Therefore, in order to achieve a better performance, less bending was practised on the antenna. Several layouts were designed (see Figure 2.15) and its corresponding simulation results are

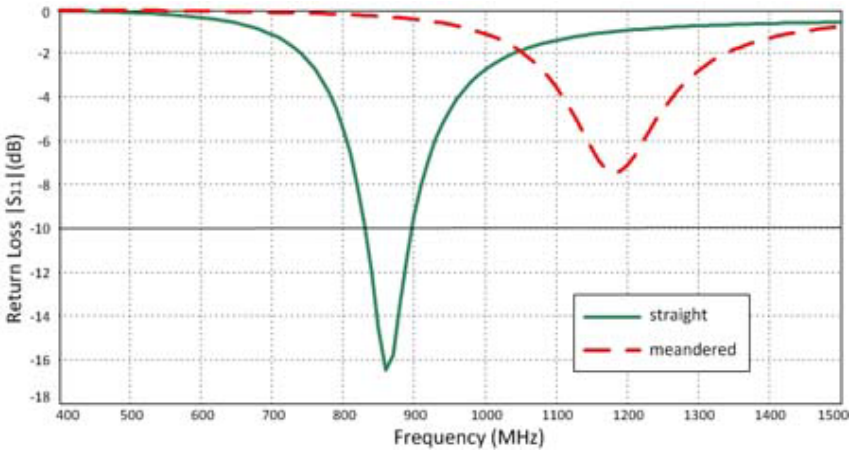

Figure 2.14: S_{11} simulation results of the straight and meandered dipole

depicted on Figure 2.16. On Table 2.5 there are indicated the values obtained from the simulations corresponding to the radiation efficiency and gain of the different layouts. It can be appreciated that as more meanders are introduced, the worse the performance. The design that offers a better result is the layout (c) , but what happens is that is the layout with less meanders and thus it is still too large. However, layout (b) offers also a good performance and in this case the design has enough meanders to provide a feasible shape and size. It would be interesting to provide a more compact shape by means of introducing more meanders, but as it is showed, the performance worsened considerably. So, at this point it was decided to bend the arms of layout (b) (parameter L_{arm} in Figure 2.17) along the Z axis (vertically), thus providing a cube shape.

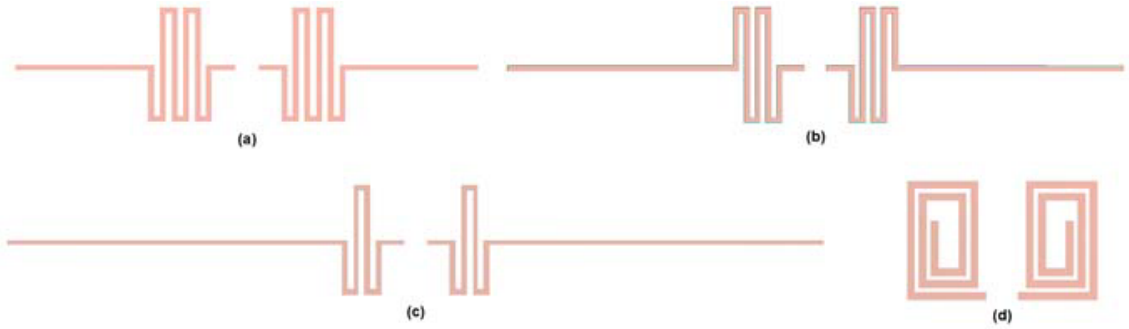

Figure 2.15: Several meandered antenna layouts

	Layout a	**Layout b**	**Layout c**	**Layout d**
Radiation efficiency	61.4%	72.77%	87.4%	6%
Gain	-0.5 dBi	0.41 dBi	1.33 dBi	-10.7 dBi

Table 2.5: Radiation efficiency and gain of the layouts depicted in Figure 2.15

L_{arm}	$L_{thickness}$	$L_{separation}$	L_A	L_{feed}	$L_{antenna}$	$W_{antenna}$
41 mm	1 mm	1 mm	4 mm	4 mm	112 mm	20 mm

Table 2.6: Dimensions of the design of Figure 2.17

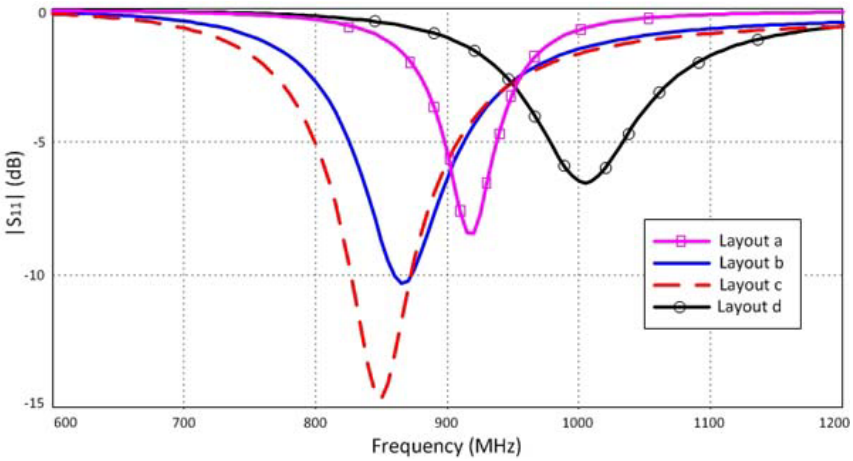

Figure 2.16: Input S-Parameters of the layouts from Figure 2.15

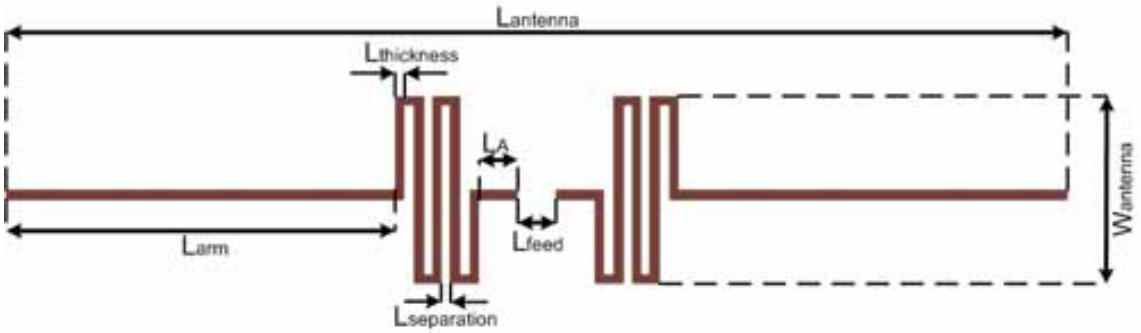

Figure 2.17: Meandered dipole

2.3. 3D meandered dipole antenna

As indicated in the last section, the arms (corresponding to parameter L_{arm} of Figure 2.17) were bended vertically along the Z axis. This was to ensure that the total size of the design was compacted thus providing it with a cube shape. This type of form is more like a cork stopper, so this antenna design is more likely to be conformal with this kind of shape. The layout from HFSS of the bended design is shown in Figure 2.18.a. This new design achieved a more compact form thus making it feasible to be inserted into a cork stopper, but it involved its consequences. As depicted in Figure 2.18.b its performance was worsen significantly. It is observed a significantly mismatch after the bending which leads to a worse performance. The fact of bending those arms also introduced a resonance on the impedance which affected its matching; the real part decreased by means of half of the previous value while the imaginary part increased. Therefore, some changes had to be made in order to optimize the tag.

2.3.1. Modification of the line length along the Z axis

In order to improve its performance, some modifications were carried out on the antenna. Those modifications were made on the lines which have been bended along the Z axis.

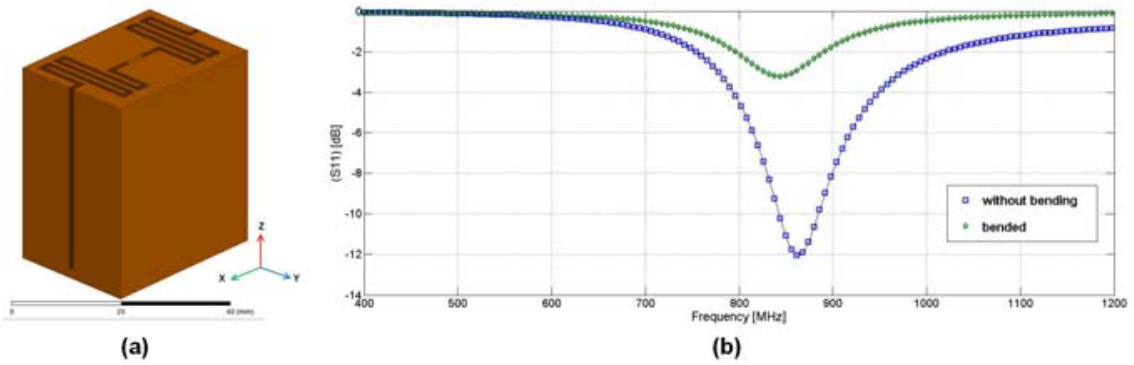

Figure 2.18: (a) - Ansys HFSS layout of the 3D meandered dipole (b) - S_{11} performance of the 3D meandered dipole and the 2D meandered dipole

First of all, it was changed its length being its current value of 37mm. The length was changed from 30mm to 40mm in steps of 1mm. Figure 2.19 shows the results on the S_{11} performance of those changes; as it is observed the change on the line length does not provide any improvement on the S_{11} performance while sets the resonant frequency. As it is highlighted, the line length which provides the desired resonant frequency is for a value of 35 mm.

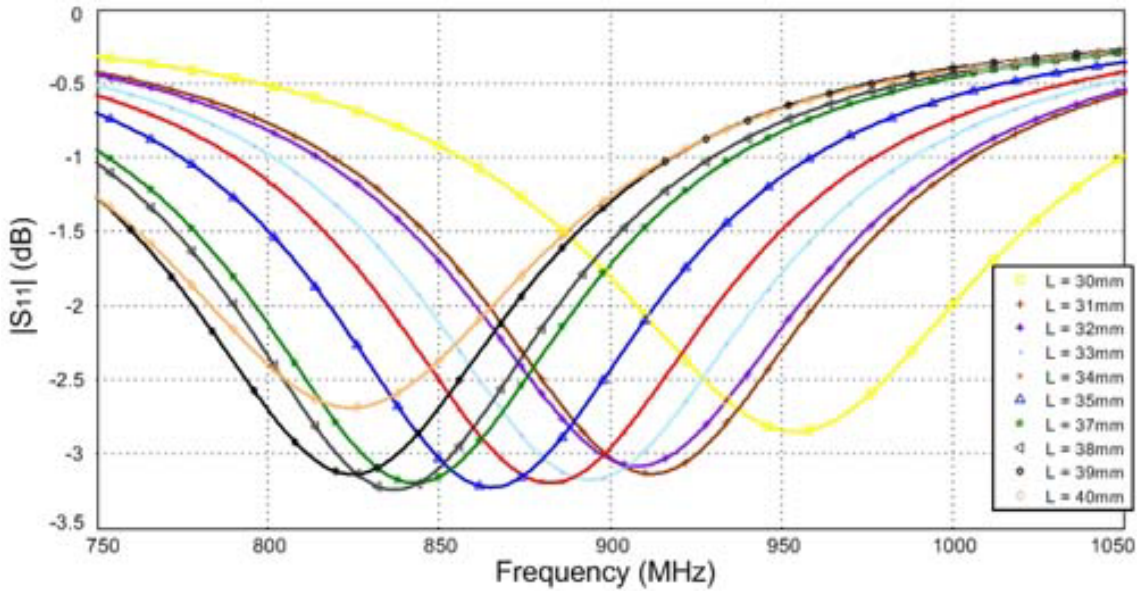

Figure 2.19: Change on the line's length

2.3.1.1. Lines joint at the bottom

Another change performed on the length of those lines was to bring both of them to the bottom of the tag, as it is indicated on Figure 2.20; notice that this is a semi transparent design in order to appreciate the changes on the lines. The result of this modification is depicted on Figure 2.21 and as it can be seen it improved slightly the S_{11} performance and brought closer the resonance frequency to the one desired.

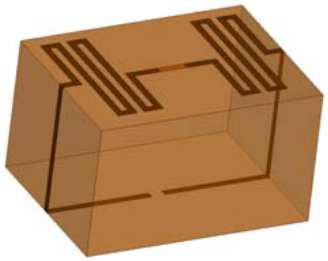

Figure 2.20: Ansys HFSS layout of the lines joint at the bottom

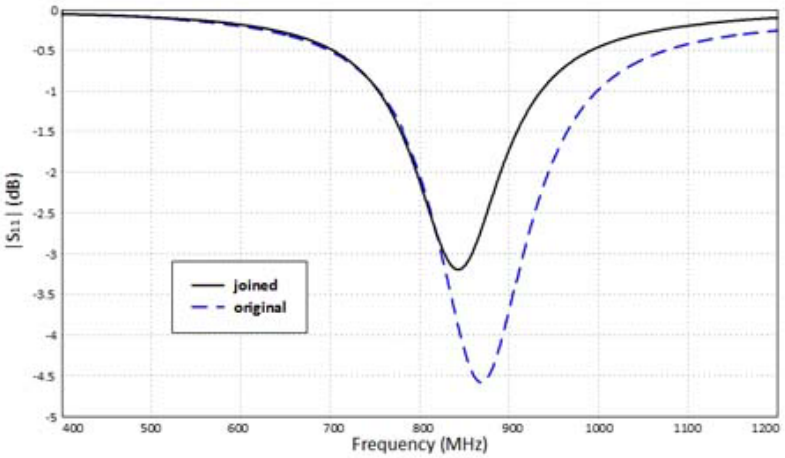

Figure 2.21: Input S-Parameters of the 3D meandered dipole and the design with the lines joint at the bottom

2.3.1.2. Square form at the end of the lines

Finally, one last change was done on the line (parameter L_{arm} of Figure 2.17). In this case it was considered the current value (37mm) which makes the tag too large for our purposes. So it was thought to reduce the overall size (not the length) by means of folding the end of the line in a way that draws a square form (see Figure 2.22). Performing this change meant an improvement on the S_{11} matching while the overall size of the tag was reduced significantly. Specifically, the tag of Figure 2.22 has dimensions of 34x25x18mm (considerably smaller than the 34x25x39mm from the tag of Figure 2.18.a). Taking into account the said results, it was decided to continue with this tag design and to perform on it some changes in order to optimize its behaviour. The modifications done are commented on the following section.

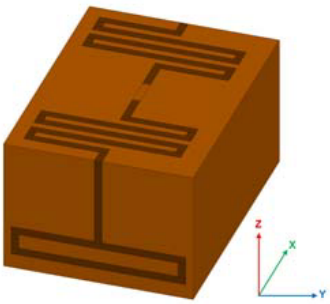

Figure 2.22: Ansys HFSS layout of the 3D meandered dipole with a square form at the end of the lines

2.3.2. Modification on the symmetry

Up to now, the design presented symmetry along its X axis (see Figure 2.24.a). What was done with this modification was to change its symmetry resulting both sides of the top face opposed to each other as it is illustrated in Figure 2.24.b. Figure 2.25 shows the

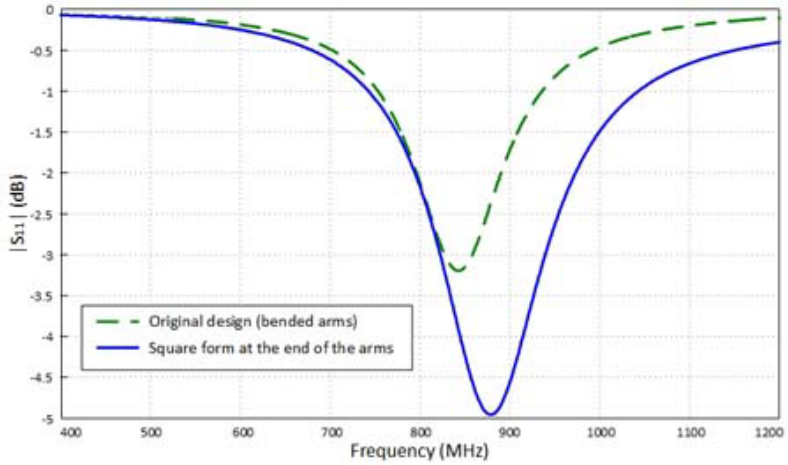

Figure 2.23: S_{11} performance of the original 3D meandered dipole and the meandered dipole with a square form at the end of the lines

simulation results corresponding to this modification compared with the original design and the design of the previous section 2.3.1.2. It is seen that this modification on the symmetry results in a slightly improvement, not being this remarkable enough to be considered; as it should be considered the disadvantages of this modification, such as loss of usable space to accommodate there in the future passive components or other devices.

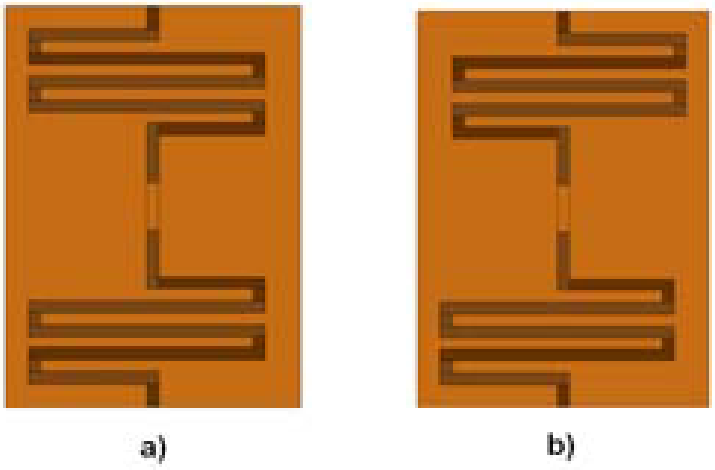

Figure 2.24: a) original design - b) modification on the symmetry

2.3.3. Modification on the line width

The current width of the line is 1mm (consider parameter $L_{thickness}$ from Figure 2.17). This parameter has been reduced up to 0.75mm and 0.5mm respectively. The results (Figure 2.26) show an improvement on the performance as the width of the lines decreases. Moreover, this change results in a significantly reduction on the overall size of the antenna. Actually, the reduction from 1mm to 0.5mm of the width of the line means a reduction of 50mm of the antenna size. Therefore, this parameter is considered as important as it provides many benefits. Due to milling machine constraints, it is not possible to provide a

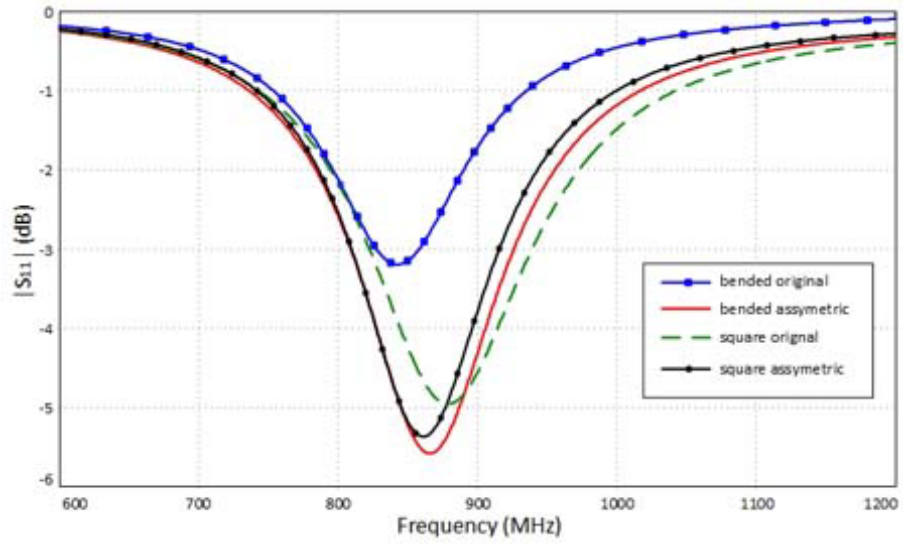

Figure 2.25: Input S-parameters of the original designs and the assymetric designs

width of 0.5mm due to the drill cannot operate with as little thickness. So it was decided to provide a width of 0.75mm.

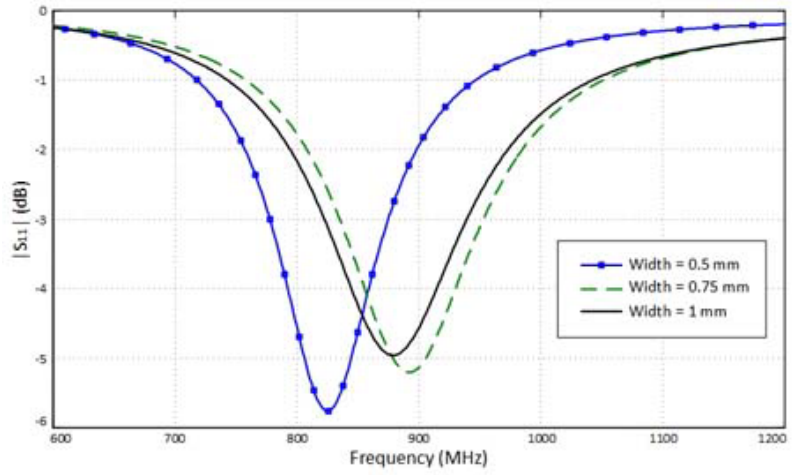

Figure 2.26: Change on the line width

2.3.4. Modification on the meanders separation

The same way as the width of the lines, the meanders separation (consider parameter $L_{separation}$ from Figure 2.17) is a critical parameter as it also conditions the overall antenna size. The current separation is 1mm and the modifications made this separation of 0.75mm and 0.5mm. As it can be observed in the results obtained (Figure 2.27), as the separation decreases the performance of the tag becomes worse, especially in the case of a separation of 0.5mm. In the case of 0.75mm it is seen that it has slightly effect on the S_{11} performance and it moves closer to the desired resonant frequency. Taking into account this and also considering that this little decrease in the separation of the meanders

is translated into a significant reduction on the overall tag size, it was decided to change the meanders separation from 1mm to 0.75mm.

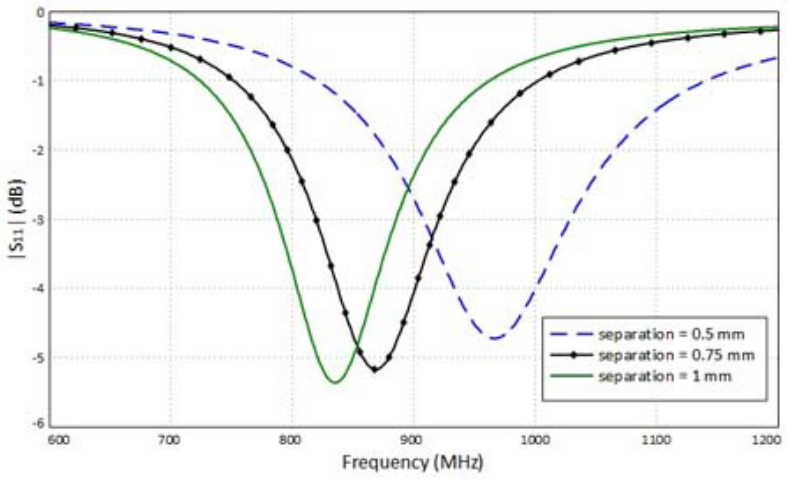

Figure 2.27: Change on the line (meanders) separation

2.3.5. Modification on the feed position

As can be seen in Figure 2.18.a, the tag is fed at the centre of the top face. So far it has been designed in order to be placed a SMA connector, like it was done with the straight dipole of previous section thus allowing being tested its S_{11} performance using coaxial cable and a VNA. Later it will be considered to be modified in order to be placed a passive RFID chip. It was thought to made modifications on this parameter as it could bring some benefits as giving more free physical space at the centre of the tag. This space could be used later, for instance, to introduce more meanders. It was modified to bring it from the centre to the top and at the bottom, respectively. The results on these changes are depicted on Figure 2.28. and it is shown that although a modification on this parameter improves slightly the S_{11} performance, it also brings lower the resonant frequency. So, considering the results obtained it was decided to leave this parameter in its original state.

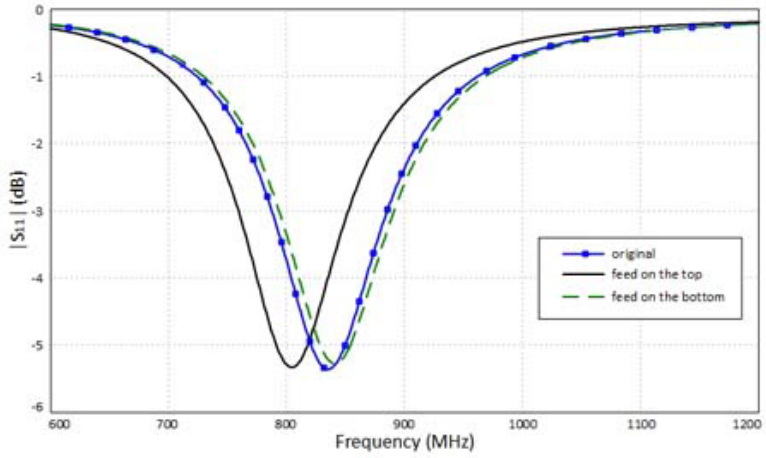

Figure 2.28: Change on the feed position

2.3.6. Final design

Up to this point and considering all the modifications made, it was decided to build the antenna which is shown in Figure 2.29. Its layout with the dimensions is shown in Figure 2.30. If the reader pays attention will notice that this design incorporates those modifications described above which have result in a better performance. That is, a separation between meanders of 1mm, a line width of 0.75mm and a square form at the end of the line along the Z axis.

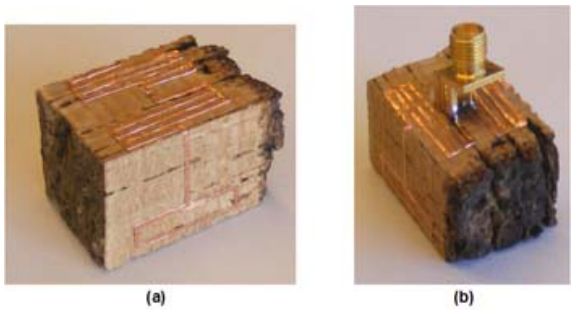

Figure 2.29: Photograph of (a) cube antenna without connector and (b) cube antenna with SMA connector

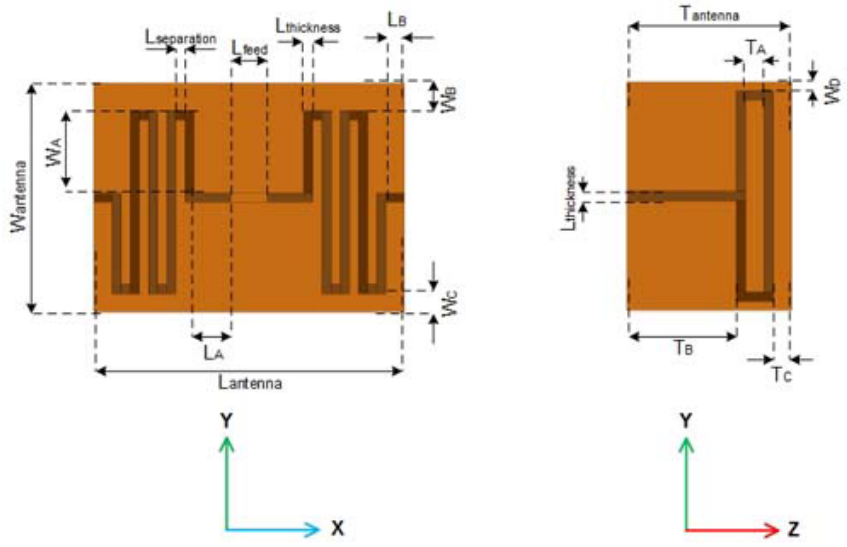

Figure 2.30: Layout of the cube antenna

2.3.7. Antenna insertion in cork stopper

The final step was the introduction of the 3D meandered dipole antenna into a cork stopper. Because of the antenna dimensions it was not feasible to be embedded into a bottle cork stopper, therefore it was decided to consider a barrel cork stopper which is larger. The used stopper with its dimensions is depicted in Figure 2.32. In order to introduce the antenna inside, a rectangular hole according with the antenna dimensions was made in the top of the stopper. The resulting stopper with the antenna inside is shown in Figure 2.33. In Chapter 5 can be found the measurement results on this design.

	Antenna dimensions
$\mathbf{W}_{antenna}$	25 mm
$\mathbf{L}_{antenna}$	32 mm
$\mathbf{T}_{antenna}$	18 mm
$\mathbf{L}_{thickness}$	0.75 mm
$\mathbf{L}_{separation}$	1 mm
$\mathbf{L}_{feed}$	4 mm
$\mathbf{L}_{A}$	4 mm
$\mathbf{L}_{B}$	2 mm
$\mathbf{W}_{A}$	9 mm
$\mathbf{W}_{B}$	3 mm
$\mathbf{W}_{C}$	2 mm
$\mathbf{W}_{D}$	1 mm
$\mathbf{T}_{A}$	2 mm
$\mathbf{T}_{B}$	12 mm
$\mathbf{T}_{C}$	2 mm

Table 2.7: Dimensions of the cube antenna

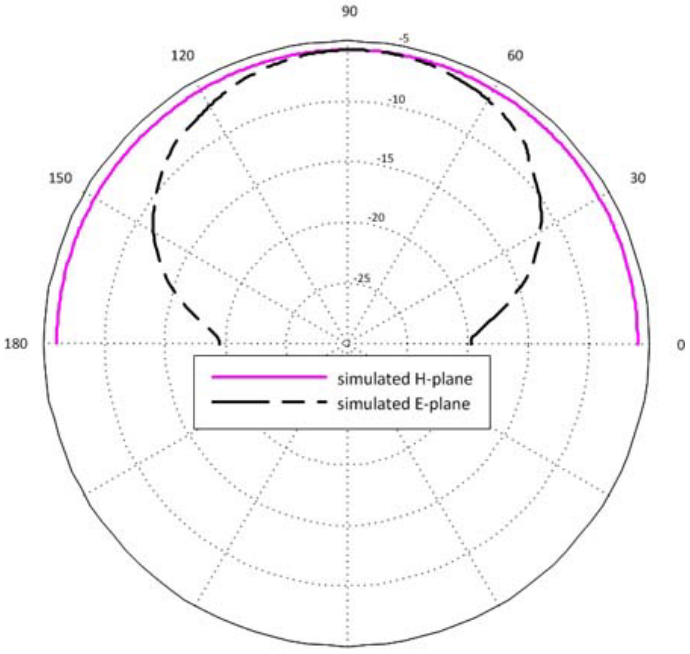

Figure 2.31: Simulated radiation pattern at 868 MHz of the cube antenna

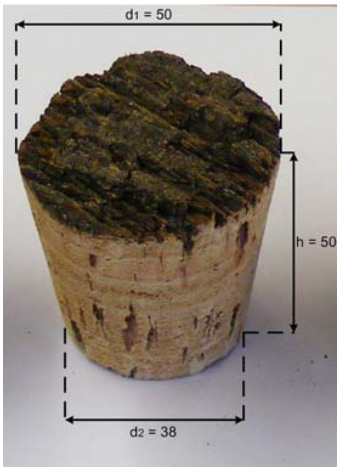

Figure 2.32: Barrel cork stopper

Figure 2.33: (left) - barrel cork stopper with the hole. (right) - cube antenna inside the cork stopper

CHAPTER 3. TAG ANTENNA DESIGN

In the last chapter various antennas placed on cork substrate have been designed and manufactured. Among others, a three dimensional meandered dipole antenna has been achieved, providing compact size, low profile and remarkable performance. This chapter will go on to describe the design of a RFID tag which uses the said antenna. First, the passive RFID chip that will be used for the tag will be presented. Then, changes on the antenna design will be performed in order to maximize the power delivered to the tag IC to turn it on. To achieve this, matching structures and mechanisms will be used as well as the introduction of an additional meander in order to obtain impedance matching between the tag antenna and the tag IC. In all cases, simulations are carried out to verify the effects of such modifications and achieve an optimized design. Last, the final tag design is presented with its simulation results and then it is manufactured.

3.1. UHF transponder chip

Maximum power transfer from the tag antenna to the tag IC is of vital importance since passive RFID tags operate in a power-constrained environment created by electromagnetic compatibility regulations and the power required to operate the tags is obtained from the incident electromagnetic waves. Therefore, it is important to consider the load to which a tag antenna must provide power. The typical input impedance of UHF transponder chips is highly reactive (e.g. $Z_{chip} \approx 20 - 200j\ \Omega$) due to the need of storing information and energy [32].

The selected UHF transponder chip to be used in this thesis has been the $Higgs^{®}$ 3 from Alien Technology [33]. This IC is EPCglobal Gen2 and ISO/IEC 1800-6c compliant [34] [35], has exceptional operating range (up to 10 m), requires low power to perform reading operation and has worlwide operation in the RFID UHF bands (860-960 MHz). Some of its main characteristics are depicted in Table 3.1.The input impedance of the $Higgs^{®}$ 3 RFID chip can be modeled as a parallel equivalent circuit with a resistance R of 1500 Ω in parallel with a 0.9 pF capacitor C. The chip capacitive reactance can be described as in equation 3.1. Then, the complex impedance Z can be calculated using the equation 3.2 and this results in a series equivalent circuit impedance for the 865 MHz frequency of 27.35-j200.7Ω.

$$X_C = -\frac{1}{2 \times \pi \times f \times C} \tag{3.1}$$

$$Z = \frac{R \times X_C^2}{R^2 + X_C^2} - j\frac{R^2 + X_C}{R^2 + X_C^2}\Omega \tag{3.2}$$

In order to verify this result, the equivalent parallel circuit was simulated using ADS (see Figure 3.1) [36]. The simulation result is depicted in Figure 3.2 and it can be seen that is in good agreement with what is get through analytical analysis.

Once the chip input impedance is well known, the following sections of this chapter will be devoted to describe the modifications on the antenna design in order to provide conjugate

Parameter	Min	Typ	Max	Units
Operating Conditions				
Operating Temperature	-50		+85	^{o}C
Operating Frequency	860		960	MHz
Electrical Characteristics				
Sensitivity		-18		dBm
Equivalent input resistance		1500		Ohm
Equivalent input capacitance		0.9		pF

Table 3.1: Operating conditions and electrical characteristics of the Higgs 3 RFID tag IC

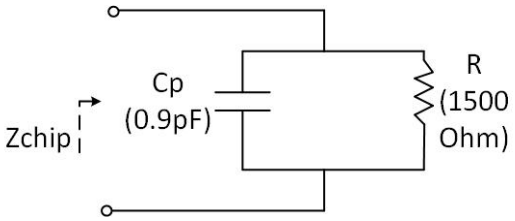

Figure 3.1: IC parallel equivalent circuit

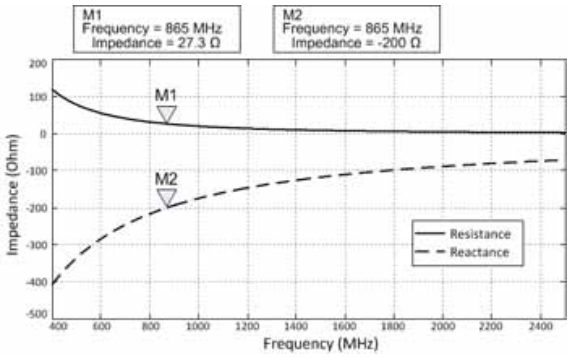

Figure 3.2: Simulation result of the chip input impedance

matching between tag antenna and chip impedances and, thus, maximum power transfer. It is well known that in order to provide maximum power transfer, the real part of the source and load impedances must be the same, and the complex parts must have the same magnitude but opposite signs; in this case, it is said that the two impedances are *complex conjugates*, differing only in the sign of the imaginary part. This statement is known as the *maximum power transfer theorem* [37]. Therefore, if the chip impedance is capacitive (negative reactance) then the antenna must be inductive (positive reactance) in order to obtain conjugate matching. In this case, as the chip impedance is 27-j200Ω, the antenna design will be modified to obtain an impedance of 27+j200Ω.

3.2. Impedance-matching techniques

Several changes were carried out on the antenna design to improve the performance of the RFID tag, as mentioned in the previous section. In Figure 3.3 it is shown the input impedance of the 3-D meandered dipole antenna described in the previous chapter (see Section 2.3. from Chapter 2); as can be observed, it has a capacitive behavior in the UHF band (865-868 MHz) while the resistance is about 10 Ω. Therefore, the resistance should be doubled while the reactance should increase up to 200 Ω in order to reach the desired impedance of 27+j200Ω.

To obtain a low-cost device, it is not feasible to use external matching networks involving lumped components. Therefore, the matching mechanisms have to be embedded within

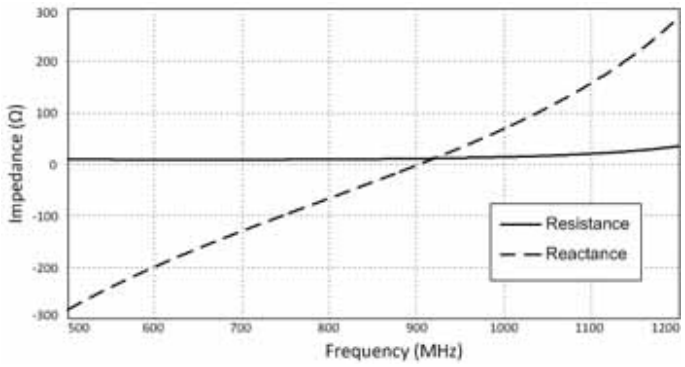

Figure 3.3: Input impedance of the 3D meandered dipole antenna

the tag's antenna layout. In order to adapt the tag antenna to the capacitive IC load, several feeding strategies were adopted for antenna tuning following published studies on impedance-matching techniques in UHF RFID antennas [9] [38]. Those used are the T-Match structure, an inductively coupled loop and the addition of another meander in the central zone of the antenna's top face. All of these techniques used are described in the following subsections.

3.2.1. Inductively Coupled Loop

One strategy followed was to source the radiating dipole via an inductively coupled small loop placed in close proximity to the radiating element. Thus, the terminals of the loop can be directly connected to the chip. This arrangement adds equivalent inductance in the antenna. The strength of the coupling, and therefore of the added reactance, is controlled by the distance between the loop and the dipole, as well as by the shape of the loop. The inductively coupled loop placed on the considered antenna is illustrated in Figure 3.4. The distance d and the length b of the loop were varied and the results of the simulations performed are depicted in Figure 3.5. One can observe that the resistance is reduced when the loop-dipole distance increases, altought it is a little remarkable decrease. Indeed, a proper loop-dipole distance to match the chip's resistance cannot be obtained due to physic space constraints. Further on, one could select the loop size with the purpose of canceling the chip's capacitive reactance, but that would not be enough to achieve the desired inductance value. As it is seen, altough it presents an inductive behavior this is not high enough. Considering these results, this technique was ruled out.

3.2.2. T-Match

This impedance-matching technique can be described as a direct coupling of the loop commented on the previous section. In this case, the distance d to the loop is equal to zero. Such structure was placed on the considered dipole antenna in the simulation process as it is shown in Figure 3.6. Such layout and the modifications performed were simulated in HFSS.

It is known that the shape and separation of the second conductor has a considerable

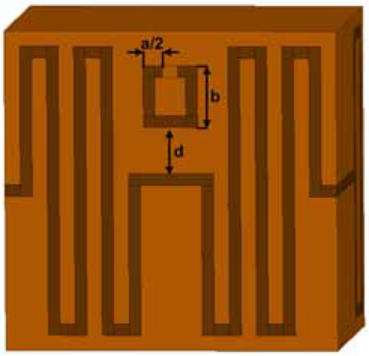

Figure 3.4: Antenna design with a coupled loop

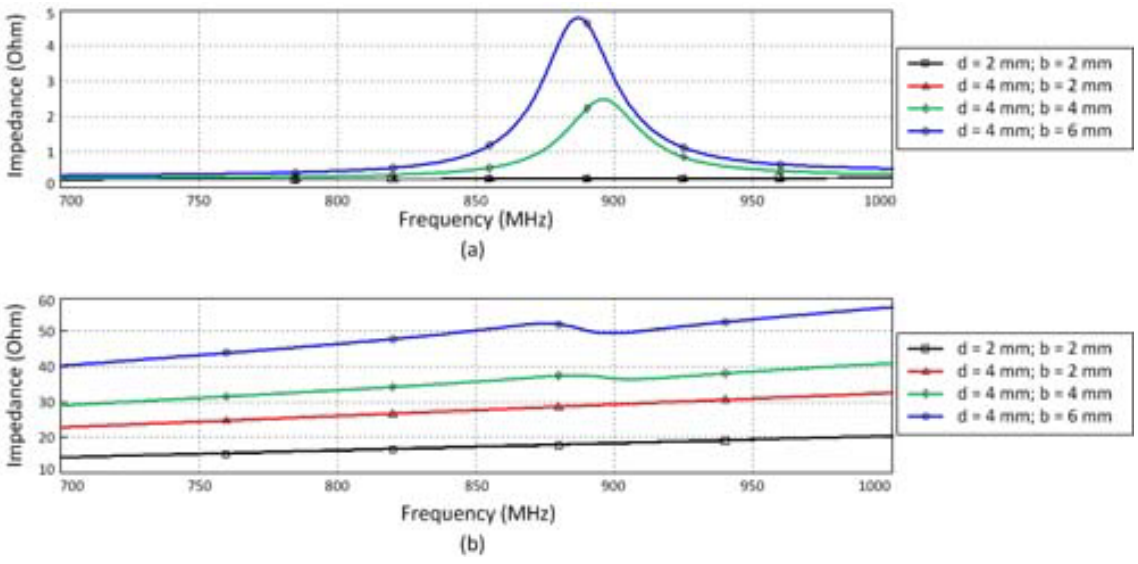

Figure 3.5: Simulated impedances from the changes on the coupled loop. (a) resistance and (b) reactance

effect on the resulting antenna impedance [38]. This can be checked taking a look at Figure 3.7 where it is depicted the results obtained on varying the values a and b. It is seen that an increase on the distance between the dipole and the loop is translated into an increase of the antenna impedance. Despite this, the impedance achieved by means of modifying those values is not high enough to reach the desired value. Therefore, optimum impedance matching could not be provided through the use of this technique.

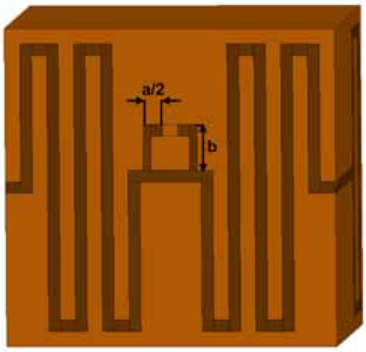

Figure 3.6: Antenna design with T-Match structure

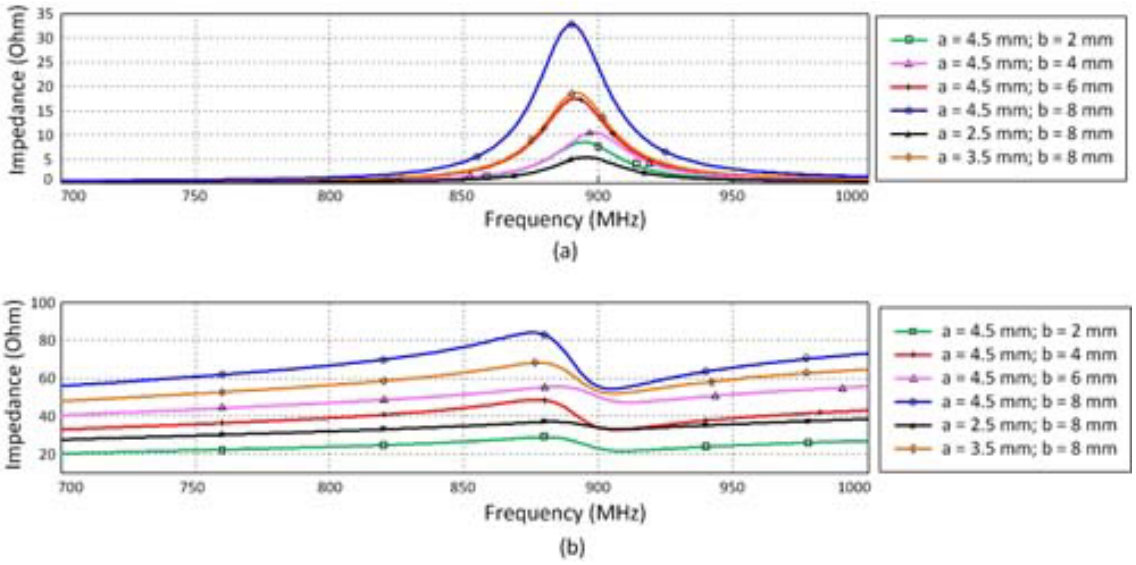

Figure 3.7: Simulated impedances from the changes in the T-Match structure. (a) resistance and (b) reactance

3.2.3. Meandering

Considering previous modifications which did not achieved optimum results, in this case was considered to add another meander. Specifically, the antenna layout was modified to bring the feeding in the top position. Then, an additional meander was added on the central zone of the tag, taking profit of the free space that was there. In Figure 3.8 it is represented this new design with an additional meander. In this representation there are specified different parameters that will be considered in following subsections. Those parameters are $L_{separation}$, which corresponds to the distance between the central meander and the

neighbour meander; $L_{thickness}$ (the thickness of the new meander) and $L_{meander}$ which is the length of this new meander. Currently values for those parameters are as follows: $L_{separation} = 1mm$, $L_{thickness} = 0.75mm$ and $L_{meander} = 7.5mm$. The S_{11} performance of this new design is much better than the original, as it is depicted in Figure 3.9.

On the other hand, in Figure 3.10 there are shown the impedances of the original and the new design. It is seen that with the new design, the desired reactance (200Ω) is achieved, but the resistance is too high. Therefore, following modifications will be focused on reducing the resistance while keeping the reactance on desirable inductive values. In this sense, modifications will be held on the thickness, length and separation of the meanders.

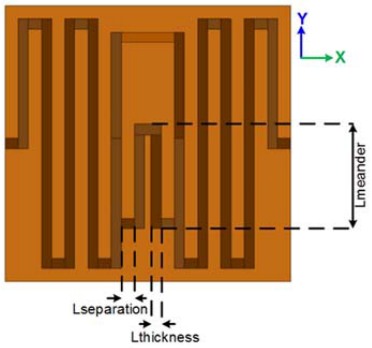

Figure 3.8: Representation of the new design with an additional meander on the central zone

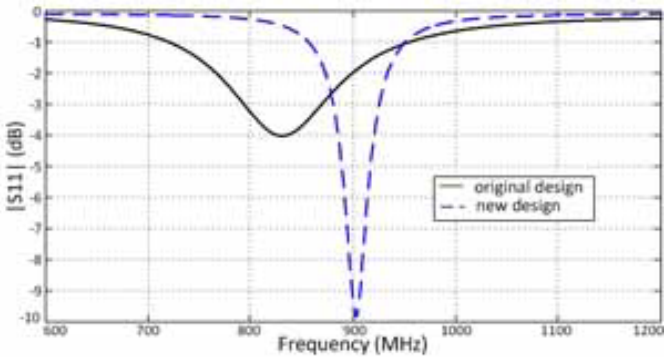

Figure 3.9: S_{11} performance of the new and the original antenna designs

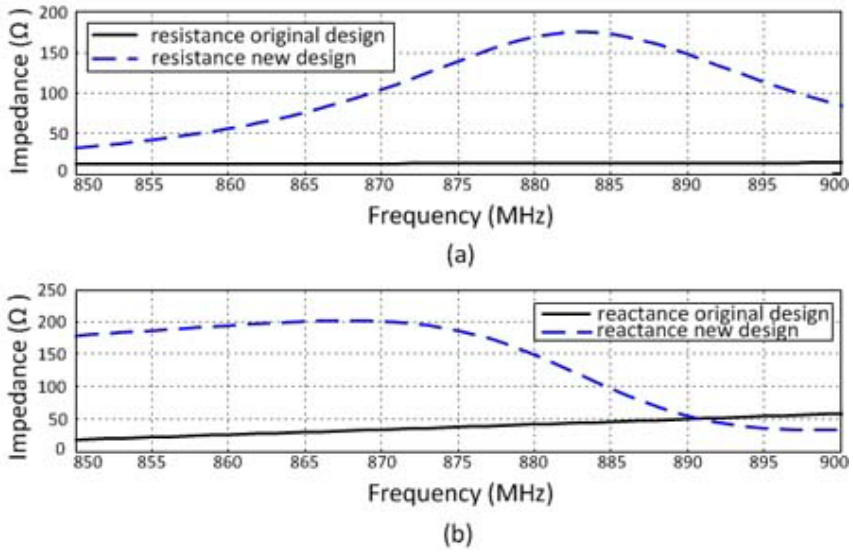

Figure 3.10: Impedances of the new and the original antenna designs. (a) resistance and (b) reactance

3.2.3.1. Meander length

As have been already explained, introducing an additional meander on the central part of the antenna results in a better performance. However, introducing this additional meander

has shifted the frequency to higher values. This is why a modification on the meander length was carried out in order to bring back the resonant frequency to the UHF band. Parameter $L_{meander}$ was increased from 8mm to 14mm. Results are depicted in Figure 3.11. It is seen that as the meander length increases, the S_{11} performance improves; so the parameter was set to a value of 14mm. The length has not been increased more than 14mm because of physical space; in fact, there is no more space for this central meander to be longer. As the result with a length of 14mm is acceptable, it was not considered to make it longer as this action would have led in an increase on the overall tag size.

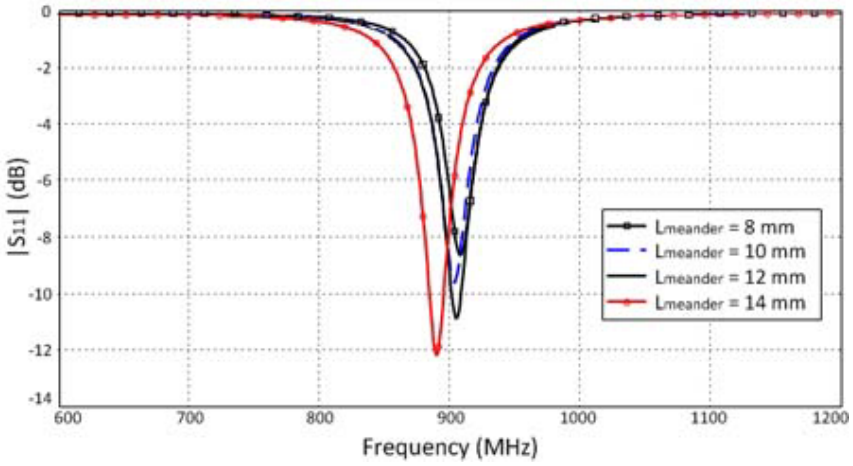

Figure 3.11: S_{11} performance of the changes in the meander length

3.2.3.2. Meander thickness

Although in previous subsections the S_{11} performance has been improved, it is still unresolved the problem of achieving a good impedance matching with the one of the RFID chip. The reader could remember that altought the imaginary part of the impedance (reactance) has a desirable inductive behaviour, the resistance it is still too high. In order to reduce the resistance value and, therefore, improve the overall impedance matching, the thickness of the meander was modified. Parameter $L_{thickness}$ was set from 0.75mm to 1.25mm. Figure 3.12 presents the results obtained with this modification. It is observed that an increase in the meander thickness is translated in a reduction on its both resistance and reactance impedance. Therefore, a trade-off between low resistance value and a reactance about 200Ω had to be achieved. In this sense, it was decided to set the meander thickness at 1.15mm.

3.2.3.3. Meander separation

Finally, it was taken into account the separation between this additional meander and its neighbour meanders. This distance is represented in Figure 3.8 as $L_{separation}$. This said parameter was set in simulations with values of 0.5mm, 0.65mm and 0.7mm. Results of such simulations are depicted in Figure 3.13. It is observed that results do not differ significantly altough it is seen that the result which presents the best behavior in both resistance and reactance, is when $L_{separation}$ has a value of 0.65mm.

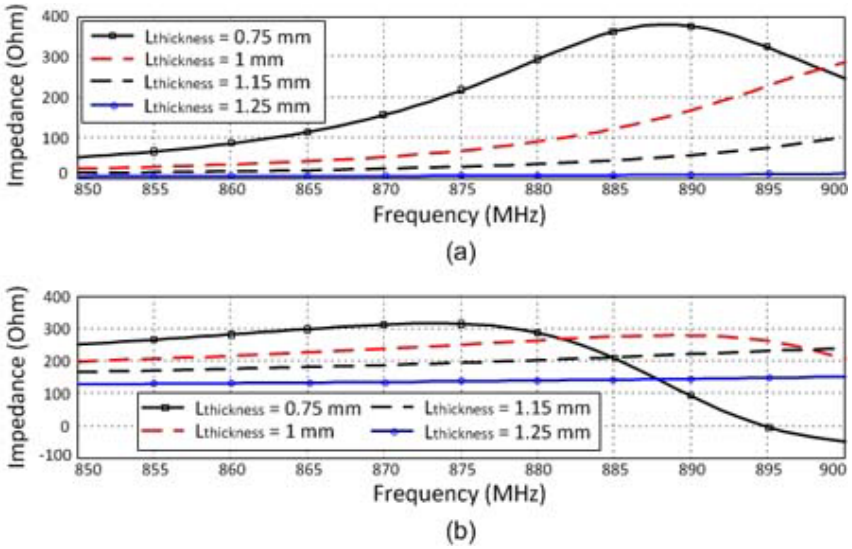

Figure 3.12: Impedances for different meander thickness. (a) resistance and (b) reactance

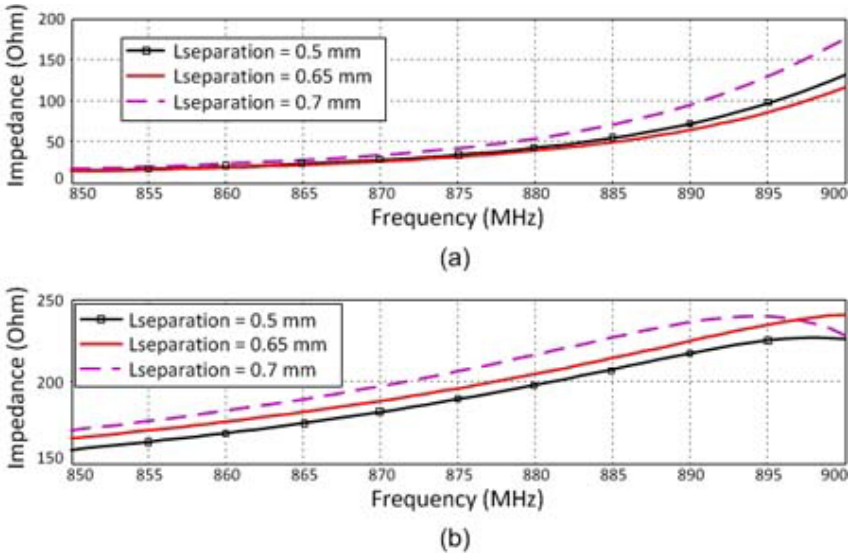

Figure 3.13: Impedances for different meander separation. (a) resistance and (b) reactance

3.3. Final design

In this section is going to be described the final design of the RFID tag. In order to realize this final design there have been considered all the previous results commented on previous sections and subsections of this chapter. From those results, it has been concluded that the tag performance improves significantly when an additional meander on the top face is introduced. Moreover, it has been checked through several simulations that the tag behavior can be improved by means of modifying the meander length, thickness and separation from the other meanders. The design presented in this section is the result of the analysis of the previous simulations, trying to get the best combination of measurements of the parameters mentioned above. Thus, in Table 3.15 are described the dimensions of the tag which corresponds to the parameters represented in Figure 3.14. The final design presents an overall size of 21.5x20.75x16.25mm, providing a compact size.

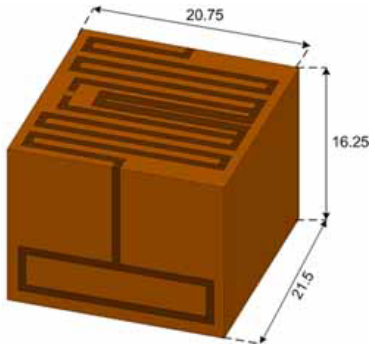

Figure 3.14: 3D layout of the final design (cube antenna)

$L_{separation}$	$L_{thickness}$	$L_{meander}$
0.65	1.15	14

Figure 3.15: Dimensions of the cube antenna (unit: mm). See Figure 3.8 to see parameters

Final design simulation results of S_{11} and impedance are shown in Figures 3.16 and 3.17 respectively. The tag presents a good S_{11} matching while its input impedance is in agreement with what was intended to achieve, being of 23.6+j185Ω. With these results, the simulation phase can be considered complete and, therefore, fabrication process of the RFID tag is the next step.

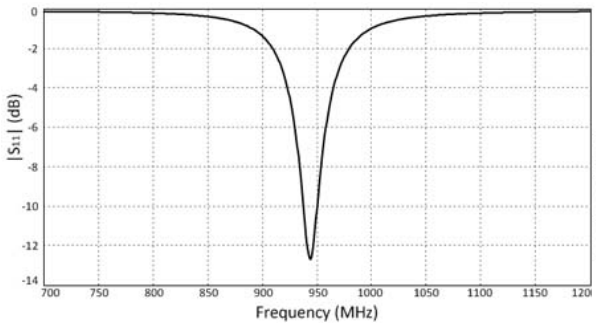

Figure 3.16: S_{11} performance of the final design (cube antenna)

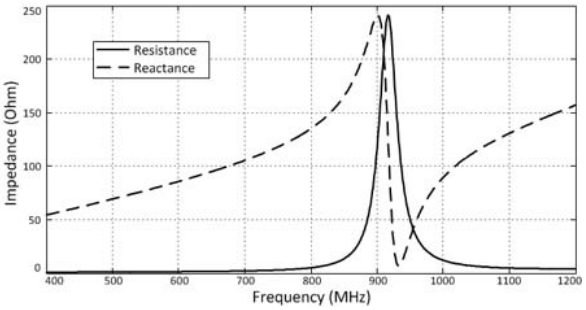

Figure 3.17: Cube antenna impedance

3.3.1. Tag fabrication

In this section is described the fabrication process of the RFID tag. Manufacturing the RFID tag was carried out following the same process described previously in this thesis when other antennas have been fabricated. This is, the use of adhesive copper tape being milled and placed on cork substrate. The Alien $Higgs^{®}$ 3 chip was soldered using standard soldering procedure. The fabricated tag is shown in Figure 3.18.

Figure 3.18: Photograph of the cube antenna

A second step on the fabrication process was to embed the tag inside a cork stopper in a similar way as it has been done previously with the cube antenna (see Section 2.3.7.). In this case, as the tag does not have a SMA connector but instead has the RFID chip, the tag can be completely inserted and the cork stopper can be covered, providing a compact result (see Figure 3.19).

Figure 3.19: RFID tag inside a cork stopper. (left) - partial embedded and (right) - completely covered

CHAPTER 4. RFID TAG WITH ADDED TEMPERATURE SENSING CAPABILITIES

The most common application of RFID is identification for inventory, but use as a communication back end for sensing is becoming more common. RFID systems have a lot of attractive advantages and great potential as low-power wireless platform for sensing applications. First of all, the cost of RFID tags is typically very low. Additionaly, passive RFID tags not only have a longer life time than other active sensors devices but also have lower consumption. Benefits for wireless RFID-enabled sensing arise in industrial applications where manual or wired measurements is impractical or unsafe in real time.

Passive RFID tag antenna sensors operate based on the principle that the back-scattered signal from the sensor varies depending on a desired sensing parameter. At this point one should especially note the principle of backscatter modulation: when an antenna is illuminated by an EM wave, electric currents are generated on its conducting parts. These currents create an EM wave that is reradiated and can be seen as a signal reflected by the antenna. Due to the fact that the currents on the antenna are dependent on the load impedance of the antenna, then changing this impedance will modify the currents on the antenna conducting parts and hence the characteristics of the wave reflected by the antenna.

In the last years, there have been many the studies related with the integration of Wireless Sensor Networks (WSN) and RFID technology for managing traceability along food supply chains [39] [40]. Indeed, one of the greatest advantages of using RFID systems in the food supply chain is the automation of processes. Hence, the wine industry is highly susceptible to improvements that can bring the integration of these technologies. In order to monitor wine fermentation, there are many factors which can be sensed such as humidity, yeast or sugar; however, temperature is one of the most important factors as if it falls outside of desirable parameters this will usually result in low-quality wine. Therefore, achieving low cost, passive wireless temperature sensors in wine industry is of special interest.

Therefore, this chapter will explain the steps followed to implement an RFID-enabled wireless temperature sensor based on the RFID tag described in the previous chapter. First of all, the sensor itself will be chosen and described. The chapter continues describing the principle of operation of such RFID-enabled sensor and showing the simulation results carried out on the design process. Finally, two tags with different fixed SMD resistances are fabricated; these tags are intended to prove the variation on the tag behavior as a dependece of a change in the sensing parameter.

4.1. Sensor description

In order to provide temperature sensing capabilities to the RFID tag, an RTD (Resistance Temperature Detector) is used. This kind of temperature sensor can be used to measure temperature by mapping the resistance of the RTD to a certain temperature value. Thus, as the temperature varies, the RTD resistance also varies and a correlation between both

can be stablished. The specifications of the selected RTD and in particularly, the table where are specified the correlation between both temperature and resistance can be found in Appendix F. The chosen sensor is the Vishay PTS SMD Flat Chip temperature sensor, which is made of platinum, as it is a SMD (Surface Mount Device) has compact dimensions which is of vital importance as there is little physical space in the RFID tag.

Hence, placing this device in the RFID tag will produce a change on the sensor resistance as the temperature varies; at the same time, this change on resistance will produce a change on the tag antenna impedance matching. Therefore, this impedance mismatch is translated into the read range performance.

From the sensor specifications (Appendix F), it is given the temperature resistance relationship which is given following the equation 4.1. Note that this equation is only applied for the temperature range of 0 °C to +155 °C. In fact, as has been explained previously in Section 1.3. of Chapter 1, the temperature range of interest in wine industry goes from 7 °C to 25 °C.

$$R_T = R_o \times (1 + A \times T + B \times T^2) \tag{4.1}$$

where R_T is the resistance as a function of temperature, R_o is the nominal resistance value at 0 °C, T is the temperature in °C, $A = 3.9083 \times 10^{-3}\,°C^{-1}$ and $B = -5.775 \times 10^{-7}\,°C^{-2}$,which are the coefficients.

Applying equation 4.1 for both temperature values, it is obtained a resitance value of 102.7Ω for the lower temperature limit and 109.7Ω for the upper temperature; thus providing to the sensor only a 7Ω change in the desired range. This little resistance variation also produces a little impedance matching variation on the RFID tag antenna.

In order to solve this problem, a circuit is proposed inspired by the work proposed in the paper “Resistance Compression Networks for Radio-Frequency Power Conversion” [41]. In this work, the authors propose a matching network where for a high resistance variation in its input, is translated into a small resistance variation of the load impedance of this network. As the problem described previously results in a little output variation for a relative large input variation, what is proposed in this paper is the opposite of the aimed solution. Therefore, it can be set a starting point where this matching network could be used to operate in the opposite way. This study will be described in the following section.

4.2. Design and implementation of the expansion network

The proposed matching network in [41] is shown in Figure 4.1. It is seen that it is a four-element network, composed by two capacitors and two inductors. The authors in [41] show that for a large variation in R, there is a variation in input resistance R_{in} smaller than the variation in load resistance R. As discussed previously, what is aimed in this thesis is the opposite behavior; that is, for a small variation in R obtain a larger variation in the ouput impedance of the network. Therefore, it was considered a similar network (Figure 4.2) consisting of reactive components and optimized their values in order to obtain a large input impedance variation. In the figure is also considered the RFID chip, which is going to be connected to this network. In this case, for a little variation of R a larger variation

on the input impedance of the network is obtained; thus changing the antenna impedance matching. In Table 4.1 there are described the component values of the network proposed in [41].

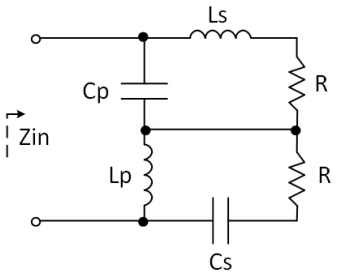

Figure 4.1: Compression network

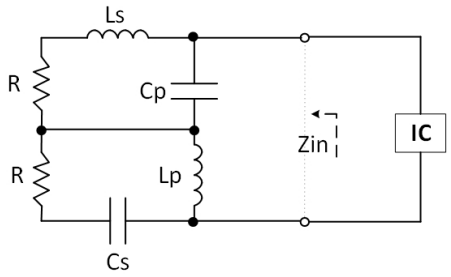

Figure 4.2: Expansion network

Component Name	Nominal Value	Manufacturer and Part Style	Part Number
C_p	15 pF	CDE Chip	MC08EA150J
C_s	11 pF	CDE Chip	MC08CA080C
L_p	169 nH	Coilcraft	132-12SM-12
L_s	246 nH	Coilcraft	132-15SM-15

Table 4.1: Components used in the compression network proposed in [41]

In order to run simulations on the circuit depicted in Figure 4.2, it was implemented into the Ansys HFSS layout. It was considered the layout of the RFID tag described in Chapter 3 and it was modified introducing the circuit in the central part of the tag's top face, where there was some free space. The modified layout with the expansion network is shown in Figure 4.3. It is also shown a detail of the network, where are specified the components and where they are placed. Components are denoted by lower s or p whether they are placed in series or parallel. Therefore, L_s denotes for the inductor placed in series, L_p for the inductor in parallel and C_s and C_p for the capacitors in series and in parallel, respectively. Resistance values R_1 and R_2 are equal; two resistance values were considered, 100Ω and 150Ω.

Simulations with Ansys HFSS were performed on the layout depicted in Figure 4.3. Using optimization features of the software, there were obtained the component values that led to a higher impedance variation. These values are depicted in Table 4.2, where there are also depicted the commercial components selected to be placed on the fabrication process. Specifications of such components can be found in Appendix E.

Simulation results obtained in Ansys HFSS for resistance values of 100Ω and 150Ω were processed to obtain the simulated read range. Both results are compared with the RFID tag one, this is shown in Figure 4.4. It can be clearly seen a modification of the read range for both resistance values. These results leads to a frequency shifting to higher values, being the peak range placed inside the American UHF RFID band (902 - 928 MHz). In any case, this result evidence a change on the tag read range performance when the resistance value is changed. Hence, the following step would be the fabrication and measurement of both tags.

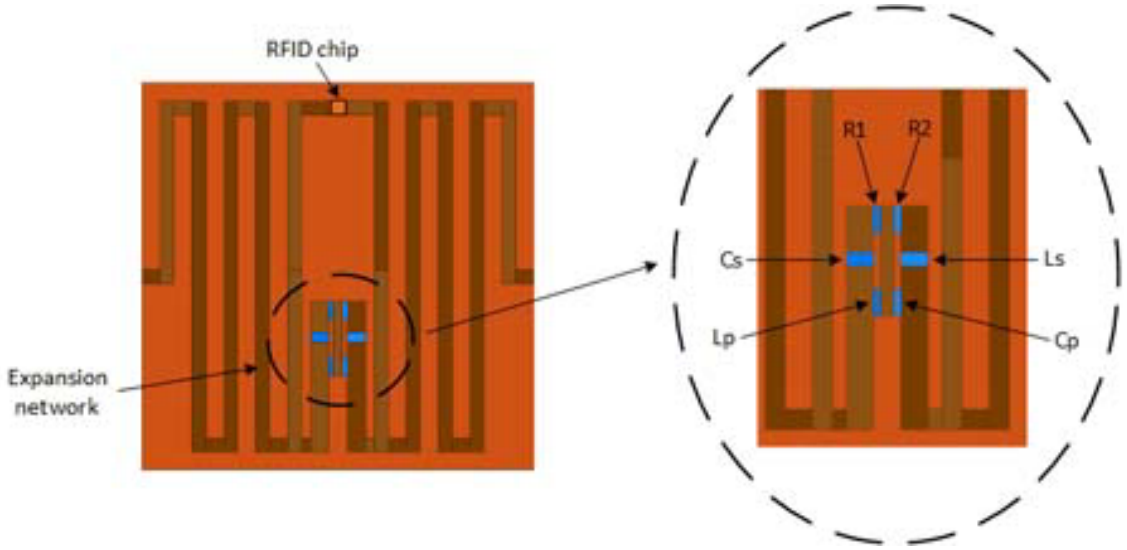

Figure 4.3: Ansys HFSS layout of the RFID tag with the lumped network

Component Name	Nominal Value	Manufacturer and Part Style	Part Number
C_p	23.2 pF		
	1.2 pF	Murata	0402/COG/1.2pF
	22 pF	Murata	0402/COG/22pF
C_s	11.2 pF		
	1.2 pF	Murata	0402/COG/1.2pF
	10 pF	Murata	0402/COG/10pF
L_p	1 nH	Coilcraft	0402CS-1N0X$_L$
L_s	8.3 nH	Coilcraft	0402CS-8N3X$_L$

Table 4.2: Components used in the expansion network

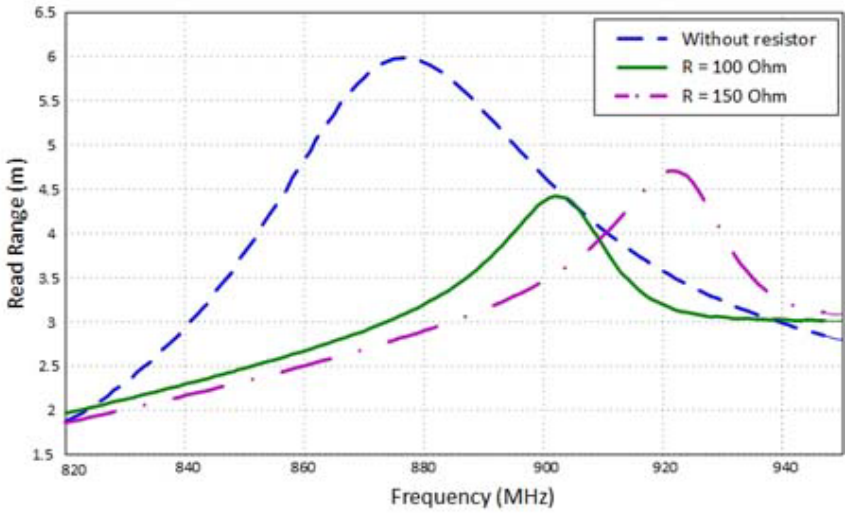

Figure 4.4: Simulation of the tag read range; without resistance, with a 100Ω resistance and with a 150Ω resistance

4.3. Fabrication of the tags

Two RFID tags with different resistance values were fabricated. One tag with a resistance value of 100Ω and the other tag with a 150Ω resistance. Fabrication process for those

tags were slightly different than the one used for previous designs considered in this thesis. Actually, the difference on the fabrication process came up with the implementation of the lumped network. The RFID-tag-antenna was built following the same process described in previous chapters, thus involving milling addhesive copper tape and placing it on cork substrate applying pressure. The RFID chip was soldered using regular soldering technique.

On the other hand, conductive epoxy was applied in order to perform solderless electronic connections between the lumped network components. The epoxy mixture was applied with the help of a needle on the tag surface and then, the components were placed. In order to assist in the drying process, the tags were placed inside an oven during 15 minutes at 80 celsius degrees. In Figure 4.5 it is shown an image taken from a microscope where it can be appreciated the components of the network with the applied epoxy. Finally, both fabricated tags are shown in Figure 4.6. Measurement results of these tags can be found in Chapter 5.

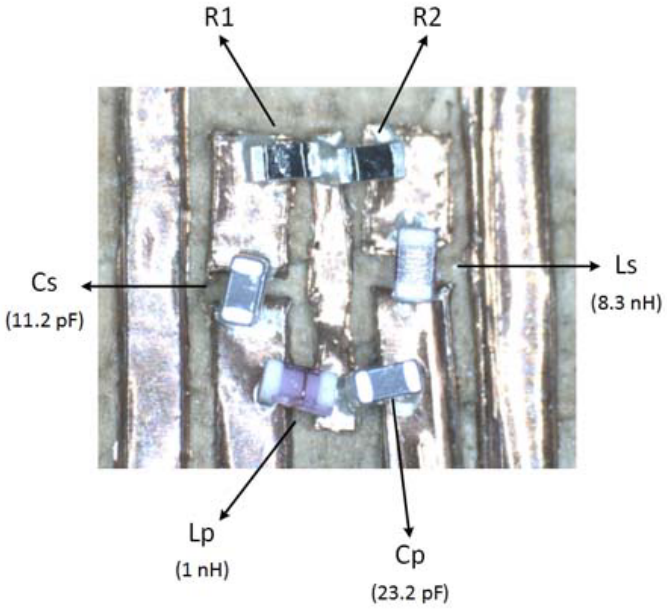

Figure 4.5: Image of the lumped network taken from a microscope

Figure 4.6: Two RFID tags with the implemented lumped network. The tag on the left has a resistance value of 100Ω and the tag on the right, a 150Ω resistance

CHAPTER 5. MEASUREMENTS

In previous chapters of this thesis, the simulation and fabrication processes of different antennas which use cork as their substrate have been discussed. In addition, the design and fabricaton processes of a RFID tag which is aimed to be used in cork stoppers of bottles have been detailed. Finally, modifications on the considered RFID tag were applied in order to achieve a RFID-enabled wireless sensor for temperature monitoring.

This chapter will discuss the measurements performed on the fabricated designs. On one hand, measurements in an anechoic chamber were realized in order to obtain consistent and repeatable results. On the other hand, measurements in the laboratory have been done, which is not a controlled environment thus involving multipath reflections. This allows to extract realistic results involving a non-friendly propagation environment.

Different fabricated designs will be discussed separately, discussing for each case the measurements performed on the design. Therefore, there is a section involving measurements performed on the straight dipole antenna, the 3D meandered dipole antenna, the RFID tag and, finally, a section for the measurements on the RFID tags with sensing capabilities.

5.1. Straight dipole antenna

The straight dipole antenna described in Section 2.1. of Chapter 2 was measured in both controlled and multipath environments. First of all, measurements of the antenna radiation pattern were performed in an anechoic chamber. The considered element (in this case, the $\lambda/2$ dipole) was placed inside the anechoic chamber. Due to limitations of the chamber, measurements were performed only on 180 degrees.

Figure 5.4 shows the radiation pattern measurements in the anechoic chamber. The obtained radiation pattern has the regular shape for a dipole. A gain of 0.42dBi is achieved in comparison with the 1.87dBi obtained in simulations (Figure 5.3). This difference could come from the fact that in simulation process has been considered a perfect electric conductor; furthermore, additional losses could come from not mounting properly the connector in the fabrication process or the copper glue which is not included in simulations. Finally, another factor that could be affecting such difference between simulation and measurement results, is the cable used to connect the antenna in the measurement; although it was partially covered with absorber material, it was not possible to cover it completely.

Measurements on the input S-parameter of the antenna were made using the Agilent Technologies E8361A PNA network analyzer [18]. As can be seen in Figure 5.6, a good result was obtained as it offered approximately -23dB adaptation at the resonant frequency (864MHz) and around -20dB in the working frequency range (865-868MHz).

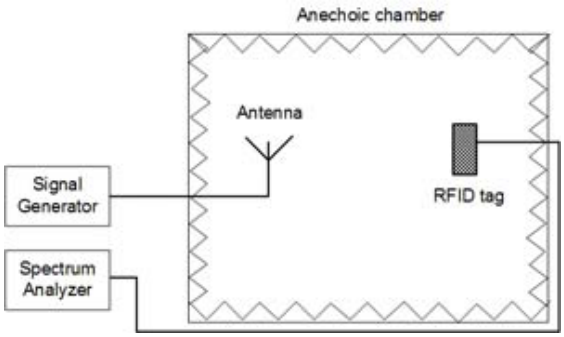

Figure 5.1: Experimental setup for measuring the radiation pattern of a RFID tag

Figure 5.2: Photograph of the measurement setup in the anechoic chamber

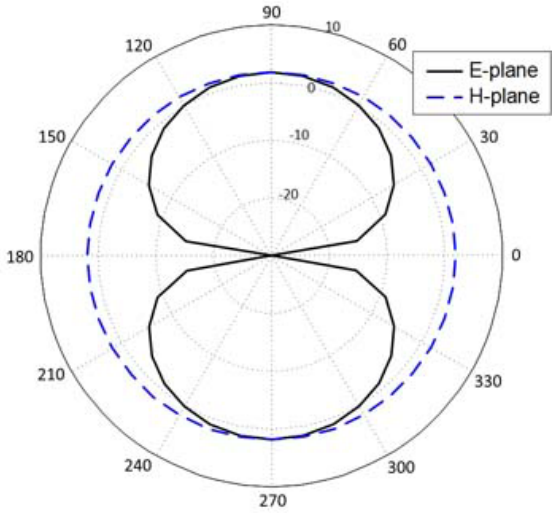

Figure 5.3: Simulated radiation pattern of the straight half-wavelength dipole antenna

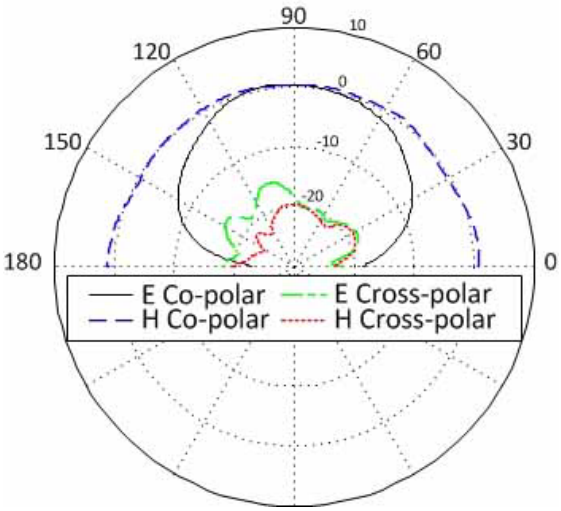

Figure 5.4: Measured radiation pattern of the straight half-wavelength dipole antenna

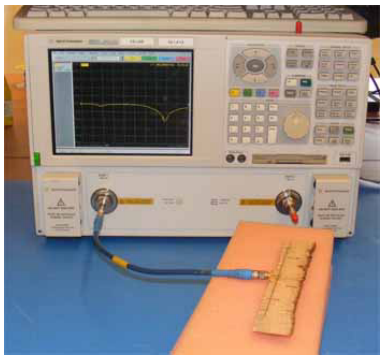

Figure 5.5: Measurement of the antenna with a VNA

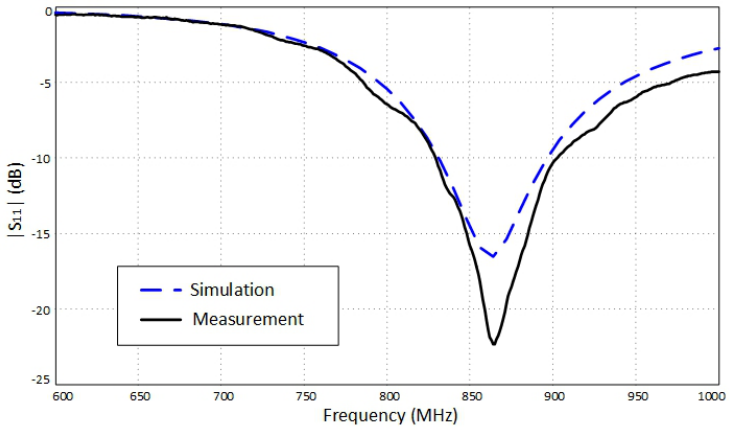

Figure 5.6: S_{11} simulation vs. measurement results

5.2. 3D meandered dipole antenna

As done with the straight dipole, the radiation pattern of the 3D meandered antenna was measured in an anechoic chamber. The measured radiation pattern is compared with the

simulated one in Figure 5.7. As can be seen, simulation results provide a much higher gain than what was obtained in measurement. Reasons for this difference are be the same as explained in section 5.1. for the case of the straight dipole. Moreover, a slight misalignment on the measured H and E planes is observed; this is due a bad subjection of the tag when it was measured, so as it moved slightly during the measures, this has been translated in the pattern.

Moreover, the input S-parameters of the antenna were measured with the VNA [18] in the lab. The measured S_{11} is compared with the one obtained in simulation (see Figure 5.8). It is seen an agreement between both theoretical and measured results; altought in the measurements the resonance frequency is shifted slightly to higher a value.

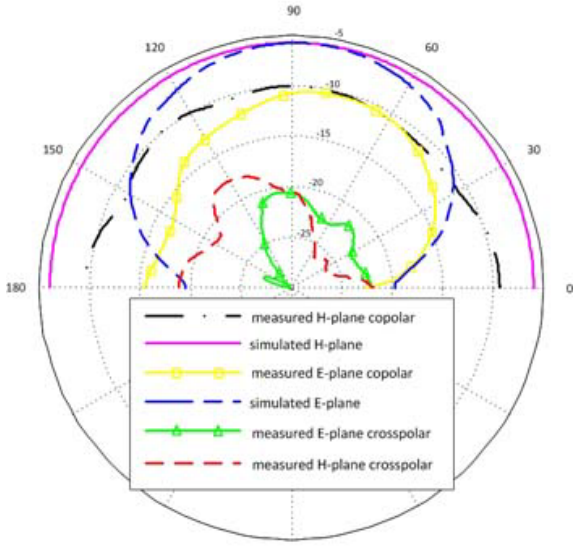

Figure 5.7: Simulated vs. measured radiation pattern of the 3D meandered dipole antenna

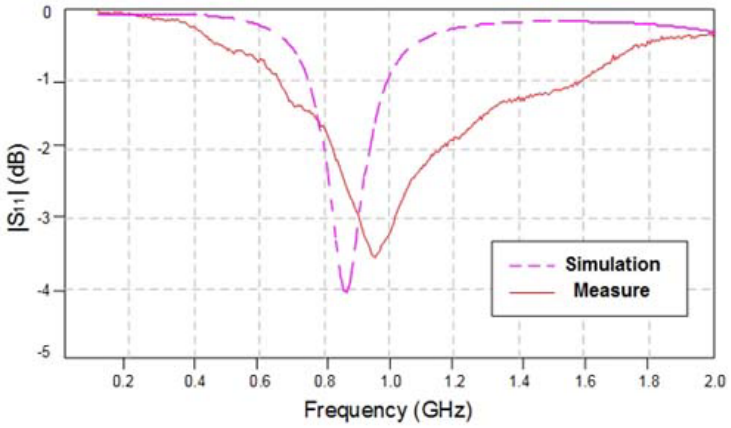

Figure 5.8: Simulation vs. measurement results of the 3D meandered dipole antenna

5.2.1. 3D meandered dipole antenna inside cork stopper

The 3D meandered dipole antenna was introduced inside a cork stopper (see Figure 5.9) of 5cm diameter, as it has been explained previosly in this thesis in section 2.3.7. of chapter 2. Input S-parameters of the antenna inside cork were performed with the VNA. It is apreciated in the obtained results (Figure 5.10) that when the antenna is introduced in the cork stopper, the resonance frequency shifts to lower values and consequently presents a better matching at the frequencies of the European UHF RFID band. This shift into a lower frequency is attributed due to the fact that as the antenna is surrounded by cork medium, which has a dielectric constant higher than the air one, the antenna looks electrically larger and thus, its resonant frequency is lower.

Figure 5.9: Photograph of the antenna inside a cork stopper

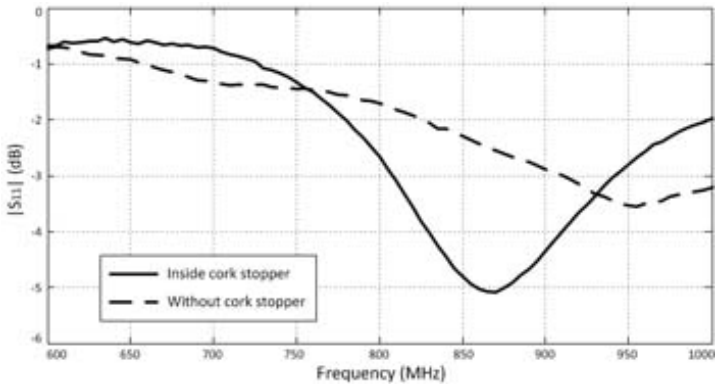

Figure 5.10: S_{11} parameters of the antenna inside cork vs. without cork stopper

5.3. RFID tag

This section is devoted to describe the measurements performed on the RFID tag described in section 3.3. of chapter 3. One of the main tag performance characteristics is the read range, which is defined as the maximum distance at which the RFID reader can detect the backscattered signal from the tag and thus, the tag can be read. The read range r can be calculated using Friis free-space formula, as have been considered in other works [42] [43] [44].

$$r = \frac{\lambda}{4\pi}\sqrt{\frac{P_t G_t G_r p \tau}{P_{th}}} \tag{5.1}$$

where λ is the wavelength, P_t is the power transmitted by the reader, G_t is the gain of the transmitting antenna, G_r is the gain of the receiving tag antenna, p is polarization mismatch between the tag and the reader antennas, P_{th} is the minimum power required to provide enough power to the RFID chip to respond, and τ is the power transmission coefficient calculated as follows

$$\tau = \frac{4R_c R_a}{|Z_c + Z_a|^2}, 0 \leq \tau \leq 1 \tag{5.2}$$

where $Z_c = R_c + jX_c$ is chip impedance and $Z_a = R_a + jX_a$ is antenna impedance.

5.3.1. Measurement setup

Two methods were used to measure the tag performance. The first method used fixed transmitted power and variable distance to the tag. In this method, the reader transmits with constant power while the tag is moved away until no reading can be performed. The second method consists of using variable power and fixed distance to the tag. The transmitted power is varied to find the minimum value at which the tag becomes detectable [44]. Both methods used the same laboratory setup involving, in this case, a transmitting/receiving antenna, a computer, a signal generator, an oscilloscope, a directional coupler and the considered RFID tag; an shcematic of the setup can be found in Figure 5.11.

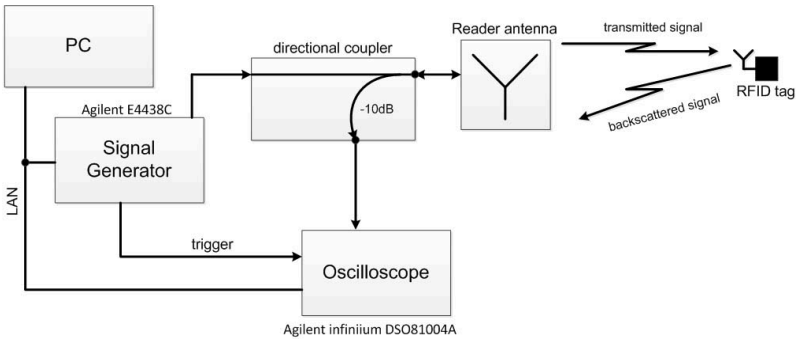

Figure 5.11: Block diagram of the measurement setup

It is important to emphasize that a reader antenna was designed and built for the measurements. The main reason to do that was because there was no circularly polarized reader antenna capable to work on the RFID UHF band (860-920 MHz). Therefore, it was decided to built a patch antenna because it is a low cost, and low profile, planar antenna which is able to provide a circularly polarized wave covering the desired frequency band. In order to provide circularly polarization, two feeds producing orthogonal linearly polarized waves are used, with one feed delayed by 90 $^\circ$ with respect to the other. This feed condition is achieved using a 90 $^\circ$ hybrid coupler.

The author of this thesis only carried out the fabrication process while the antenna design was developed by the thesis director. The reader can find the information about the fabrication process and the antenna parameters in Appendix G.

Referring to the measurement setup depicted in Figure 5.11, the computer was connected through LAN connection with the signal generator and the oscilloscope and was used to send the inventory sequence to the signal generator. At the same time, the signal generator is connected to the transmitting antenna through a directional coupler. Specifically, the signal generator is connected to the through port of the directional coupler while the transmitting antenna is connected to the incident port. The coupled port is connected to the oscilloscope which is thus showing the received signal from the tag. The signal generated through the Matlab code and transmitted by the signal generator is also sent to the oscilloscope to be used as a trigger signal. Thus, the backscattered signal from the tag can be seen in the oscilloscope and this way it can be determined whether the tag is responding or not.

5.3.1.1. Wake-up sequence

Waking up the transponder chip was done using an inventory sequence according to the EPCglobal Gen2 Standard. The inventory sequence was generated in Matlab (see Appendix D) and sent to the vector signal generator [32]. The inventory sequence consists on a query command, which is used to initiate an inventory round where the reader and the tag communicate each other cyclically. Initially, the query command sent to the chip, requests an answer from it. The tag replies to this command by sending a 16 bit random sequence. The reader responds the tag by means of sending this 16 bit random sequence back. The analysis of the Gen2 communication protocol is beyond the scope of this thesis, but the reader can found complete information about it consulting the published EPCglobal Gen2 Standard [34].

In Figure 5.12 a capture from the oscilloscope is shown where it can be observed the inventory sequence. In addition to the sequence, the magnitude FFT of the signal is computed, which helps to verify the sequence characteristics. As it can be apreciated, the query command sent by the reader consists on a 22 bit sequence, as it is specified in the EPCglobal Gen2 Standard.

On the other hand, captures of a tag response and non-response are showed in Figure 5.13. The reader can see that when there is no tag response, the FFT only shows the main lobe due to the carrier; however, when there is a tag response, it can be clearly observed through the FFT. Although in the time domain signal capture (Figure 5.13) cannot be appreciated well, the tag response can be apreciated in the received power signal paying attention to the small peaks in the upper and lower borders of the signal.

Figure 5.12: Inventory command

5.3.1.2. Read range results

Formulas 5.1 and 5.2 were processed with Matlab (see code in Appendix C) to obtain theoretical results in the range from 820 to 920 MHz. Values for the transmitted reader

Figure 5.13: (a) tag no response - (b) tag response

power (P_t) was 24dBm and 5dBi for the reader gain G_t (see antenna specifications in Appendix G). The simulated gain G_r was obtained from Ansys HFSS. Similarly, tau was calculated using simulated impedance values for the tag antenna and the chip. The chip was modeled as a parallel RC circuit with $R = 1500\Omega$ and $C = 0.9pF$ (see Table 3.1). For the threshold power, P_{th}, it was considered the value of -18dBm.

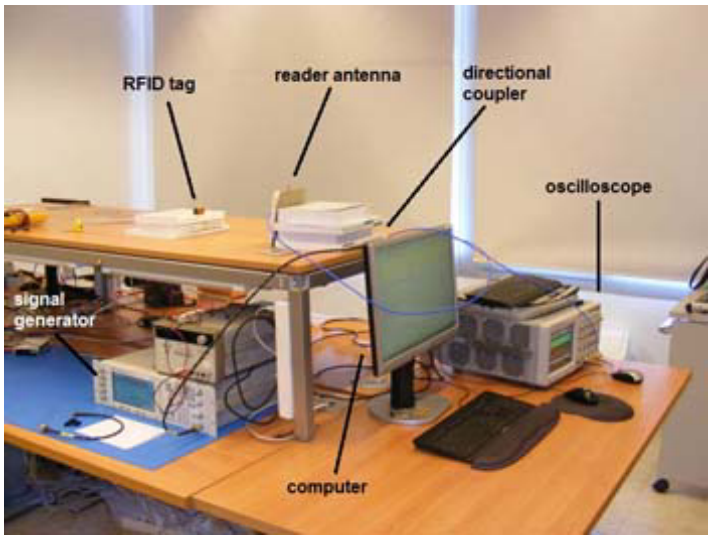

Figure 5.14: Image of the measurement setup

The theoretical calculation was compared with measured data. In Figure 5.15 are compared both theoretical data obtained through Matlab processing and measured data from lab test experiment. It is seen that theoretical and measured data differ from each other. This difference can com from the fact that values for tag gain and antenna impedances are considered from simulation results which can differ from actual values. It has to be considered also that measured data was taken in a real environment thus being affected by various types of interferences, such as multipath reflections or interferences from external EMI sources, while theoretical result considers free-space propagation environment. Moreover, the tag is not properly matched to the chip and therefore it is translated in a low tau value. In any case, it is appreciated that both results present the peak range around 875 MHz and a measured read range of 90 cm is achieved in the UHF band (considering

a transmitted power, P_t of 24dBm). In fact, increasing the transmitted power up to 30dBm, the range is expected to be doubled from 5.1.

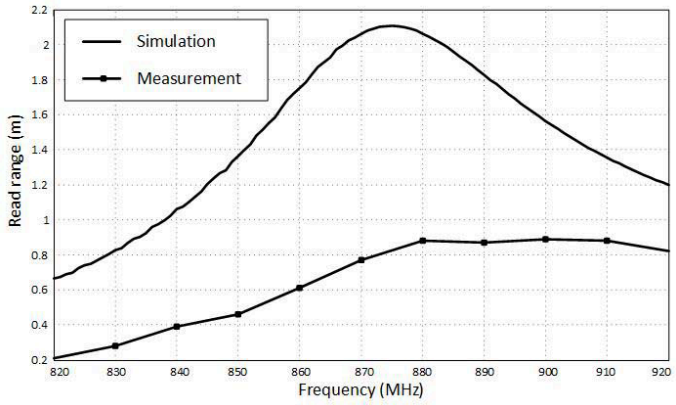

Figure 5.15: Read range simulation vs measurement

The second method used, which involved fixed distance to the tag (38cm) and variable transmitted power, was used to estimate the tag power sensitivity. Tag sensitivity is defined in [44] as the minimum signal strength at the tag location needed to power up (read) the tag. This tag performance characteristic is a function of the chip threshold power sensitivity, tag antenna gain, and match between tag antenna and chip. Tag power sensitivity can be expressed as:

$$P_{tag} = Gp\tau P_{th} \tag{5.3}$$

where p is the polarization efficiency, τ is the impedance matching coefficient between the tag antenna and the chip, and P_{th} is the chip power threshold sensitivity. Equation 5.3 shows how much minimum incident power at the tag location is needed to make sure that the sufficient amount of it gets absorbed in the RFID chip and activates it [44].

In this second measurement method, the transmitted power was varied to find the minimum transmitter power P_{min} to turn on the tag, similarly as it is done in [45]. In fact, tag power sensitivity and read range for any given EIRP can be calculated from the measured minimum power P_{min} using the following equations, which have been extracted from [45] and [44].

$$P_{tag} = P_{min} G_t \left(\frac{\lambda}{4\pi d} \right)^2 \tag{5.4}$$

$$r_{tag} = d \sqrt{\frac{EIRP}{P_{min} G_t}} \tag{5.5}$$

where P_{min} is the minimum transmitted power to turn on the tag, G_t is the tag gain, λ is the wavelength at 865MHz, d is the distance between the reader and the tag (38 cm), and the EIRP (Equivalent Isotropically Radiated Power) refers to the radiated power in a single direction. It has been considered an EIRP of 2W because of international regulations on the European UHF RFID band [10].

Equations 5.4 and 5.5 consider free space propagation and thus would require measurements in an anechoic chamber; this was not the case, and the measurements were performed in the lab, implying multipath environment. However, with the measured minimum transmitted power P_{min} to turn on the tag, the tag power sensitivity and read range were

calculated from equations 5.4 and 5.5. These results are depicted in Figure 5.16, one can see that the best tag sensitivity values correspond to the best tag range and vice versa.

Additionaly, measurements with a commercial Impinj Revolution R420 reader were performed in a real scenario involving multipath effects. Such measurements and the corresponding results can be found in Appendix B.

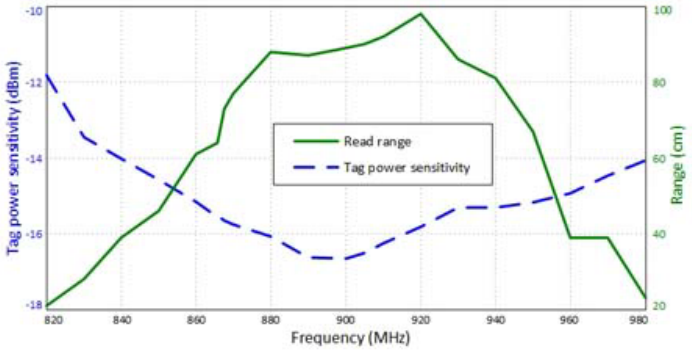

Figure 5.16: Tag power sensitivity (dBm) and range (cm) vs. frequency (MHz). Other parameters: 2W EIRP

5.3.2. RFID tag inside cork stopper

In this case, the RFID tag was introduced inside a cork stopper (see Figure 3.19 from chapter 3) and the same measurement methods described above were performed on the tag. First, read range measurements results with fixed transmitted power and variable distance to the tag are obtained in Figure 5.17. Where it can be seen that there is a slightly difference between both measurements. What it can be appreciated is that the peak range in the case of introducing the tag inside cork has shifted to a slightly lower frequency and it can also be appreciated that the range is slightly lower. On the other hand, tag power sensitivity and read range calculations through the measurement of the minimum transmitted power P_{min} to turn on the tag are shown in Figure 5.18. No significant difference is detected in this case compared with the one obtained in the case of the tag without being inside the cork stopper (see Figure 5.16).

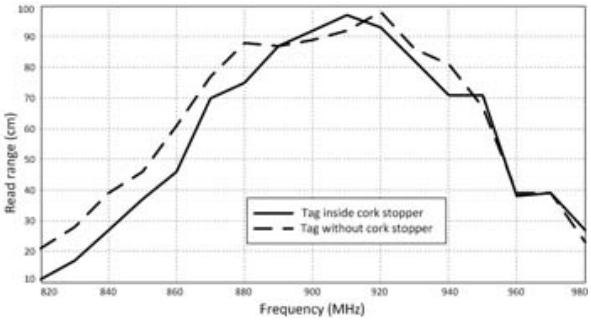

Figure 5.17: Read range for the tag inside cork stopper vs tag without cork stopper

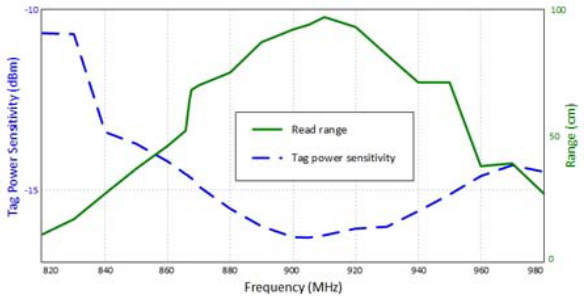

Figure 5.18: Tag power sensitivity (dBm) and range (cm) vs. frequency (MHz) for the tag being inside a cork stopper. Other parameters: 2W EIRP

5.4. RFID tags with sensing capabilities

Read range measurements were performed on the two tags with sensing capabilities. The measurement setup was the same described in Section 5.3.1. of this chapter for the case of the RFID tag. In Figure 5.19 are depicted the results corresponding to the tag with a resistance value of 100Ω. It presents results very similar to what is obtained in the case of the RFID tag. However, in this case the behavior of the tag fits better inside the European RFID UHF band. On the other hand, in Figure 5.20 are shown the results corresponding to the tag with a resistance value of 150Ω. In this case, it is seen that the behavior has shifted to a higher frequency, thus involving different values of read range and tag power sensitivity compared with the other tag. As it happened with the RFID tag, results from both tags shows that the best tag sensitivity values correspond to the best tag range and vice versa.

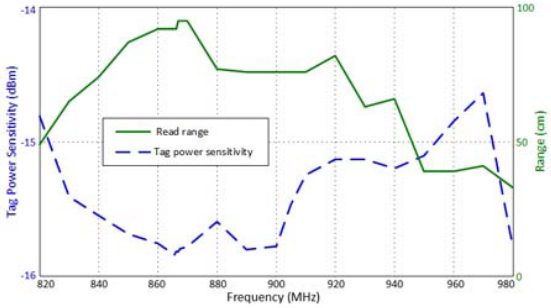

Figure 5.19: Tag power sensitivity (dBm) and range (cm) vs. frequency (MHz) for the tag with a 100Ω resistance. Other parameters: 2W EIRP

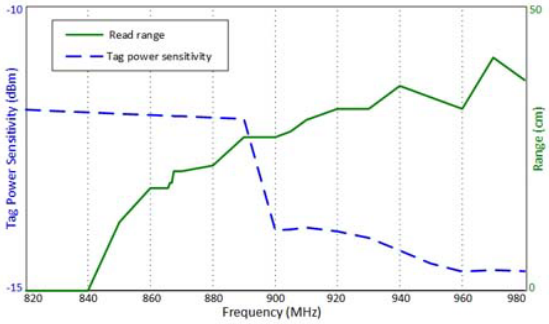

Figure 5.20: Tag power sensitivity (dBm) and range (cm) vs. frequency (MHz) for the tag with a 150Ω resistance. Other parameters: 2W EIRP

CHAPTER 6. CONCLUSIONS AND FUTURE WORK

In this Master thesis the feasibility of an RFID tag embedded in a cork stopper has been shown. A passive UHF RFID tag with a cube shape and dimensions of 21.5 x 20.75 x 16.25 mm has been designed and fabricated through a fast and cost effective fabrication process. The tag performance has been evaluated using a commercial Impinj Speedway Revolution R420 reader, achieving a 100 cm read range with 2W EIRP.

In addition, sensing capabilities have been added to the RFID tag; a lumped network with fixed resistance values has been added to test temperature sensing principle of operation. Two tags with different resistance values have been fabricated and their performance in terms of read range have been tested; measurement results have shown good agreement with simulations, presenting a change in tag performance depending on the resistance value.

6.1. Conclusions

Cork electrical properties of a piece of natural cork have been characterized using a two-line microstrip technique, determining the propagation factor of such pair of microstrip lines of different lengths and thus obtaining dielectric constant and loss tangent values. Cork ansitropy behavior has been demonstrated under various humidity conditions.

A half-wavelength dipole antenna placed on cork substrate has been fabricated. Antenna performance has been evaluated using a Vector Network Analyzer, providing good results in agreement with simulation and thus confirming correct obtained values of cork dielectric constant and loss tangent.

A 3D meandered dipole antenna placed on cork substrate has been fabricated by milling the designed pattern on low cost adhesive copper tape, allowing for a fast and cost effective fabrication.

An RFID tag has been implemented on cork substrate using the 3D meandered dipole antenna as the tag antenna. The tag has dimensions of 21.5 x 20.75 x 16.25 mm. The performance of the RFID tag has been evaluated using a commercial Impinj Speedway Revolution R420 reader, achieving a 100 cm read range with 2W EIRP.

The principle of operation of a temperature RFID-tag-antenna-based sensor has been shown. Two different tags with different resistance values have been fabricated and their performance has been tested. Their measured read range have shown a differenciated tag behavior depending on the resistance value incorporated in the tag.

The fact of developing the project from the beginning, making the design, analysis and physical realization of the antennas and tags, has helped me to acquire a better understanding of the concepts and antenna parameters.

From this Master thesis, there are being written several papers. In fact, one conference paper titled “Cork Antennas for RFID Tagging for Wine Bottles and Barrels” has been submitted to the 2014 IEEE Electronic Components and Technology Conference (ECTC), Lake Buena Vista FL, USA, May 27-30, 2014; it is currently waiting for acceptance. A journal paper titled “Low Porfile Conformal UHF Antennas and RFID Tags on Cork Substrate” is under preparation for submission to the IEEE Transactions on Antennas and Propagation in collaboration with the University of Aveiro, Portugal. This paper refers to the design and fabrication of the antennas on cork substrate described in this thesis (half-wavelength dipole and 3D meandered dipole antennas) and the RFID tag. Furthermore, another paper is planned to be written about the RFID-tag-antenna-based temperature sensor.

6.2. Future work

Improve the tag read range. As it has been discussed in the thesis, although the achieved read range is significant, it can be improved. Specifically, one of the parameters that should be improved is the impedance matching between the tag and the chip.

Implement a fabrication process involving ink-jet printing on cork substrate in order to lower the tag fabrication cost and also provide a faster process.

Place a RTD on the RFID tag instead of fixed SMD resistances in order to obtain a RFID-tag-antenna-based temperature sensor. This is not a straigthforward process as it could involve, for instance, changes on the antenna design or changes on the reactive components values. Then, the obtained tag should be measured and calibrated.

Miniaturize the RFID tag in order to make it small enough to be able to be fit inside a bottle cork stopper.

Place the cork stopper with the RFID tag inside a wine barrel. Test the behavior of the tag with an empty barrel and with a full wine barrel. In fact, it has been already studied the performance of different commercial tag models attached to wine bottles [4] [26]. It was concluded that wine seems to deteriorate the electromagnetic properties of the bottle causing a reduction of the received power, a modification of the radiation pattern and a reduction in the width of the reading arc. Therefore, the tag considered in this thesis should be measured when attached to a wine barrel and quantify such reduction on its performance.

Investigate others fields of application for the RFID tag and the RFID-tag-antenna-based sensor, not only on wine industry, but on other applications that use cork. One of this fields of application could be the aeronautics and space. Another field of application could be the construction industry. Currently, many indoor walls use cork; taking advantage of this fact, RFID tags or sensors could be placed inside walls to configure, for instance, a WSN (Wireless Sensor Network).

6.3. Environmental issues

There are no serious environmental consequences related to this work. On one hand, natural cork is used, directly extracted from the tree and, as mentioned, is a material that can be recycled. On the other hand, manufacturing process only involve milling, cut and paste. The only items to be considered to recycle after their use are the RFID chip and the passive components.

Furthermore, the fact of incorporating this technology allows to use less paper as barcodes are supressed and the product information can be stored in the tag. Finally, the sensing methodology does not harm the environment or people, while radiation levels are within current regulations.

Figure 6.1: Photograph of all the elements fabricated in this thesis

BIBLIOGRAPHY

[1] A. Rida, L. Yang, and M. Tentzeris, “RFID-Enabled Sensor Design and Applications”. Artech House, 2010. “RFID Tags for Challenging Environment”. *IEEE Microwave Magazine*. vol. 14, (no. 5). page 26–35. (July/August 2013)

[2] Sangkil Kim, Yoshihiro Kawahara, Apostolos Georgiadis, Ana Collado, and Manos M. Tentzeris “Low-Cost Inkjet-Printed Fully Passive RFID Tags Using Metamaterial-inspired Antennas for Capacitive Sensing Applications”.

[3] Z. Hu, P. H. Cole “Bottle Packaged Wine Product Detection By UHF RFID Systems”. *2010 International Conference on Electromagnetics in Advanced Applications (ICEAA)*. page 301–304. (20-24 September 2010, Sydney, NSW)

[4] Jingtian XI and Terry Tao YE “Conformal UHF RFID Tag Antenna Mountable on Winebottle Neck”. *2012 IEEE Antennas and Propagation Society International Symposium (APSURSI)*. page 1–2. (8-14 July 2012, Chicago, IL)

[5] YoungDo Kim “Design of Near Omnidirectional UHF RFID Tag with One-off Seal Function for Liquid Bottles”. *Microwave and Optical Technology Letters*. vol. 55 (no. 2), page 375–379. (February 2013)

[6] Toni Bj*ö*rninen, Member, IEEE, Atef Z. Elsherbeni, Fellow, IEEE, and Leena Ukkonen, Member, IEEE “Low-Profile Conformal UHF RFID Tag Antenna for Integration With Water Bottles”. *IEEE Antennas and Wireless Propagation Letters*. page 1147–1150. (October 2011)

[7] Smail Tedjini, Nemai Karmakar, Etienne Perret, Arnaud Vena, Randika Koswatta, and Rubayet E-Azim “Hold the Chips”. *IEEE Microwave Magazine*. vol. 14, (no. 5). page 56–65. (July/August 2013)

[8] RFID Market. (2012). [Online]. Available: http://www.idtechx.com/research/articles/rfid-market-reaches-7-67-billion-in-2012-up-17-from-2011-00004585.asp

[9] Daniel Dobkin “The RF in RFID. Passive UHF RFID in Practice”. Newnes ed., Elsevier, 2008. ISBN 978-0-7506-8209-1.

[10] European Telecommunications Standard Institute (ETSI) “Electromagnetic compatibility and Radio spectrum Matters (ERM); Radio Frequency Identification Equipment operating in the band 865 MHz to 868 MHz with power levels up to 2 W; Part 1: Technical requirements and methods of measurement”. *V1.1.1 (2004-09)*.

[11] A. Ali Babar, Atef. Z. Elsherbeni, Lauri Syd*ä*nheimo, and Leena Ukkonen “RFID Tags for Challenging Environment”. *IEEE Microwave Magazine*. vol. 14, (no. 5). page 26–35. (July/August 2013)

[12] Sangkil Kim, Chiara Mariotti, Federico Alimenti, Paolo Mezzanotte, Apostolos Georgiadis, Ana Collado, Luca Roselli, and Manos M. Tentzeris. “No Battery Required”. *IEEE Microwave Magazine*. vol. 14, (no. 5). page 66–77. (July/August 2013)

[13] Rahul Bhattacharyya, Student Member IEEE, Christian Flowrkemeier, Member IEEE, and Sanjay Sarma, Member IEEE “Low-Cost, Ubiquitous RFID-Tag-Antenna-Based Sensing”. *Procedings of the IEEE* . vol. 98, (no. 9), page 1593–1600. (September 2010)

[14] G. Marrocco, L. Mattioni, and C. Calabrese, “Multiport sensor RFIDs for wireless passive sensing of objects - Basic theory and early results”. *IEEE Transactions on Antennas and Propagation*. vol. 56, (no. 8). pp 2691–2702. (August 2008)

[15] J. Siden, X. Zeng, T. Unander, A. Koptyug, and H. E. Nilsson, “Remote moisture sensing utilizing ordinary RFID tags”. *IEEE Sensors Conference*. pp 308–311. October 2007.

[16] Luis Gil “Cork Composites: A Review”. *MDPI Materials*. vol. 2 (Issue 3), page 776–789. (July 2009)

[17] Frederick Declercq, Hendrik Rogier, Senior Member, IEEE, and Carla Hertleer “Permittivity and Loss Tangent Characterization for Garment Antennas Based on a New Matrix-Pencil Two-Line Method”. *IEEE Transactions on Antennas and Propagation*. vol. 56 (no. 8), page 2548–2554. (August 2008)

[18] E8361A PNA Network Analyzer, 10 MHz to 67 GHz. Agilent Technologies. [Online] Available: http://www.home.agilent.com/

[19] S. P. Silva, M. A. Sabino, E. M. Fernandes, V. M. Correlo, L. F. Boessel and R. L. Reis “Cork: properties, capabilities and applications”. *International Materials Reviews, Maney Publishing*. vol. 50 (no. 6), page 345–365. (December 2005)

[20] Henry Berger, James B. Beyer, Roger J. Chaffin, Robert S. Elliott and John W. E. Griemsmann “The Complex Permittivity of Some Cork Composition Materials from 10 to 10 000 MHz”. *IEEE Transactions on Microwave Theory and Techniques*. page 55–57. (January 1968)

[21] V. Despres and C. Akyel “Microwave Sensing of Moisture Content in Wine Corks”. *1997 Asia Pacific Microwave Conference*. vol. 3 page 1089–1092. (2-5 December 1997)

[22] M. C. Lança, E. R. Neagu, C. J. Dias, L. Gil, J. N. Marat-Mendes “Electrical Properties of Cork and Derivatives”. *Ciencia & Tecnologia dos Materiais*. vol. 23 (no. 3/4), page 64–70. (2011)

[23] M. C. Lança, M. Brandt, E. R. Neagu, C. J. Dias, J. N. Marat-Mendes “Dielectric spectra of natrual cork and derivatives”. *Journal of Non-Crystalline Solids*. no. 356, page 763–767. (2010)

[24] Maset del Lleo. Cultura vinicola - Consejos Practicos [Online]. http://www.maset.com/cultura-vinicola/consejos-practicos

[25] ACS Challenge CH250 Environmental Chamber. [Online]. Specifications available at: http://http://www.ets.co.uk/previous_features/0606.php

[26] Isabel Exposito, Inigo Cuinas “RFID Tag Readability around White Wine Bottles”. *2011 19th International Conference on Software, Telecommunications and Computer Networks (SoftCOM)*. page 1–5. (15-17 September 2011)

[27] Ansoft HFSS ver. 13, ANSYS, Inc., Canonsburg, PA, 2009 [Online]. Available: http://www.ansys.com/

[28] Constantine A. Balanis “Antenna Theory: Analysis and Design”. *Third Edition*. Wiley Editions. ISBN: 978-0471667827

[29] LPKF CircuitCAM ver. 6.0, LPKF Laser&Electronics. [Online]. Available: http://www.lpkfusa.com/Software/ccam.htm

[30] LPKF ProtoMat C100/HF Circuit Board Plotter. [Online]. Available: http://www.lpkfusa.com/RapidPCB/CircuitboardPlotters/c100hf.htm

[31] LPKF BoardMaster ver. 5.0, LPKF Laser&Electronics. [Online]. Available: http://www.lpkf.com/products/rapid-pcb-prototyping/software/boardmaster/

[32] Lukas W. Mayer and Arpad L. Scholtz “Sensitivity and Impedance Measurements on UHF RFID Transponder Chips”. *IEEE Transactions on Microwave Theory and Techniques*. vol. 57 (no. 5), page 1297–1302. (May 2009)

[33] Alien Higgs-3, RFID EPC Class 1 Gen 2 RFID Tag IC. [Online]. Specifications available at: http://www.card1688.com/files/alienUHFH3.pdf

[34] EPCglobal Gen 2 Standard. [Online]. Availabe: http://www.gs1.org/gsmp/kc/epcglobal/uhfc1g2

[35] International Organization for Standarization. [Online]. Available at http://www.iso.org

[36] Advanced Design System (ADS) v2008. [Online]. Available: http://www.home.agilent.com/

[37] David M. Pozar “Microwave Engineering”. *Fourth Edition*. Wiley Editions. ISBN: 0470631554

[38] Gaetano Marrocco “The Art of UHF RFID Antenna Design: Impedance-Matching and Size-Reduction Techniques”. *IEEE Antennas and Propagation Magazine*. vol. 50 (no. 1), page 66–79. (February 2008)

[39] Luca Catarinucci, Inigo Cuinas, Isabel Exposito, Riccardo Colella, Jose Antonio Gay Fernandez, Luciano Tarricone “RFID and WSNs for Traceability of Agricultural Goods from Farm to Fork: Electromagnetic and Deployment Aspects on Wine Test-Cases”. *2011 19th International Conference on Software, Telecommunications and Computer Networks (SoftCOM)*. page 1–4. (15-17 September 2011)

[40] Isabel Exposito, Inigo Cuinas, Jose Antonio Gay-Fernandez “Efficient traceability solutions in the wine production by RFID and WSN”. *2013 7th European Conference on Antennas and Propagation (EuCAP)*. page 3539–3542. (8-12 April 2013, Gothenburg)

[41] Yehui Han, Student Member IEEE, Olivia Leitermann, David A. Jackson, Juan M. Rivas, Member, IEEE, and David J. Perreault, Senior Member, IEEE "Reistance Compression Networks for Radio-Frequency Power Conversion". *IEEE Transactions on Power Electronics*. vol. 22 (no. 1), page 41–53. (January 2007)

[42] K. V. Seshagiri Rao, Senior Member, IEEE, Pavel V. Nikitin, Member, IEEE, and Sander F. Lam "Antenna Design for UHF RFID Tags: A Review and a Practical Application". *IEEE Transactions on Antennas and Propagation*. vol. 53 (no. 12), page 3870–3876. (December 2005)

[43] Pavel V. Nikitin, Senior Member, IEEE, K. V. Seshagiri Rao, Senior Member, IEEE, Rene Martinez, Member, IEEE, and Sander F. Lam "Sensitivity and Impedance Measurements of UHF RFID Chips". *IEEE Transactions on Microwave Theory and Techniques*. vol. 57 (no. 5), page 1297–1302. (May 2009)

[44] Pavel V. Nikitin, Senior Member, IEEE and K. V. S. Rao, Senior Member, IEEE "Antennas and Propagation in UHF RFID Systems". *2008 IEEE International Conference on RFID, Las Vegas, NV*. page 277–288. (April 2008)

[45] Pavel V. Nikitin and K. V. S. Rao "Effect of Gen2 Protocol Parameters on RFID Tag Performance". *2009 IEEE International Conference on RFID*. page 117–122. (27-28 April 2009)

[46] Impinj Speedway Revolution UHF RFID Reader. [Online]. Specifications available at: http://www.impinj.com/Speedway_Revolution_Reader_Spec_Table.aspx

[47] Impinj Multireader software v6.6.8. [Online]. Available: http://www.impinj.com/support/downloadable_documents.aspx

APPENDIXS

APPENDIX A. SUBSTRATE CHARACTERIZATION TECHNIQUE

The technique used in this thesis to determine the permittivity and loss tangent of a cork sample is described in this Appendix. The theoretical basis of the used methodology is derived from the work described in the paper *"Permittivity and Loss Tangent Characterization for Garment Antennas Based on a New Matrix-Pencil Two-Line Method"* from Frederick Declerq, Hendrik Rogier and Carla Hertleer [17]; although in the work presented here no matrix pencil employed and the derived dielectric permittivity and loss tangent were computed based on least-squares fitting.

A.1. Determination of the Propagation Factor, Dielectric Constant and Loss Tangent

The S-parameters of two transmission lines of different length are first measured. The S-parameter matrix of the longer lines is indicated as S_d and the S-parameter matrix of the shorter lines as S_t. In a second step, the S-parameter matrices are converted to transmission matrices T_d and T_t respectively using (A.1) and (A.2).

$$T_d = \begin{bmatrix} T_{d11} & T_{d12} \\ T_{d21} & T_{d22} \end{bmatrix} = \begin{bmatrix} -\frac{det(S)}{S_{d21}} & \frac{S_{d11}}{S_{d21}} \\ -\frac{S_{d22}}{S_{d21}} & \frac{1}{S_{d21}} \end{bmatrix} \tag{A.1}$$

$$T_t = \begin{bmatrix} T_{t11} & T_{t12} \\ T_{t21} & T_{t22} \end{bmatrix} = \begin{bmatrix} -\frac{det(S)}{S_{t21}} & \frac{S_{t11}}{S_{t21}} \\ -\frac{S_{t22}}{S_{t21}} & \frac{1}{S_{t21}} \end{bmatrix} \tag{A.2}$$

Being $det(S) = S_{11}S_{22} - S_{21}S_{12}$. Then, T is calculated as: $T = T_d \cdot T_t^{-1}$. The propagation factor is determined by the eigenvalue equation (A.3). $T_r(T)$ represents the trace of T, and the determinant $\Delta(T)$ equals one because of symmetry and reciprocity. Passivity imposes that $\left|e^{-\gamma\Delta l}\right| < 1$. This inequality determines the correct sign of the root in (A.3) and thus the correct angular rotation of γ. Substituting $z = 1/2T_r(T)$ in (A.3) and solving respect to γ yields $\gamma = (\Delta(T)^{-1} ln(z \pm \sqrt{z^2 - 1}))$.

$$e^{\pm\gamma\Delta l} = \frac{T_r(T) \pm \sqrt{(T_r(T))^2 - 4\Delta(T)}}{2} \tag{A.3}$$

The complex propagation factor γ is described as (A.4), alpha being the attenuation constant and beta being the phase constant. The attenuation constant α is decomposed in $\alpha = \alpha_c + \alpha_d$, α_c being α_c the conductor losses and α_d the dielectric losses. Assuming the conductor losses negligible $(\alpha_c = 0)$, the attenuation constant is approximated as the dielectric losses $(\alpha \cong \alpha_d)$. So, from (A.4) the phase constant β is obtained. Once β is known, $\varepsilon_{r,eff}$ is obtained from (A.5) where $k_o = \frac{2\pi}{\lambda_o}$.

$$\gamma = \alpha + j\beta \tag{A.4}$$

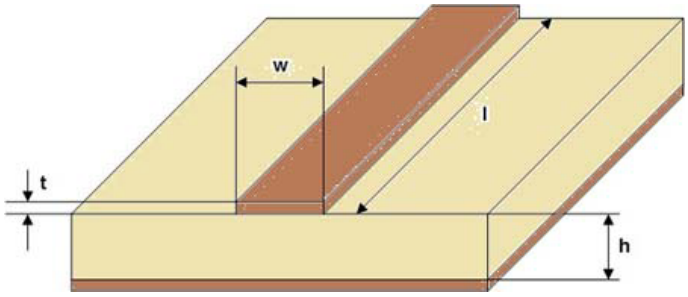

Figure A.1: Schematic of a microstrip line

$$\varepsilon_{r,eff} = \left(\frac{\beta}{k_o}\right)^2 \tag{A.5}$$

A.1.1. Calculation of ε_r from $\varepsilon_{r,eff}$

The microstrip lines used in this thesis are depicted in A.1, the equivalent height and width of the lines are described as $H = h - 2t$ and $W = w + \frac{t}{\pi}\left[ln(\frac{2h}{t}) + 1\right]$. Assuming that all the measured samples comply with the inequality $W/H > 1$, the $\varepsilon_{r,eff}$ is described by (A.6).

$$\varepsilon_{r,eff} = \frac{\varepsilon_r + 1}{2} + \frac{\varepsilon_r - 1}{2}\left[\frac{1}{\sqrt{1 + 12 \cdot (\frac{H}{W})}} + 0.4 \cdot (1 - \frac{W}{H})^2\right] \tag{A.6}$$

So, ε_r is obtained from (A.6). Note that in the case of $W/H \geq 1$, $\varepsilon_{r,eff}$ is described by (A.7).

$$\varepsilon_{r,eff} = \frac{\varepsilon_r + 1}{2} + \frac{\varepsilon_r - 1}{2\sqrt{1 + 12 \cdot (\frac{H}{W})}} \tag{A.7}$$

Finally, after having obtained α_d, $\varepsilon_{r,eff}$ and εr, the loss tangent $tan\delta$ calculation is straightforward from (A.8).

$$tan\delta \approx 0.0366 \frac{\alpha_d \lambda_0 \sqrt{\varepsilon_{r,eff}}(\varepsilon_r - 1)}{\varepsilon_r(\varepsilon_{r,eff} - 1)} \tag{A.8}$$

A.2. Matlab code

Following it is attached the Matlab code used to perform the calculations described in the previous section.

```
%%% Matlab file for the "Substrate Characterization Technique " %%%
%we have a file with Sd that corresponds to the long line
%we have a file with St that corresponds to the short line

%clear all
deltaL=0.005;   %meters
c=3e8;  %meters /s

```

```
fo=Sd(:,1);
lambda0=c./fo;
ko=2* pi ./lambda0;

Sd11=(10.^(Sd(:,2)./20)).*    exp (j.*Sd(:,3).*  pi ./180);
Sd21=(10.^(Sd(:,4)./20)).*    exp (j.*Sd(:,5).*  pi ./180);
Sd12=(10.^(Sd(:,6)./20)).*    exp (j.*Sd(:,7).*  pi ./180);
Sd22=(10.^(Sd(:,8)./20)).*    exp (j.*Sd(:,9).*  pi ./180);

St11=(10.^(St(:,2)./20)).*    exp (j.*St(:,3).*  pi ./180);
St21=(10.^(St(:,4)./20)).*    exp (j.*St(:,5).*  pi ./180);
St12=(10.^(St(:,6)./20)).*    exp (j.*St(:,7).*  pi ./180);
St22=(10.^(St(:,8)./20)).*    exp (j.*St(:,9).*  pi ./180);

detSd=Sd11.*Sd22-Sd12.*Sd21;
detSt=St11.*St22-St12.*St21;

Td11=-detSd./Sd21;
Td12=Sd11./Sd21;
Td21=-Sd22./Sd21;
Td22=1./Sd21;

Td=[Td11 Td12 Td21 Td22];

Tt11=-detSt./St21;
Tt12=St11./St21;
Tt21=-St22./St21;
Tt22=1./St21;

Tt=[Tt11 Tt12 Tt21 Tt22];

for  i=1:1: length (Sd(:,1))
tempTd=[Td(i,1) Td(i,2); Td(i,3) Td(i,4)];
tempTt=[Tt(i,1) Tt(i,2); Tt(i,3) Tt(i,4)];

tempT=tempTd*  inv (tempTt);
trT= trace (tempT);
z=trT/2;
gamma =(1/(deltaL))*  log (z+ sqrt (z^2-1));   %NOTE : select  + or - in the sqrt
    selected  so that  check <1
alfa(i)= real (gamma );
beta (i)= imag (gamma );
er_eff(i)=(  beta (i)./ko(i)).^2;
end

check= abs (exp (-gamma .*deltaL))   %check  has  to  be  <  1

W=1  %mm  (T-line  width )
H=3  %mm  (substrate  heigth )

%%% Calculation  of  dielectric  constant  (er) %%%
```

```
% if W/H > 1, uncomment the following lines :
% er1 =er_eff -0.5+(1./(2* sqrt (1+12.*( H/W))));
% er2 =0.5+(1./(2.* sqrt (1+12.*( H/W))));
% er=er1 ./ er2 ;

% if W/H < 1, uncomment the following lines :
A=1./( sqrt (1+12.*(H/W)))+0.4.*(1-W/H).^2;
er=((er_eff+0.5.*(A-1))./(1+A)).*2;

%%% Calculation of dielectric loss tangent (tanD ) %%%
tanD=0.0366.*(alfa.*lambda0'.*     sqrt (er_eff).*(er-1))./(er.*(er_eff-1));

%%% plot the results %%%
hold on
figure (1)
plot (fo,er)
xlabel ('Frequency [GHz ]');
ylabel ('dielectric constant ');
figure (2)
plot (fo,tanD)
xlabel ('Frequency [GHz ]');
ylabel ('dielectric loss tangent ');
```

APPENDIX B. RFID TAG MEASUREMENTS WITH COMMERCIAL READER

In this appendix there are exposed the measurements performed with a commercial reader on the RFID tag described in Section 3.3. of Chapter 3 of this thesis. Specifically, read range and angular readability measurements were performed using a commercial Impinj Speedway Revolution R420 reader [46]. These measurements were carried out on the laboratory room, thus implying a multipath environment. The RFID tag was placed at a distance D from the reader and this distance was increased until no reading could be performed. A photograph of this measurement setup is shown in Figure B.1. In order to perform the readings, the commercial software povided by Impinj was used [47].

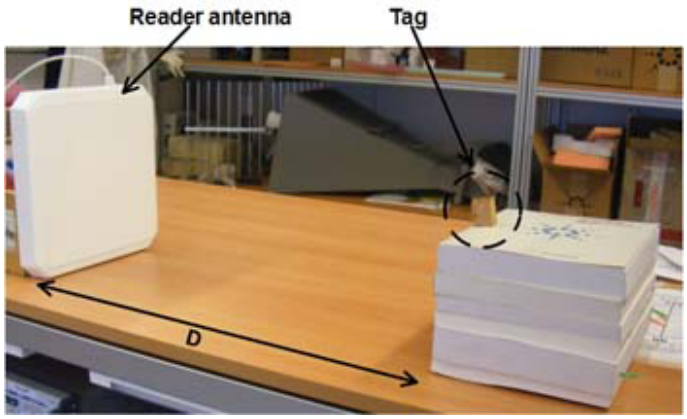

Figure B.1: Photograph of the measurement setup with the commercial reader

The read range measurement results using a commercial Impinj reader are depicted in Figure B.2. The considered RFID tag was moved away from the reader until no reading could be performed. The reader output power was varied from 12dBm to 30dBm in steps of 3dBm. Read range results depicted in Figure B.2 show a good tag performance, as it achieves a maximum read range of about 1m.

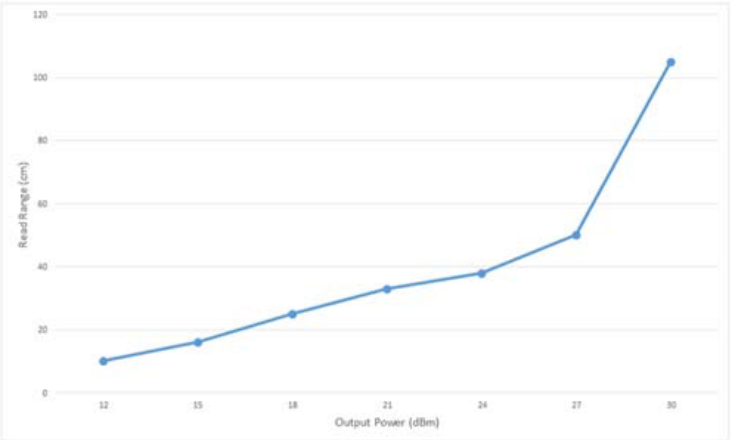

Figure B.2: Measured tag read range vs variable output power

Angular readability of the tag was measured in the anechoic chamber using the commercial reader. The measurement setup is described in Figure B.3. In this case, the mutual orientation between the RFID tag and the antenna was varied from theta 0 ° to 180 ° and the read rate and power received was measured. These results are depicted in Figures B.6 and B.5 respectively.

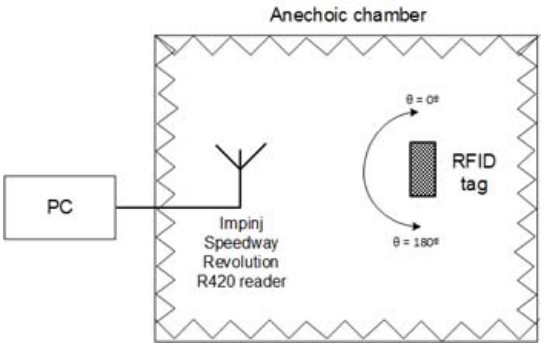

Figure B.3: Scheme of the measurement setup in the anechoic chamber

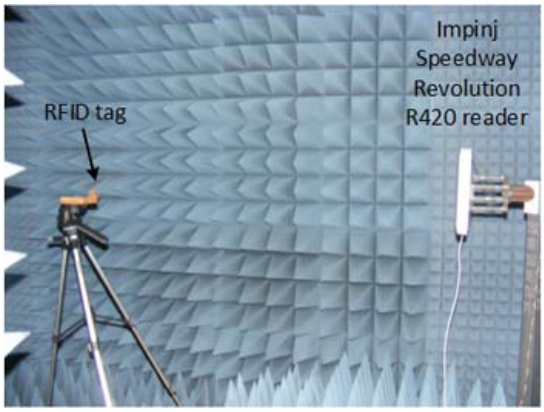

Figure B.4: Anechoic chamber measurement setup

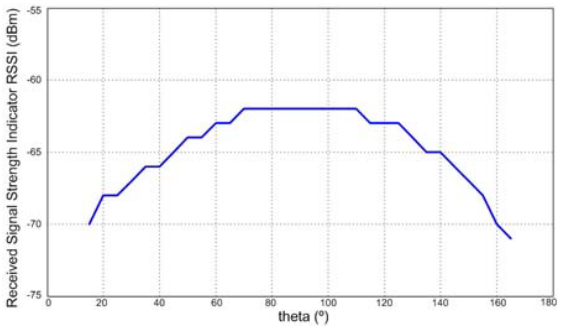

Figure B.5: Angular tag readability

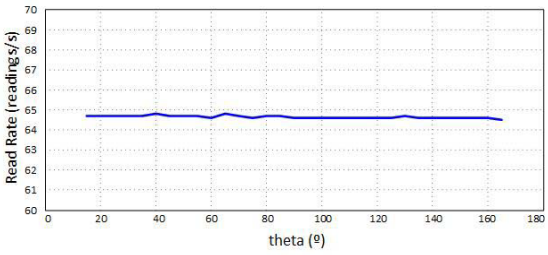

Figure B.6: Tag read rate depending on the tag orientation

As it is apreciated, the angular readability of the considered RFID tag is quite high as it provides readings in an arc of about 160 °. It is seen that only in the extremes, the readings could not be performed properly. On the other hand, results on the read rate shown a good tag performance. Here, the read rate is defined as the total number of counts divided by the time elapsed between the first read and the last. Therefore, a good read rate performance is shown in a wide angular range, providing a readability of around 150 °. In the extremes, it is apreciated that there is no value of read rate; this fact is due to there was not enough backscattered power to perform a reading.

APPENDIX C. MATLAB CODE USED IN THE TAG READ RANGE CALCULATIONS

In this appendix can be found the Matlab code used to perform the read range calculations (simulations) on the RFID tags. This code develops the read range equations described in Chapter 5. Some of the input parameters of the equations (such as the gain of the tag antenna) are imported from Ansys HFSS simulations.

```
%%%%%%%%%%%%%%%%%    READ RANGE CALCULATIONS    %%%%%%%%%%%%%%%%%%%%%%%%%%%%%%%%
freq=820:920;    %frequency , from 820 Mhz to 920 MHz in stes of one MHz
c = 3*10^8;   %constant  c [m/s]
lambda = c/f;   %lambda  [m]
Ptx = 10^-0.6;   %Power transmitted  [lineal ] / 30dBm
Gtx = 10^(5/10);    %Gain of the tranmition  antenna  [lineal ] / 5dBi
EIRP = Ptx*Gtx;    %value in [W] | EIRP = Ptx*Gtx
Grx = Gr(:,2);   %Simulated  gain of the receiver  (tag) antenna  at 868 MHz
Pth = 10^((-18-30)/10);     %Treshold power. Minimum received power to turn on
    the chip [lineal ] / -18dBm

%%%%%%%%%%%%%%%%%%%%%%%%     RFID tag %%%%%%%%%%%%%%%%%%%%%%%%%%%%%%%%%%%%%%%%%%%
Rantenna = Zantenna(:,2);     %real part of the antenna  impedance
Rchip = Zchip(:,2);    %real part of the chip  impedance
Xantenna = Zantenna(:,4)*j;     %imaginary  part of the antenna  impedance
Xchip = Zchip(:,4)*j;    %imaginary  part of the antenna  impedance
Zantenna = Rantenna + Xantenna;      %antenna  impedance
Zchip = Rchip + Xchip;    %chip  impedance
tau = (4.*Rchip.*Rantenna)./(    abs(Zchip+Zantenna).^2);
range_original = (lambda/(4*    pi))*(sqrt((EIRP*Grx.*tau)/Pth));
%%%%%%%%%%%%%%%%%%%%%%%%     end RFID tag %%%%%%%%%%%%%%%%%%%%%%%%%%%%%%%%%%%%%%%

%%%%%%%%%%%%%%%%%%%%%%%%     tag with R=100 Ohm %%%%%%%%%%%%%%%%%%%%%%%%%%%%%%%%
GR1 = GR1(:,2);   %simulated  gain of the tag with R = 100 Ohm
RR1 = ZR1(:,2);   %real part of the antenna  impedance
XR1 = ZR1(:,3)*j;    %imaginary  part of the antenna  impedance
ZR1 = RR1 + XR1;   %antenna  impedance
tauR1 = (4.*Rchip.*RR1)./(    abs(Zchip+ZR1).^2);
R1 = (lambda/(4*  pi))*(sqrt((EIRP*GR1.*tauR1)/Pth));
%%%%%%%%%%%%%%%%%%%%%%%%     end tag R100 %%%%%%%%%%%%%%%%%%%%%%%%%%%%%%%%%%%%%%%

%%%%%%%%%%%%%%%%%%%%%%%%     tag with R=150 Ohm %%%%%%%%%%%%%%%%%%%%%%%%%%%%%%%%
GR2 = GR2(:,2);   %simulated  gain of the tag with R = 150 Ohm
RR2 = ZR2(:,2);   %real part of the antenna  impedance
XR2 = ZR2(:,3)*j;    %imaginary  part of the antenna  impedance
ZR2 = RR2 + XR2;   %antenna  impedance
tauR2 = (4.*Rchip.*RR2)./(    abs(Zchip+ZR2).^2);
R2 = (lambda/(4*  pi))*(sqrt((EIRP*GR2.*tauR2)/Pth));
%%%%%%%%%%%%%%%%%%%%%%%%     end tag R150 %%%%%%%%%%%%%%%%%%%%%%%%%%%%%%%%%%%%%%%

plot(freq,range_original,    'k-',freq,R1, 'kd',freq,R2, 'ks')
```

APPENDIX D. MATLAB CODE USED TO GENERATE THE TAG WAKEUP SQUENCE

In this appendix there is the Matlab code used in Chapter 5 in order to realize the tag measurements. The code generates a tag wakeup sequence, which is sent to a signal generator. This Matlab code has been provided by Gianfranco Andía Vera, Phd. Student at Laboratoire de Conception et d'Integration des Systèmes (LCIS), Grenoble (France).

```
%function  send_query  (freq,p)
freq=980;  % MHZ
p=24;  % dBm

%% Charge  le  query  dans  le  generateur
%Avec  ce  programme  on  crée  un  vecteur  binaire  (seulement  2  valeurs  :  0
%ou  1)  ayant  les  caract éristiques  choisies  précédemment .  La  fréquence
%déchantillonnage  vaut  20MHz,  ce  qui  est  compatible  avec  les  capacit és
%du  générateur  qui  a  une  fréquence  déchantillonnage  maximale  de  30MHz.

%% 1)  connection  VISA  Instrument
% TCPIP  parameters  of  the  Spectrum  Analyzer
 mxa_ip =  '10.1.3.152 ';
 mxa_port = 5025;
 % MXA  Interface  creation  and  connection  opening
 fprintf ('\nConnecting  to  Instrument  ...\n');
 deviceObject = tcpip(mxa_ip,mxa_port);
 deviceObject.OutputBufferSize = 1000000;
 deviceObject.ByteOrder =  'littleEndian ';
 fopen (deviceObject);
 % Intrument  identification
 idn = query(deviceObject,  '*IDN?');
 fprintf ('Hello  from  %s', idn);

%% 2)  Génération  de  la  commande  QUERY
% temps  entre  chaque  échantillon
%delta_t  = 50*10^-9;
delta_t = 25*10^-9;

%fréquence  d'échantillonnage
f_ech=1/delta_t;

%Définition  de  l'entête
%Durée  du  delimiter ,  du  tari ,  du  PW,  du  data1 ,  du  RTcal  et  du  TRcal
d_delimiter=12.5*10^-6;
d_tari=12.5*10^-6;
d_PW=d_tari*0.5;
d_data1=1.75*d_tari;
d_RTcal=d_data1+d_tari;
d_TRcal=2*d_RTcal;
d_CW11=10*d_RTcal;
```

```
d_CW1=20*d_RTcal;
d_CW0 = 30*d_RTcal;

%Nombre de points
long_delimiter =  round (d_delimiter/delta_t);
long_tari =  round (d_tari/delta_t);
long_PW =  round (d_PW/delta_t);
long_data1 =  round (d_data1/delta_t);
long_RTcal =  round (d_RTcal/delta_t);
long_TRcal =  round (d_TRcal/delta_t);
long_CW11 =  round (d_CW11/delta_t);
long_CW1 =  round (d_CW1/delta_t);
long_CW0 =  round (d_CW0/delta_t);

%Définition des vecteurs
delimiter= zeros (1 , long_delimiter+1);
data0=[ones(1,long_tari-long_PW+1),      zeros (1,long_PW+1)];
data1=[ones(1,long_data1-long_PW+1),      zeros (1,long_PW+1)];
RTcal=[ones(1,long_RTcal-long_PW+1),      zeros (1,long_PW+1)];
TRcal=[ones(1,long_TRcal-long_PW+1),      zeros (1,long_PW+1)];
CW11=ones(1,long_CW11+1);
CW1=ones(1,long_CW1+1);
CW0= zeros (1,long_CW0+1);

%Définition de l'entete
entete = [delimiter,data0,RTcal,TRcal];

%Vecteur commande QUERY
vecteur= [1 0 0 0 1 0 1 1 0 0 0 0 0 0 0 0 0 0 1 1 0 1];

% %Vecteur commande QUERY
% vecteur =[1 1 1 1 1 1 1 1 1 1 1 1 1 1 1 1 1 1 1 1 1 1];

%Définition de la trame commande QUERY
commande=[];
n=0;
for i = 1: length (vecteur)
    n=n+1;
    if vecteur(n)==1
        commande=[commande,data1];
    elseif vecteur(n)==0
        commande=[commande,data0];
    end
end
trame=[CW11,entete,commande,CW1];

%Création d'un fichier de données comprenant les
%vecteurs I et Q ainsi que le marker
idata = trame;
qdata =  zeros (1, length (idata));
marker =  zeros (1, length (idata));
```

```
marker(1:16250)= 1;

% 3) Charge le query dans la memoire du generateur et envoi le signal
% Some more commands to make sure we don't damage the instrument
fprintf (deviceObject, ':SOURce :RADio :ARB :STATe OFF')
fprintf (deviceObject, ':OUTPut :MODulation :STATe OFF')
% Set the instrument source freq
freq=freq*1e6;
fprintf (deviceObject, [ 'SOURce :FREQuency ' num2str (freq)]);
% Set the source power
fprintf (deviceObject, [ 'POWer ' num2str (p)]);

% Write the data to the instrument
n = size (trame);
%sprintf ('Starting Download of %d Points \n',n(2) /2)
binblockwrite(deviceObject,trame, 'single ',':MEM :DATA "WFM1 : query ",');
%binblockwrite (deviceObject ,trame ,'double ',': MEM :DATA "WFM1 : query ",') ;

fprintf (deviceObject, '');

fprintf (deviceObject, ':SOURce :RADio :ARB :WAV "WFM1 : query "');
% Some more commands to start playing back the signal on the instrument
fprintf (deviceObject, ':SOURce :RADio :ARB :STATe ON') %Arb on
fprintf (deviceObject, ':OUTPut :MODulation :STATe ON') %Mod on
%fprintf (deviceObject ,': OUTPut :MODulation :STATe OFF') %Mod on

fprintf (deviceObject, ':OUTPut :STATe ON') %RF on
%fprintf (deviceObject ,': SOURce :RADio :ARB :WAV "ARBI : query_20M_AC "') ;
% Position du marker
  %réinitialier tous les markers
fprintf (deviceObject, 'SOURce :RADio :ARB :MARK :CLEar :ALL "WFM1 : query ",1');
%marker_pos =16200; % signle - %delta_t = 50*10^-9;
marker_pos=33000 % 3000; % signle - %delta_t = 25*10^-9;

fprintf (deviceObject,[ ':SOURce :RADio :ARB :MARKer :SET "WFM1 : query ",1, '
    num2str (marker_pos) ',' num2str (marker_pos) ',0']);
% Close the connection to the instrument
fclose (deviceObject);

save trame.mat trame
```

APPENDIX E. SPECIFICATIONS OF THE LUMPED COMPONENTS

In this appendix there are described the specifications of the lumped components used in the expansion network used in the RFID tags with sensing capabilities described in Chapter 4. This expansion network involve resistances, capacitors and inductors. Inductors are from Coilcraft while capacitors and resistances are from Murata. All of them are SMD type. In addition, some of them are 0402 class and others 0603 class, which involve different dimensions that are going to be discussed in the following sections.

E.1. Resistances

As it is explained in Chapter 4, in this thesis have been used two different resistance values. Specifically, resistances of 100Ω and 150Ω respectively. Both of them are 0402 class, dimensions of both components are the same and are specified in Table E.1 and Figure E.1.

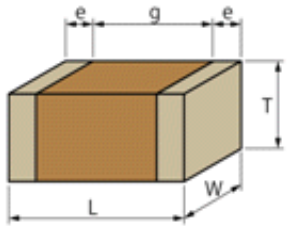

Figure E.1: Scheme of the device dimensions

L size	0.6±0.03mm
W size	0.3±0.03mm
T size	0.3±0.03mm
External terminal width e	0.1 to 0.2mm
Distance between external terminals g	0.2mm min.
Size code in mm	0603

Table E.1: Dimensions of the resistance components

E.2. Capacitors

There were used three different capacitors with values 1.2 pF, 10 pF and 22 pF respectively. As the case of resistances, the capacitors used are 0603 type, which involve a component dimensions describe in Table E.2. Dimensions specified in the table correspond refer to those specified in Figure E.1.

L size	0.6±0.03mm
W size	0.3±0.03mm
T size	0.3±0.03mm
External terminal width e	0.1 to 0.2mm
Distance between external terminals g	0.2mm min.
Size code in mm	0603

Table E.2: Dimensions of the capcitors

E.3. Inductors

There were used two different inductors with values 1 nH and 8.3 nH respectively. In this case, the inductors used are 0402 type, which involve the dimensions specified in Table E.3 and Figure E.2.

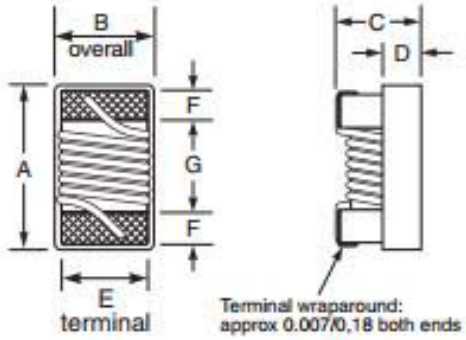

Figure E.2: Scheme of the inductor dimensions

A	1.14mm
B	0.51 - 0.71mm
C	0.61mm
D	0.25mm
E	0.51mm
F	0.2mm
G	0.61mm

Table E.3: Dimensions of the inductors

APPENDIX F. RTD SENSOR SPECIFICATIONS

Following, it is attached the datasheet with the temperature sensor specifications.

PTS Series - Pt-Sensors

Vishay Beyschlag

VISHAY.

Platinum SMD Flat Chip Temperature Sensor

PTS SMD Flat Chip Temperature sensors are the perfect choice for temperature control of electronics operating under varying environmental conditions. The highly controlled platinum thin film manufacturing process guarantees an outstanding stability of temperature characteristics which ensures reliable operation even under harsh conditions. Typical applications include automotive, aviation and industrial electronics.

FEATURES

- Standardized characteristics according to IEC 60751
- Advanced thin film technology
- Short reaction times down to $t_{0.9} \leq 2$ s (in air)
- Outstanding stability of temperature characteristic
- Standard SMD sizes
- Supports lead (Pb)-free soldering
- Compliant to RoHS Directive 2002/95/EC

Pb e3 RoHS COMPLIANT

APPLICATIONS

Temperature measurement in

- Automotive electronics
- Aviation electronics
- Industrial electronics

TECHNICAL SPECIFICATIONS

DESCRIPTION		PTS 0603	PTS 0805	PTS 1206
Resistance values R_0 at 0 °C		100 Ω	100 Ω, 500 Ω	100 Ω, 500 Ω, 1000 Ω
Temperature coefficient (0 °C ... + 100 °C)		+ 3850 ppm/K		
Tolerance classes		F0.3, F0.6		
Operating temperature range		- 55 °C to + 155 °C		
Long term stability $\Delta R_0/R_0$: R_0 change after 1000 h at + 155 °C		< ± 0.04 %		
Insulation resistance		> 10 MΩ		
Measurement current I_{meas} (DC) [2]	100 Ω	0.1 mA to 0.50 mA	0.1 mA to 1.0 mA	0.1 mA to 1.0 mA
	500 Ω	-	0.1 mA to 0.40 mA	0.1 mA to 0.40 mA
	1000 Ω	-	-	0.1 mA to 0.25 mA
Self-heating [1]	Still air (v = 0 m/s)	≤ 0.9 K/mW	≤ 0.8 K/mW	≤ 0.7 K/mW
Thermal response time [1]	Flowing water (v = 0.4 m/s)	$t_{0.5} \leq 0.1$ s	$t_{0.5} \leq 0.2$ s	$t_{0.5} \leq 0.3$ s
		$t_{0.9} \leq 0.2$ s	$t_{0.9} \leq 0.3$ s	$t_{0.9} \leq 0.4$ s
	Flowing air (v = 3.0 m/s)	$t_{0.5} \leq 1.0$ s	$t_{0.5} \leq 1.5$ s	$t_{0.5} \leq 2.0$ s
		$t_{0.9} \leq 2.0$ s	$t_{0.9} \leq 3.0$ s	$t_{0.9} \leq 5.0$ s

Notes
[1] Valid for sensor element only
[2] Indicated measurement currents can be applied continuously with self-heating effect of less than 0.1 °C

Figure F.1: Temperature sensor datasheet - page 1/4

DIMENSIONS in millimeters

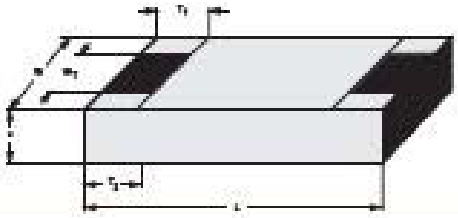

DIMENSIONS - PTS sensor types, mass and relevant physical dimensions							
TYPE	H	L	W	W_T	T_1	T_2	MASS (mg)
PTS 0603	0.45 + 0.1/- 0.05	1.55 ± 0.05	0.85 ± 0.1	> 75 % of W	0.3 + 0.15/- 0.2	0.3 + 0.15/- 0.2	1.9
PTS 0805	0.45 + 0.1/- 0.05	2.0 ± 0.1	1.25 ± 0.15	> 75 % of W	0.4 + 0.1/- 0.2	0.4 + 0.1/- 0.2	4.6
PTS 1206	0.55 ± 0.1	3.2 + 0.1/- 0.2	1.6 ± 0.15	> 75 % of W	0.5 ± 0.25	0.5 ± 0.25	9.2

PRODUCTION

Production is strictly controlled and follows an extensive set of instructions established for reproducibility. A homogeneous film of platinum is deposited on a high grade ceramic body (96 % Al_2O_3). The sensor-elements are covered by a protective coating designed for electrical, mechanical and climatic protection. The terminations receive a final pure tin on nickel plating.

QUALITY

The result of the determined production is verified by an extensive testing procedure performed on 100 % of the individual sensors. Only accepted products are laid directly into the paper tape in accordance with IEC 60286-3.

STORAGE

Solderability is specified for 2 years after production or re-qualification. The permitted storage time is 2 years.

ASSEMBLY

The Pt-sensors are suitable for processing on automatic SMD assembly systems. They are suitable for automatic soldering using wave, reflow or vapour phase. The encapsulation is resistant to all cleaning solvents commonly used in the electronics industry, including alcohols, esters and aqueous solutions. The Pt-sensors are RoHS compliant, the pure tin plating provides compatibility with lead (Pb)-free and lead-containing soldering processes. The immunity of the plating against tin whisker growth has been proven under extensive testing.

All products comply with the CEFIC-EECA-EICTA list of legal restrictions on hazardous substances.

This includes full compatibility with the following directives:

- 2000/53/EC End of Vehicle life Directive (ELV)
- 2000/53/EC Annex II to End of Vehicle Life Directive (ELV II)
- 2002/95/EC Restriction of the use of Hazardous Substances Directive (RoHS)
- 2002/96/EC Waste Electrical and Electronic Equipment Directive (WEEE)

APPROVALS

The Pt-sensors are tested in accordance with IEC 60751 and IEC 60068 series.

Figure F.2: Temperature sensor datasheet - page 2/4

PART NUMBER AND PRODUCT DESCRIPTION (1)

PART NUMBER (2): PTS0603B01B100RP100

P	T	S	0	6	0	3	B	0	1	B	1	0	0	R	P	1	0	0

TYPE	SIZE CODE	SPECIAL CHARACTER	TOLERANCE CLASS	RESISTANCE VALUE	PACKAGING (3)	SPECIAL
3 digits	4 digits	1 digit	2 digits	4 digits	2 digits	2 digits
PTS = Platinum Temperature Sensor SMD	0603 0805 1206	0 = Neutral	1B = Class F0.3 2B = Class F0.6	100R = 100 Ω 500R = 500 Ω 1K00 = 1000 Ω	PU P1	00 = Standard

PRODUCT DESCRIPTION (4): PTS 0603-B P1 100R

PTS	0603	-B	P1	100R
TYPE	SIZE CODE	TOLERANCE CLASS	PACKAGING (3)	RESISTANCE VALUE
PTS = Platinum Temperature Sensor SMD	0603 0805 1206	B = Class F0.3 2B = Class F0.6	PU P1	100R = 100 Ω 500R = 500 Ω 1K = 1000 Ω

Notes
(1) Products can be ordered using either the PART NUMBER or the PRODUCT DESCRIPTION
(2) The part number is shown to facilitate the introduction of a unified part numbering system
(3) Please refer to table PACKAGING
(4) We recommend that the Production Description is used to minimize the possibility of errors in order handling

PACKAGING

MODEL	DIAMETER	PIECES	CODE	BOX/REEL
PTS 0603	114 mm	100	PU	BOX
	180 mm/7"	1000	P1	REEL
PTS 0805	114 mm	100	PU	BOX
	180 mm/7"	1000	P1	REEL
PTS 1206	114 mm	100	PU	BOX
	180 mm/7"	1000	P1	REEL

Figure F.3: Temperature sensor datasheet - page 3/4

FUNCTIONAL PERFORMANCE

The temperature resistance relationships of the PTS series follow different equations:

For the temperature range of - 55 °C up to 0 °C:

$$R_T = R_0 \times (1 + A \times T + B \times T^2 + C \times (T - 100\ °C) \times T^3)$$

And for the temperature range of 0 °C up to + 155 °C:

$$R_T = R_0 \times (1 + A \times T + B \times T^2)$$

R_T: Resistance as a function of temperature
R_0: Nominal resistance value at 0 °C
T: Temperature in °C

Coefficients according to IEC 60751:

$A = 3.9083 \times 10^{-3}\ °C^{-1}$
$B = -5.775 \times 10^{-7}\ °C^{-2}$
$C = -4.183 \times 10^{-12}\ °C^{-4}$

The tolerances values of the PTS series are classified by the following equations as specified by IEC 60751:

Class F0.3: $\Delta T_{F0.3} = \pm (0.30 + 0.005 \times |T|)$

Class F0.6: $\Delta T_{F0.6} = \pm (0.60 + 0.010 \times |T|)$

NOMINAL RESISTANCE VALUE

TEMPERATURE	R/R_0 RATIO	NOMINAL RESISTANCE VALUES			CLASS F0.3	CLASS F0.6
		R_0 100 Ω	R_0 500 Ω	R_0 1000 Ω	T_{TOL}	T_{TOL}
(°C)		(Ω)	(Ω)	(Ω)	(°C)	(°C)
- 55	0.78319	78.32	391.59	783.19	± 0.58	± 1.15
- 50	0.80306	80.31	401.53	803.06	± 0.55	± 1.10
- 45	0.82290	82.29	411.45	822.90	± 0.53	± 1.05
- 40	0.84271	84.27	421.35	842.71	± 0.50	± 1.00
- 35	0.86248	86.25	431.24	862.48	± 0.48	± 0.95
- 30	0.88222	88.22	441.11	882.22	± 0.45	± 0.90
- 25	0.90192	90.19	450.96	901.92	± 0.43	± 0.85
- 20	0.92160	92.16	460.80	921.60	± 0.40	± 0.80
- 15	0.94124	94.12	470.62	941.24	± 0.38	± 0.75
- 10	0.96086	96.09	480.43	960.86	± 0.35	± 0.70
- 5	0.98044	98.04	490.22	980.44	± 0.33	± 0.65
0	1.00000	100.00	500.00	1000.00	± 0.30	± 0.60
5	1.01953	101.95	509.76	1019.53	± 0.33	± 0.65
10	1.03903	103.90	519.51	1039.03	± 0.35	± 0.70
15	1.05849	105.85	529.25	1058.49	± 0.38	± 0.75
20	1.07794	107.79	538.97	1077.94	± 0.40	± 0.80
25	1.09735	109.73	548.67	1097.35	± 0.43	± 0.85
30	1.11673	111.67	558.36	1116.73	± 0.45	± 0.90
35	1.13608	113.61	568.04	1136.08	± 0.48	± 0.95
40	1.15541	115.54	577.70	1155.41	± 0.50	± 1.00
45	1.17470	117.47	587.35	1174.70	± 0.53	± 1.05
50	1.19397	119.40	596.99	1193.97	± 0.55	± 1.10
55	1.21321	121.32	606.60	1213.21	± 0.58	± 1.15
60	1.23242	123.24	616.21	1232.42	± 0.60	± 1.20
65	1.25160	125.16	625.80	1251.60	± 0.63	± 1.25
70	1.27075	127.08	635.38	1270.75	± 0.65	± 1.30
75	1.28987	128.99	644.94	1289.87	± 0.68	± 1.35
80	1.30897	130.90	654.48	1308.97	± 0.70	± 1.40
85	1.32803	132.80	664.02	1328.03	± 0.73	± 1.45
90	1.34707	134.71	673.53	1347.07	± 0.75	± 1.50
95	1.36608	136.61	683.04	1366.08	± 0.78	± 1.55
100	1.38506	138.51	692.53	1385.06	± 0.80	± 1.60
105	1.40400	140.40	702.00	1404.00	± 0.83	± 1.65
110	1.42293	142.29	711.46	1422.93	± 0.85	± 1.70
115	1.44182	144.18	720.91	1441.82	± 0.88	± 1.75
120	1.46068	146.07	730.34	1460.68	± 0.90	± 1.80
125	1.47951	147.95	739.76	1479.51	± 0.93	± 1.85
130	1.49832	149.83	749.16	1498.32	± 0.95	± 1.90
135	1.51710	151.71	758.55	1517.10	± 0.98	± 1.95
140	1.53584	153.58	767.92	1535.84	± 1.00	± 2.00
145	1.55456	155.46	777.28	1554.56	± 1.03	± 2.05
150	1.57325	157.33	786.63	1573.25	± 1.05	± 2.10
155	1.59191	159.19	795.96	1591.91	± 1.08	± 2.15

Figure F.4: Temperature sensor datasheet - page 4/4

APPENDIX G. PATCH ANTENNA

In order to realize the tag measurements explained in Chapter 5 it was fabricated a patch antenna to be used as a reader antenna. In this appendix there are specified the main antenna parameters as it is also explained the antenna fabrication process.

The antennna was designed to work in the whole RFID UHF band (860 - 920 MHz). Moreover, it was required to have circularly polarization, as it had to work as the reader antenna for the measurements. In fact, as the RFID tag is linearly polarized, the reader antenna must be circularly polarized in order to ensure that the tag can be read in any orientation. In order to provide the antenna with circularly polarization, it was added a 90° hybrid. Thus, the antenna is fed by two modes with a 90° phase delay with respect to the other mode. Antenna design process was carried out using Agilent ADS Momentum; in Figure G.1 there is the Momentum antenna layout.

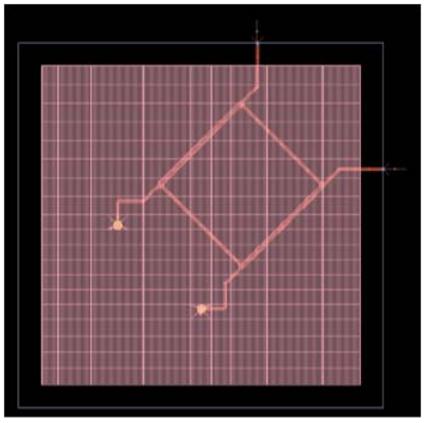

Figure G.1: ADS layout of the antenna design

The design was simulated and some of the antenna parameters given in simulation result are described in Table G.1. Furthermore, in Figure G.2 there are depicted the simulated S-parameters, in Figure G.3 the simulated axial ratio and Figure G.4 shows the simulated gain and directivity.

Parameter	Value	Unit
Gain	9.076	dB
Directivity	9.089	dB
Axial ratio	1.46	dB
Effective angle	88.79	degrees

Table G.1: Simulated patch antenna parameters

Following, the next step was the antenna fabrication. The layout was exported into gerber format to be used in the control software of the milling machine. Then, the substrate was milled as well as the hybrid and the ground plane. The patch and the ground were cut with a guillotine, providing them with the required dimensions. Following, the pieces were assembled; a piece of foam (with an ε_r close to the air) was placed between the patch and the ground plane. Finally, the two feeds were soldered between the patch and the ground plane. A photograph of the fabricated antenna is shown in Figure G.5.

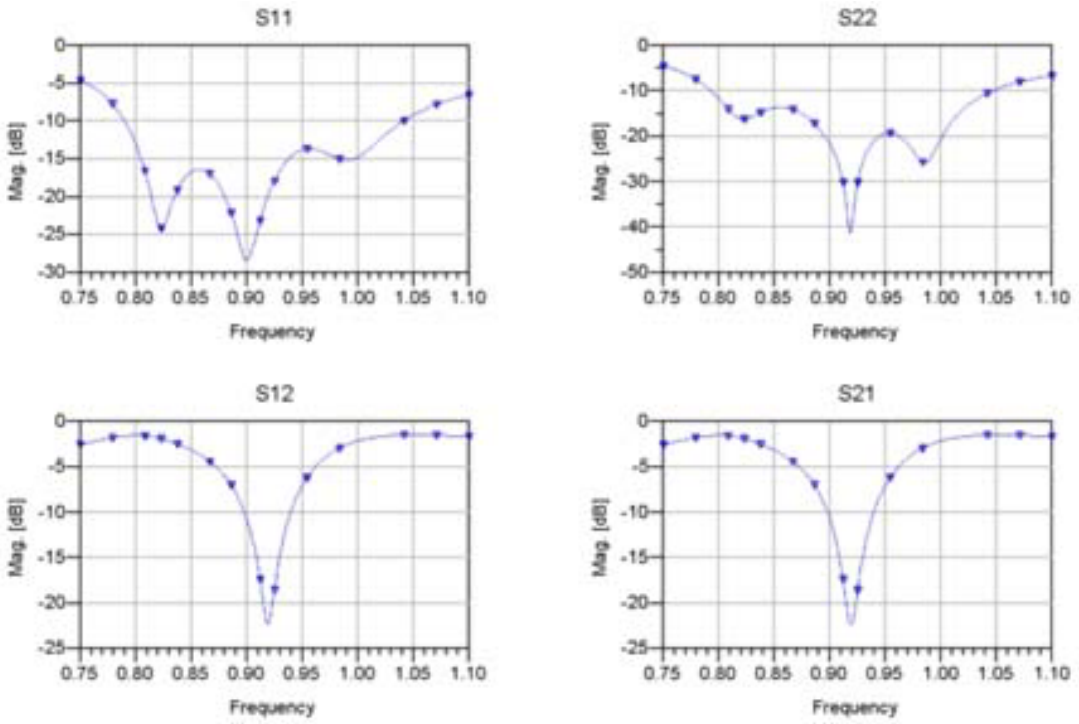

Figure G.2: Simulated S-parameters

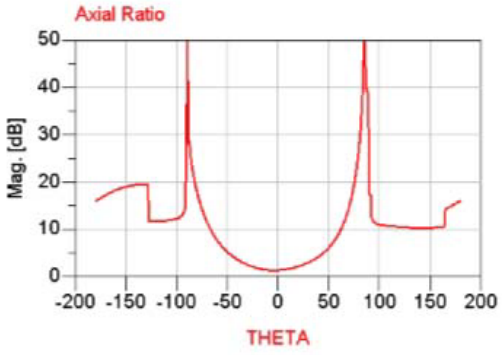

Figure G.3: Simulated axial ratio

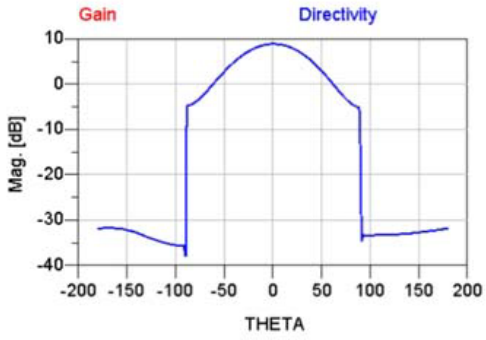

Figure G.4: Simulated gain and directivity

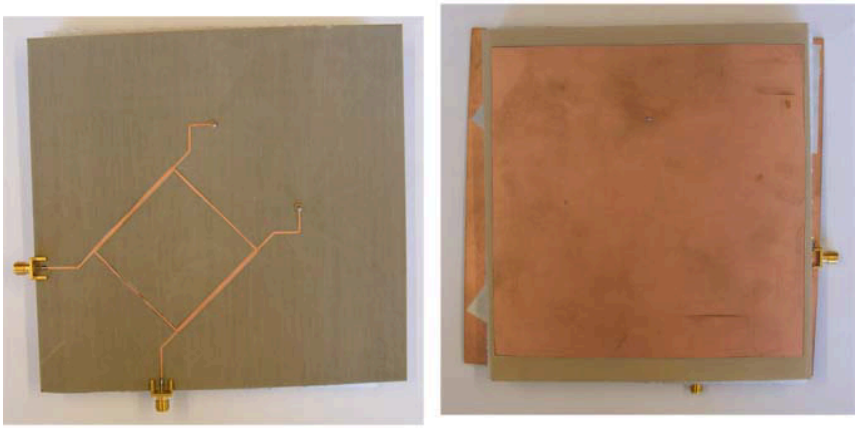

(a) (b)

Figure G.5: Photo of the fabricated patch antenna. (a) Rear view - (b) Front view